Singlet Fission Photovoltaics

by

Jiye Lee

Submitted to the Department

of Electrical Engineering and Computer Science

in partial fulfillment of the requirements for the degree of

Doctor of Philosophy

at the

Massachusetts Institute of Technology

February 2013

Author.....
Department of Electrical Engineering and Computer Science
January 28, 2013

Certified by .....
Professor Marc A. Baldo
Thesis Supervisor

Certified by .....
Professor Leslie A. Kolodziejski
Chair, Department Committee on Graduate Students

Singlet Fission Photovoltaics

by

Jiye Lee

Submitted to the Department of Electrical Engineering and Computer Science on January 28, 2013, in partial fulfillment of the requirements for the degree of Doctor of Philosophy

Abstract

The efficiency of a solar cell is restricted by the "single junction limit," whereby photons with energy higher than the bandgap lose energy by thermalization. Singlet exciton fission splits a high-energy molecular excitation ("singlet" exciton) into a pair of low-energy ones ("triplet" excitons). In solar cells, it promises to generate two electrons per photon, potentially overcoming the singlet junction efficiency limit.

In this thesis, we present singlet-fission-based photovoltaic cells that generate more than one electron per photon. We first demonstrate organic photodetectors with quantum efficiencies reaching 100% by exploiting singlet exciton fission. Through study of the magnetic field dependence of the fission process, we find an optimum thickness of singlet fission layers that guarantees the nearly 100% conversion of a singlet into two triplets. By employing an exciton blocking layer and a light trapping scheme to the solar cell, we demonstrate the peak external quantum efficiency exceeding 100% in the visible spectrum. It is the first time that any solar cell has generated more than one electron per photon outside the UV spectrum.

We also build a simple model that predicts the rate of singlet fission through intermolecular coupling, enabling rational designs of singlet fission molecules and devices. Finally, we propose a future direction—generating *three* electrons per photon. As a step toward this goal, we demonstrate singlet exciton fission in hexacene, whose energetics may allow a singlet to split into three triplets.

Thesis Supervisor: Marc A. Baldo

Acknowledgments

Like any other PhD students, I had a lot of ups and downs for the last six years. Here I would like to thank many people who held my hands during this rollercoaster. First of all, I am so grateful to my awesome advisor Marc Baldo. No matter where I was, Marc always had faith in my capability as a researcher. During my first three years, my research wasn't going so well and I seriously doubted my ability to pursue a PhD degree. But Marc somehow believed that I would do great research—this thesis and my enthusiasm toward research are the product of his abiding trust. I also learned the joy of doing research from Marc. Probably the best times in my PhD were not when my papers were accepted to top-tier journals but when I found some new things in dark optics labs or during our endless discussions.

I was very fortunate to work with Troy Van Voorhis, my physical chemistry advisor. My training was supposed to be on devices, but Troy helped me widen my interest to molecular levels. When I had vague ideas and data which I didn't know what to do about, Troy knew how to 'cook' my data, turning it to invaluable pieces. I thank Vladimir Bulovic for making great comments about my dissertation. His questions and comments allowed me to see a big picture.

I had amazing collaborators outside MIT. I had a good fortune of running into Koen Vandewal at MRS and writing a paper with him and his advisor Jean Manca. I thank Matt Sfeir and Chuck Black in Brookhaven National Lab for hosting me in their lab and training me as a quasi spectroscopist. John Anthony and Matt Bruzek at University of Kentucky were kind enough to respond to my sudden email asking for

collaboration and provide their special molecules. I also thank Mark Wilson and Professor Richard Friend for their collaboration, which made my last project at MIT possible.

My works at MIT would have been impossible without my fellow group members. Michael Segal helped me get on track for research. Carlijn and Priya, I miss our mixture of girly talks and research discussions. Kaveh showed me how to navigate the world of nanofabrication. I was supposed to mentor Hiroshi and Lisa, my UROPs, but it was probably me who learned more by working together. Phil was always patient to listen to all my concerns, which enormously supported me throughout my PhD. I would always go to Matthias if I needed advices on mechanical stuffs. Nick and Dan, we wrote a hero paper; I will never forget our three shifts of making pentacene devices. Shane, my computational chemistry teammate, made lots of cool molecular pictures and calculations. Luke, Benjie, Kemal, Paul, Jean Anne, Tony, David, Sebastian, Mihai, Shlomy, Jon, Mike Currie, Tim, Jason, Amador, Carmel, Eric, thank you for helping me on various topics and being good friends.

I've spent more than half of my twenties at MIT and it was full of joy thanks to my buddies: Tim, Jin, Will, and Charles. We're now spread out all over the world, but let's keep our friendship forever. Mom and Dad, I love you and thank you for being proud of your daughter. And lastly but most importantly, I've been with Wonyoung, my husband as well as my soul mate, during this long journey. We share our passion for work and the world. If I stand on the shoulders of giants, it's Wonyoung who raises me up every day.

Table of Contents

1. Introduction

Solar energy, radiant light from the sun, can supply an almost infinite amount of clean energy for human energy uses. The total solar energy absorbed by the Earth is around 3,850,000 exajoules (EJ) per year.[2] The solar energy that hits the Earth every hour can provide the energy human civilization uses every year.[3] Figure 1-1 shows the land area

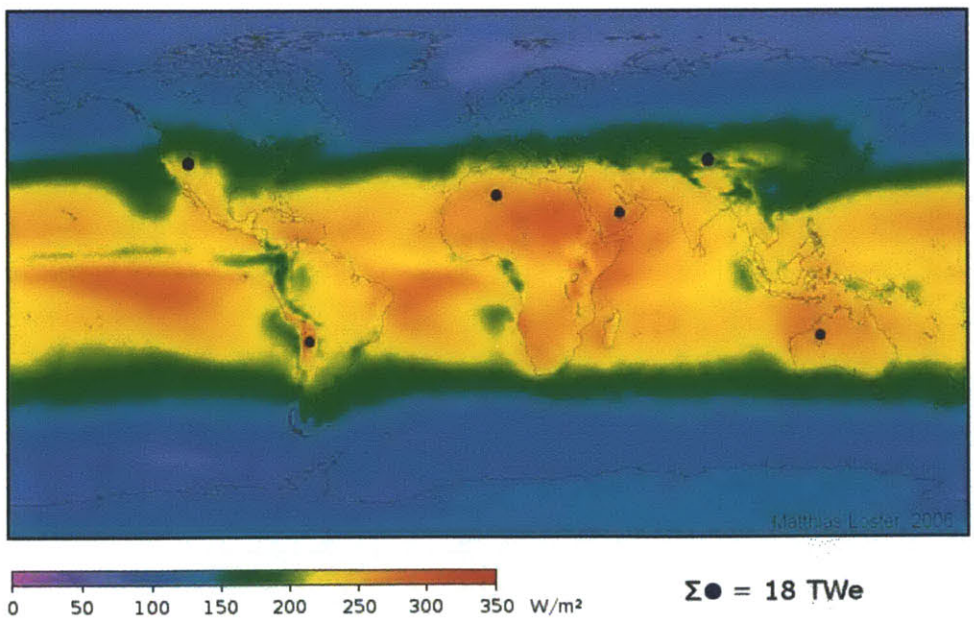

Figure 1-1 Local solar flux in the world. Solar energy produced by solar panels that cover the black area could provide the world's total energy demand. Taken from Ref. 1.

required to provide the world's total energy consumption with solar electricity.[1]

The development of solar energy technologies will bring huge long-term benefits. It will decrease countries' reliance on fossil fuels, enhance sustainability on the global scale, and fight environmental pollutions and climate changes.[4]

To execute this mission, photovoltaic technologies need to be cheap enough to compete with coal or gas-fired generation. Silicon solar cells, the current premier solar technology, have 15–20% efficiencies. In March 2012, mono-crystalline silicon cells are priced at $1.06 per watt and the price has steadily decreased due to efficient production from China.[5] Organic solar cells can be manufactured with roll-to-roll processing instead of expensive clean-room processes. If organic solar cells have efficiencies comparable to other solar cell technologies (~15%), they could provide cheap, efficient solutions to the solar industry.

The efficiency of organic solar cells has rapidly improved over the last decade; see Figure 1-2. In 2012, the state-of-the-art efficiency is 10.6% from a cell made by researchers at UCLA and Sumitomo Chemicals.[6] Most of the high-efficiency organic photovoltaic cells today are tandem structures, where two cells absorbing different parts of solar spectrum are stacked in series. Tandem cells have better efficiencies, but the electric currents of the two constituent cells should be matched and the manufacturing steps become challenging and complicated.

This thesis concerns a way to construct an effective tandem cell in a *single-junction* cell structure, which is expected to improve efficiencies at a low cost. We utilize an energy transfer process that allows a solar cell to convert a photon into two electrons—called singlet exciton fission.

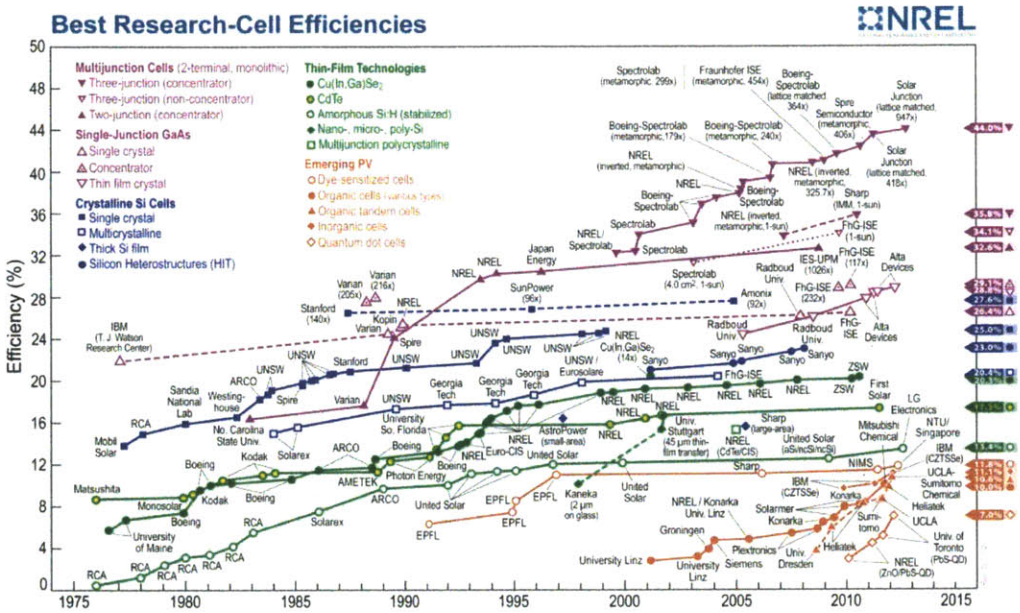

Figure 1-2 Best research-cell efficiencies. Taken from www.nrel.gov.

2. Fundamentals of Organic Solar Cells

Here we summarize essentials for understanding fundamental electronic processes and device operation principles in organic solar cells. The following material was written mostly based on the lecture note of Ref. 7, Ref. 8, and Ref. 9.

2.1 Excitons

Perhaps a key characteristic that distinguishes organic semiconductors from inorganic materials is an excitonic effect. An exciton is a pair of an electron and a hole that are bound by Coulombic attraction.[8] Conventional inorganic semiconductors have large dielectric constants and, therefore, shield electron-hole interactions efficiently. In contrast, organic molecules typically have a small dielectric constant; thus their exciton binding energies are on the order of a few hundred meV, much bigger than kT at room temperatures.[10] This unique excitonic characteristic is where a lot of challenges and fascinating effects of organic semiconductor technologies—including this thesis's topic, singlet exciton fission—begin.

2.1.1 Spin of Excitons

An exciton consists of an electron and a hole, with each having a spin of 1/2. Each particle can have a spin of up or down. Consequently, the two-electron system can have four basis sets: ↑↑, ↓↓, ↑↓, ↓↑. There are three states with a total spin of 1:

$$|s = 1, m = 1\rangle = \uparrow\uparrow$$

$$|s = 1, m = 0\rangle = (\uparrow\downarrow + \downarrow\uparrow)/\sqrt{2}$$

$$|s = 1, m = -1\rangle = \downarrow\downarrow,$$

where s is the total spin number and m is the spin quantum number.[11] These three states are called "triplets," as there are three states. Note that triplet states are symmetric under particle exchange. A state with a total spin of 0 is called a singlet[11]:

$$|s = 0, m = 0\rangle = (\uparrow\downarrow - \downarrow\uparrow)/\sqrt{2}$$

Note that a singlet state is anti-symmetric under particle exchange. Only the optical transition between the same total spin, *i.e.* singlet → singlet or triplet → triplet, is allowed.

2.1.2 Fluorescence and Phosphorescence

First, we will show why the total spin should be preserved during optical transitions. The transition dipole moment, which predicts whether a transition from an initial state $|i\rangle$ to a final state $|f\rangle$ is possible, is given by:

$$\mu = \langle f | -e\mathbf{r} | i \rangle \tag{2.1}$$

where **r** is the position of a particle with respect to the coordinate system. Let us apply the inversion operation, i.e. $\mathbf{r} \rightarrow -\mathbf{r}$. The transition dipole should not change the sign; thus $|i\rangle$ and $|f\rangle$ should have different symmetry under inversion.

The electric dipole moment operator for a two-electron system is $-e\mathbf{r}_1 - e\mathbf{r}_2$. This operator is symmetric under particle exchange. Let us construct spatially symmetric (Ψ_+) and anti-symmetric (Ψ_-) wavefunctions under particle exchange:

$$\begin{aligned} \psi_+ &= \frac{1}{\sqrt{2}}\{HOMO(1)LUMO(2) + LUMO(1)HOMO(2)\} \\ \psi_- &= \frac{1}{\sqrt{2}}\{HOMO(1)LUMO(2) - LUMO(1)HOMO(2)\} \end{aligned} \tag{2.2}$$

where HOMO is the highest occupied molecular orbital and LUMO is the lowest unoccupied molecular orbital.

The dipole moment for the transition between states of different symmetry is

$$\mu = -e\langle \psi_+(\mathbf{r}_1,\mathbf{r}_2) \,|\, (\mathbf{r}_1 + \mathbf{r}_2) \,|\, \psi_-(\mathbf{r}_1,\mathbf{r}_2)\rangle \tag{2.3}$$

This dipole moment changes its sign under particle exchange. Since the dipole moment cannot depend on the labelling of electrons, it must be zero. This concludes that only the optical transition between the states of the same symmetry is allowed.

The Pauli exclusion principle states that the total wavefunction for two identical fermions is anti-symmetric with respect to an exchange of the particles. The total wavefunction is composed of a spatial factor and a spin factor. We showed that the spatial symmetry should not change during optical transitions. This means that optical transitions do not alter symmetry of the spin wavefunction. In other words, only the

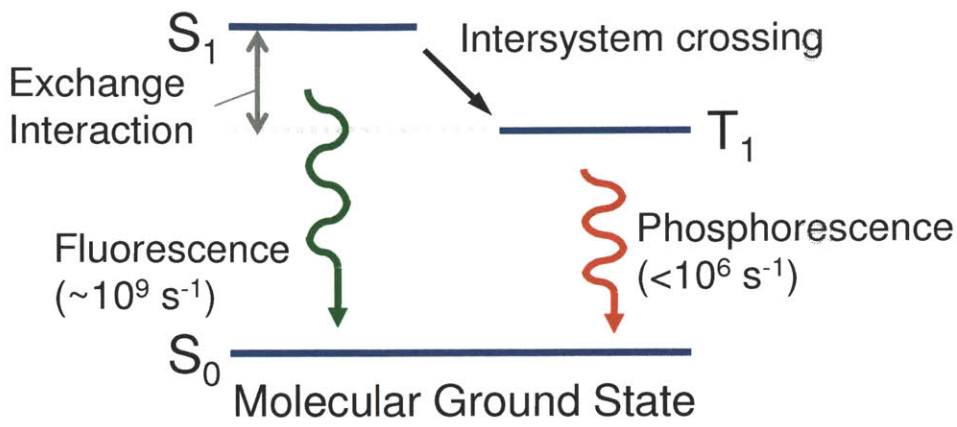

Figure 2-1 Spin-dependent energy transfer process in molecules

transitions maintaining the total spin, *i.e.* singlet → singlet or triplet → triplet, are possible.

The molecular ground state is usually a HOMO filled with two electrons. The filled HOMO spatial wavefunction is symmetric under particle exchange; therefore, the ground state is a singlet. The decay of a singlet exciton into a ground state is spin-allowed; thus, this process occurs quite rapidly on the timescale of several nanoseconds and the emitted light is called fluorescence (see Figure 2-1). The transition from a triplet excited state into a ground state is spin-forbidden and, in some molecules, as slow as a few seconds.[12] Certain processes, such as spin-orbit coupling, may mix singlet and triplet states, making the decay of triplet excited states emissive. This weakly allowed transition, called phosphorescence, can be as fast as several microseconds.

Singlet and triplet excited states are non-degenerate in terms of energy due to electron-electron interactions. The Coulomb integral J is defined by:

$$J = \frac{e^2}{4\pi\varepsilon}\left\langle HOMO(1)LUMO(2)\,|\,\frac{1}{r_{12}}\,|\,HOMO(1)LUMO(2)\right\rangle \tag{2.4}$$

and the exchange integral K is defined by:

$$K = \frac{e^2}{4\pi\varepsilon}\left\langle HOMO(1)LUMO(2)\,|\,\frac{1}{r_{12}}\,|\,HOMO(2)LUMO(1)\right\rangle \tag{2.5}$$

Electron-electron interaction for wavefunctions which are symmetric in space and anti-symmetric in spin under particle exchange is obtained by:

$$\begin{aligned} E_+ &= \frac{e^2}{4\pi\varepsilon_0}\left\langle \psi_+\,|\,\frac{1}{r_{12}}\,|\,\psi_+\right\rangle \\ &= \frac{e^2}{4\pi\varepsilon_0}\left\langle \frac{1}{\sqrt{2}}\{H(1)L(2)+L(1)H(2)\}\,|\,\frac{1}{r_{12}}\,|\,\frac{1}{\sqrt{2}}\{H(1)L(2)+L(1)H(2)\}\right\rangle \\ &= J + K \end{aligned} \tag{2.6}$$

where H and L denote the HOMO and LUMO, respectively. Similarly, the energy for spatially anti-symmetric wavefunctions is:

$$\begin{aligned} E_- &= \frac{e^2}{4\pi\varepsilon_0}\left\langle \psi_-\,|\,\frac{1}{r_{12}}\,|\,\psi_-\right\rangle \\ &= \frac{e^2}{4\pi\varepsilon_0}\left\langle \frac{1}{\sqrt{2}}\{H(1)L(2)-L(1)H(2)\}\,|\,\frac{1}{r_{12}}\,|\,\frac{1}{\sqrt{2}}\{H(1)L(2)-L(1)H(2)\}\right\rangle \\ &= J - K \end{aligned} \tag{2.7}$$

Hence the triplet state is lower in energy than the singlet state. The energy gap between the singlet and triplet states is called the exchange energy.

2.2 Electronic Transition Principle

2.2.1 The Born-Oppenheimer approximation

Unfortunately, most electronic states in molecules are complex, and its Schrödinger equation cannot be solved analytically. The Born-Oppenheimer approximation allows us to overcome this difficulty by taking advantage of the fact that electrons are much lighter than nuclei. Due to the mass difference, the electrons can respond almost instantaneously to the movement of the nuclei. Therefore, it is possible to fix the nuclei in position and solve the Schrödinger equation for the electrons in the static electric potential formed by given nuclear arrangement. The Born-Oppenheimer approximation is used in the Franck-Condon principle, an essential theory for explaining molecular absorption and fluorescence spectra.

2.2.2 The Franck-Condon principle

When an electronic transition, *e.g.* photoexcitation of a molecule, occurs, the nuclei configuration is transformed by a Coulombic force as a result of the redistribution of electrons. The nuclei undergo vibration and the absorption spectrum shows the vibrational energies of molecules. This vibronic transition—simultaneous electronic and vibrational transitions—can be analyzed by the Franck-Condon principle.

The Franck-Condon principle assumes the stationary nuclear framework during electronic transition. Figure 2-2 describes the electronic transition from the ground state to the first excited state. Note that the excited state curve is typically displaced to the right relative to the ground state curve because the excited state has more antibonding character. Under the Born-Oppenheimer approximation, the transition should happen

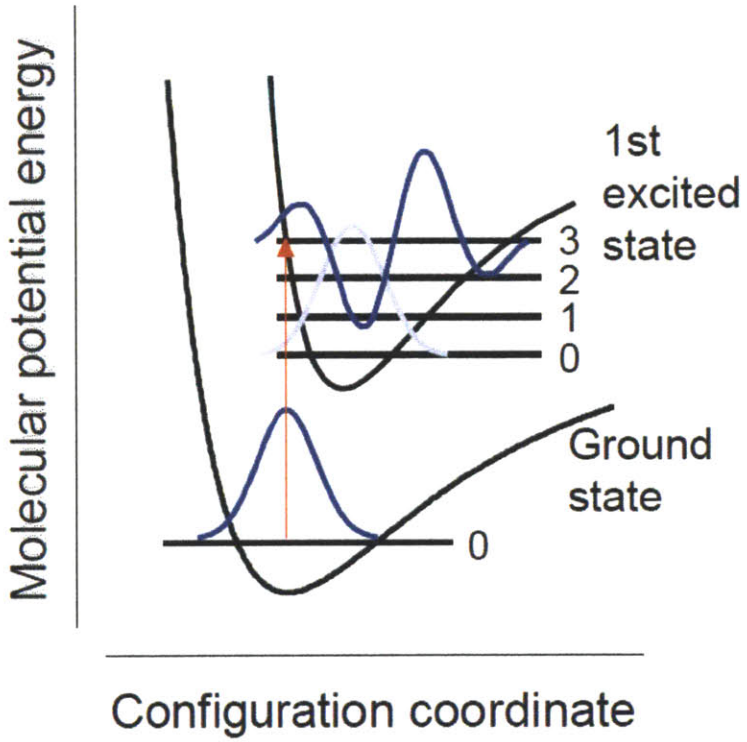

Figure 2-2 The ground vibrational state makes a transition to the first excited state with a vibrational state that most strongly resembles the initial vibrational wavefunction. Taken from Ref. 7. Adapted from Atkins and Friedman.

without changing the nuclear configuration coordinate. Therefore, the transition occurs from the ground vibrational state in the lower state to the vibrational state in the excited state that maximizes the overlap of the wavefunctions.

2.3 Marcus Electron Transfer

The Marcus theory of electron transfer is an extremely useful concept to explain various electron transfer reactions in organic devices—charge transport, charge transfer at the donor-acceptor interface, charge recombination, and singlet exciton fission.

In a solid bonded by van der Waals forces, the intermolecular interaction is not significant enough to form an electronic band, which is commonly created in covalently bonded inorganic crystals. Thus, the movement of charges is best described by *hopping* from one molecule to the next. As the molecules are weakly bonded in an organic solid, the potential associated with a charge carrier distorts local crystal lattices. We call an electron combined with the local lattice distortion a *polaron*. Under the Born-Oppenheimer approximation, the electron responds much quicker than the associated nuclear rearrangement. Therefore, we can assume that the nuclear reconfiguration limits the charge transfer reaction.

Let us write the energy of an electron sitting on a molecule as a function of x, the deviation of the molecule from the original configuration:

$$E = E_0 - Ax \tag{2.8}$$

where E_0 is the increase in energy gained by having an excess charge on the molecule. The new charge that comes into the molecule changes the nuclear arrangement, forming a polarization field. The constant A describes the energy relaxation caused by the polarization dipole. Furthermore, the lattice distortion increases the energy of the molecule and we can describe it as a spring with the spring constant K:

$$E = \frac{1}{2}Kx^2 \tag{2.9}$$

Therefore, the total energy combining the nuclear and electronic effects is

$$E = E_0 - Ax + \frac{1}{2}Kx^2 \tag{2.10}$$

The distortion at equilibrium is found to be at the minimum of Eq. (2.10): $\bar{x} = A/K$. The total energy of an electron and a molecule at equilibrium is

$$E(\bar{x}) = E_0 + E_b \tag{2.11}$$

where E_b is the binding energy given by

$$E_b = -\frac{A^2}{2K} \tag{2.12}$$

Now we consider one molecule with the ground state energy E_1 and the neighboring molecule with the ground state energy E_2. The charge transfer occurs when the electronic levels of the two molecules are resonant:

$$E_1 + E_0 - Ax_1 = E_2 + E_0 - Ax_2 \tag{2.13}$$

The total energies of the first and second molecules are

$$\begin{aligned} U_1 &= \frac{1}{2}Kx_1^2 + E_0 - Ax \\ U_2 &= \frac{1}{2}Kx_2^2 \end{aligned} \tag{2.14}$$

The total energy U_1+U_2 given the constraint of Eq. (2.13) is minimized at $x_1 = \frac{A}{2K} - \frac{\Delta}{2A}$ with $\Delta = E_2 - E_1$. The total energies for the two molecules are

$$U_1 + U_2 = \frac{(\Delta - 2E_b)^2}{8E_b} + E_0 + E_b \tag{2.15}$$

The change in total energy provides the activation energy given by

$$E_A = (U_1 + U_2) - (E_0 + E_b) \tag{2.16}$$

The hopping rate k is exponentially dependent on the activation energy:

$$k \propto \exp\left[\frac{-E_A}{k_B T}\right] \tag{2.17}$$

Often it is convenient to define a reorganization energy as twice the binding energy, *i.e.* $\lambda = 2|E_B|$, and the final expression for Marcus electron transfer is obtained:

$$k \propto \exp\left[\frac{-(\Delta + \lambda)^2}{4\lambda k_B T}\right] \tag{2.18}$$

It is possible to graphically understand the Marcus electron transfer. The two curves shown in Figure 2-3 represent the energy of the electron donor and acceptor molecules against a common configuration x_1. Charge transfer occurs when the energies of the donor and acceptor are equal. The difference of the ground state energy Δ can be induced by applying an electric field: $\Delta = aqF$. When no electric field is applied, the activation barrier is $\lambda/4$. As the electric field increases, charge transfer becomes faster until the transfer becomes resonant. However, further increases in the electric field after the resonant point slow down electron transfer; this regime is called the 'Marcus inverted' region.

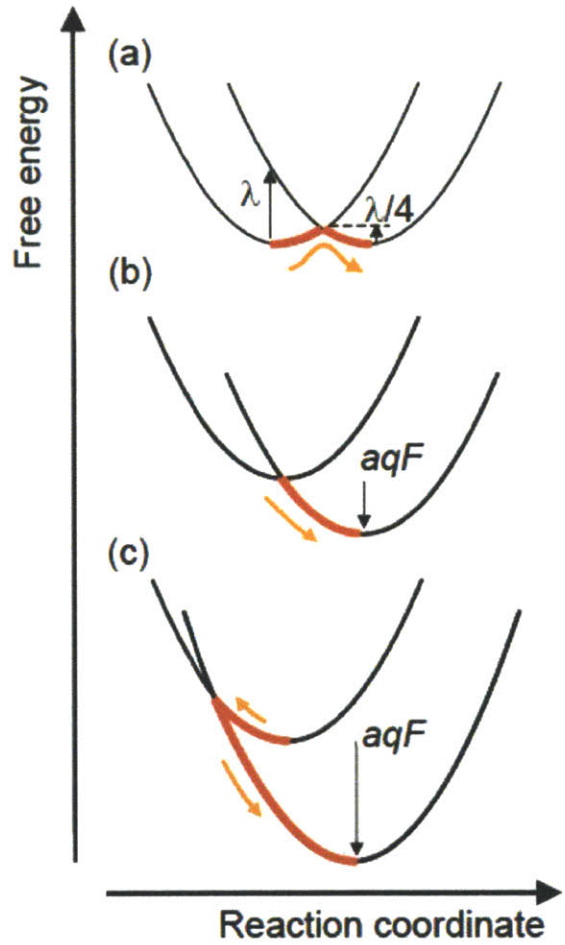

Figure 2-3 Charge transfer in the Marcus theory. **(a)** No electric field is applied. **(b)** No activation barrier is required and the charge transfer rate is at maximum. **(c)** As the electric field increases further, the rate starts to drop. This regime is called 'Marcus inversion'. Taken from Ref. 7

2.4 Operation of Organic Solar Cells

Figure 2-4 illustrates the power conversion process of organic solar cells. Photon absorption creates a bound electron-hole pair, or exciton. In organic molecules, the

exciton has a high binding energy up to 1eV and therefore cannot be dissociated by the internal electric field. The excitons diffuse toward the donor-acceptor (DA) heterojunction. The energy offset at the DA interface dissociates the strongly bound excitons in organic molecules with near unity efficiency. Excitons are separated into charge transfer states, which are bound electron-hole pairs across the DA junction. The charge transfer states can be dissociated into free carriers, which ultimately generate photocurrent.

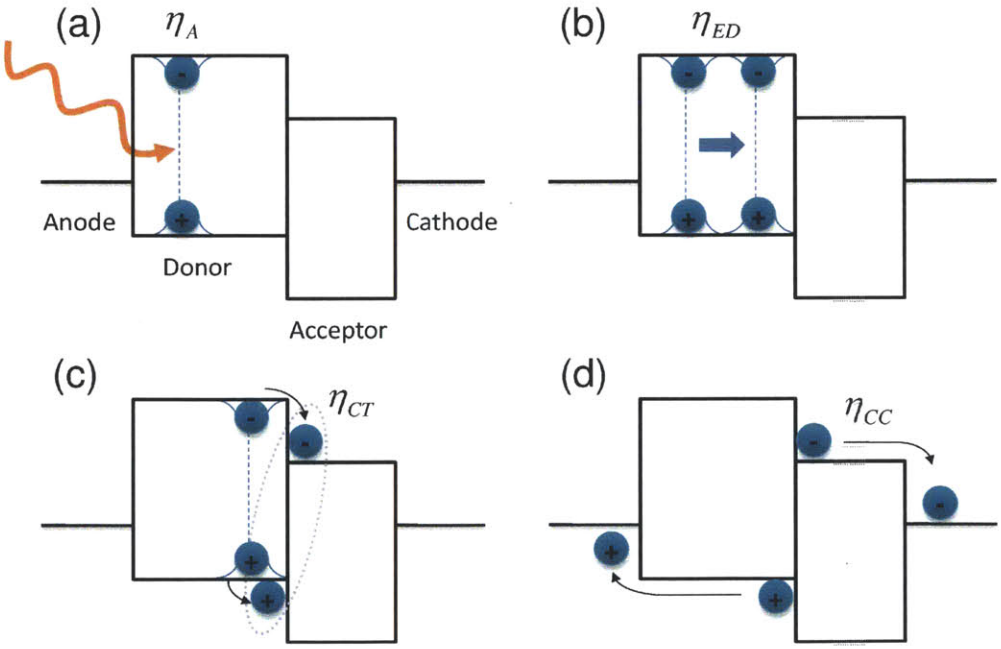

Figure 2-4 The operating principle of organic bilayer solar cells. **(a)** Upon light absorption, an exciton is created. **(b)** Excitons diffuse to the interface. **(c)** Excitons are dissociated into charges at the donor-acceptor interface. **(d)** Charges are extracted to the electrodes.

3. Potentials of Singlet Exciton Fission

Singlet fission, a process that splits a singlet (spin 0) exciton into two triplet (spin 1) excitons, promises to allow for photovoltaics with efficiencies beyond the Shockley-Queisser (SQ) limit.[13] In a conventional single-junction solar cell, an electron-hole pair photoexcited with energy above the bandgap loses its extra energy via thermalization.[14] Singlet exciton fission instead splits a high-energy excited state into two low-energy states, generating one extra exciton per absorbed photon, which would have been otherwise wasted as heat.

Although the transition between singlet and triplet states is disallowed by the conservation of spin symmetry, a pair of triplets can have some singlet character[8]; therefore, singlet fission, the conversion of a singlet into a pair of triplets, can be a spin-allowed process.[13] If the energy of the singlet exciton is higher than or comparable to twice the energy of the triplet, singlet fission can be very fast, outcompeting other decay channels, including prompt fluorescence.[13]

The triplet excitons produced by fission have roughly half the energy of the initial singlet excitation. Consequently, fission limits the open circuit voltage of the cell to no more than half its previous value. Triplet excitons are, however, also dark states; the absorption in the spectral region between the singlet and triplet excitons is spin-forbidden. This empty absorption region must be filled by adding another material that

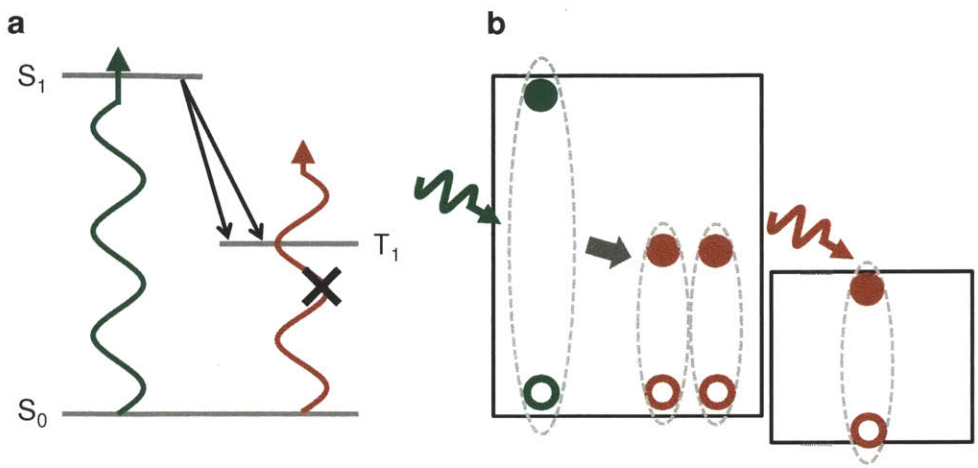

Figure 3-1 **(a)** Energetic structure and state transition in singlet fission materials. Photoexcitation of singlets splits into pairs of triplet states. The wavelength range between the singlet and triplet states is not optically accessible. **(b)** A device structure example of singlet-exciton-fission-based solar cells. The donor layer performs singlet fission, where a high-energy photoexcitation splits into two triplet excitons. The acceptor layer absorbs low-energy photons and has the bandgap similar to the triplet energy of the donor.

captures low-energy photons; see Figure 3-1a. Otherwise, the singlet-fission photovoltaic system will double the photocurrent, but also cut the voltage by half, leading to no net benefit in the power conversion efficiency. See Figure 3-1b for an example of device structures featuring singlet fission donors and low bandgap acceptors. As shown in Figure 3-2, singlet fission solar cells with absorption in the singlet-triplet gap can bring the SQ limit to 41% from 33% of conventional single-junction solar cells.[13, 14]

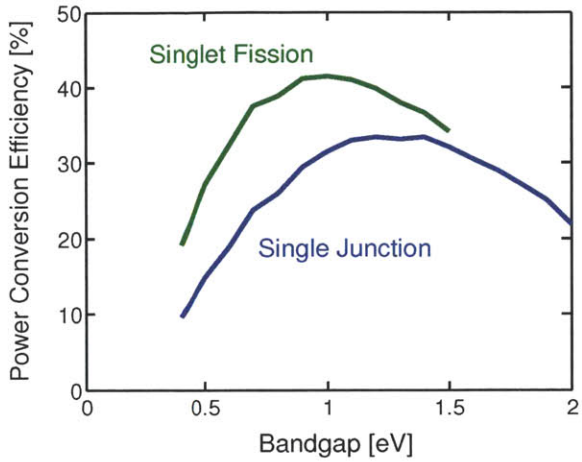

Figure 3-2 Theoretical maximum power conversion efficiency as a function of bandgap (S_1–S_0 for single-junction; T_1–S_0 for singlet fission) for single-junction (blue) and singlet fission (green) solar cells.

4. Singlet-exciton-fission-based Photodetectors

We employ an exciton fission process that converts one singlet exciton into two triplet excitons to increase the quantum efficiency of an organic multilayer photodetector beyond 100%. The photodetector incorporates ultrathin alternating donor-acceptor layers of pentacene and C_{60}, respectively. By comparing the quantum efficiency after separate pentacene and C_{60} photoexcitation we find that singlet exciton fission in pentacene enhances the quantum efficiency by (45±7)%. In quantitative agreement with this result, we also observe that the photocurrent generated from pentacene excitons is decreased by (2.7±0.2)% under an applied magnetic field of $H = 0.4$T, while the C_{60} photocurrent is relatively unchanged.

4.1 Introduction

Organic optoelectronic devices are compatible with flexible plastic substrates and low-cost manufacturing processes.[15] Within this broad family of devices, efficient organic photodetectors have been investigated for applications in medical imaging and large area optical detectors. Peumans *et al.* reported multilayer organic photodetectors with external quantum efficiencies of 75% across the visible spectrum using ultrathin (~5 Å) electron

donor and electron acceptor layers.[16] The narrowness of each layer minimizes losses during exciton diffusion to a charge generation site at an interface between the donor and acceptor materials. Using multiple layers maintains the optical absorption of the photodetector, however, the layers also trap charge carriers, and a strong external electric field is required to drive the carriers out of the device.

In the present work, we enhance the efficiency of an organic multilayer photodetector by employing exciton fission. In pentacene, the energy of the first singlet exciton $E(S_1) = 1.83$ eV is more than twice the energy of the first triplet exciton $E(T_1) = 0.86$ eV.[17] Thus, the spin-allowed transition of a singlet exciton into two triplets $S_1 \rightarrow 2T_1$, called singlet fission,[18] is energetically possible in pentacene without thermal excitation and occurs rapidly (< 1 ps) (See Figure 4-1).[17],[19] If charge transfer occurs after singlet exciton fission, one photon can lead to two carriers, potentially doubling the quantum efficiency.

4.2 Device Structures

To exploit singlet exciton fission, we built a multilayer photodetector composed of pentacene and C_{60} for donor and acceptor, respectively, as illustrated in Figure 4-1. Each pentacene and C_{60} layer is 2-nm and 1-nm-thick, respectively; thin enough to allow efficient exciton separation and charge extraction. There are 30 pentacene/C_{60} bilayers in total, yielding an optically active thickness of 90nm. Devices were fabricated on precleaned glass substrates coated with indium tin oxide (ITO) and poly(3,4-ethylenedioxythiophene): poly(4-styrenesulphonate) (PEDOT:PSS). Inserting a buffer layer of PEDOT:PSS on the anode reduces the dark current at a reverse bias by an order

of magnitude and aids charge extraction by increasing the built-in potential, as investigated in Ref. [20]. All other layers were deposited by thermal evaporation at high vacuum ($< 3\times10^{-6}$ Torr). The silver cathode was defined by a 1-mm-diameter shadow mask.

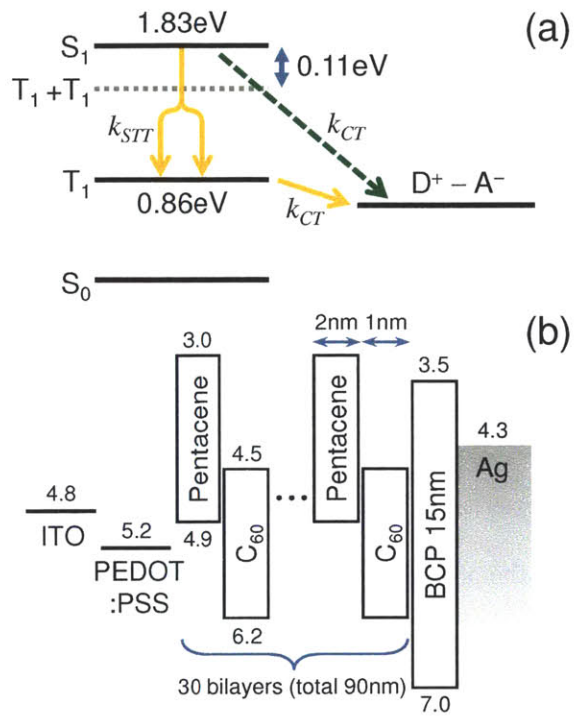

Figure 4-1 **(a)** Energy transfer process in a pentacene/C_{60} photodetector. A singlet exciton created upon photoexcitation of pentacene undergoes singlet exciton fission with a rate of k_{STT} (< 1 ps), leading to two triplet excitons. They are separated at the pentacene/C_{60} heterojunction at a charge transfer rate of k_{CT}, generating photocurrent (solid arrow). Singlet excitons in pentacene can also undergo direct charge transfer (dotted arrow). **(b)** Schematic energy-level diagram of a pentacene/C_{60} multilayer photodetector. The energy levels are from Ref. 21, 22, and 23. Note that the lowest unoccupied molecular orbital of C_{60} is calculated from optical absorption measurements.

4.3 Experiment Setup

The spectral quantum efficiency was measured by using a xenon lamp with a monochromator, chopped at ~90 Hz, and a lock-in amplifier. The incident light intensity was measured using a calibrated silicon photodiode and the current-voltage characteristics were recorded using a semiconductor parameter analyzer. Complex refractive indices of modeled thin films were characterized by measuring thin-film reflection and transmission. All devices were packaged in a nitrogen atmosphere before measurement.

4.4 Efficiency of Singlet Exciton Fission

Figure 4-2 shows the external quantum efficiency (EQE, η_{EQE}) at a voltage bias of $V = -3.5$ V compared to the absorption of the optically active layers. We fitted the EQE spectrum using optical interference modeling,[9] obtaining internal quantum efficiencies (IQE) of (128±2)% and (89±4)% for pentacene and C_{60}, respectively. Optical parameters were obtained from reflectance and transmittance measurements of organic multilayer films grown simultaneously with the active layers of the devices. Assuming that all photogenerated excitons are dissociated in the multilayer structure, and that the charge extraction efficiency is independent of the source of the excitons, the comparison between the IQE of pentacene and C_{60} suggests that singlet exciton fission in pentacene enhances the EQE by $\eta_{STT} = (145\pm7)\%$. In previous work on pentacene/C_{60} photovoltaic cells, Yoo *et al.* observed a high IQE of 87% at short-circuit conditions under specific

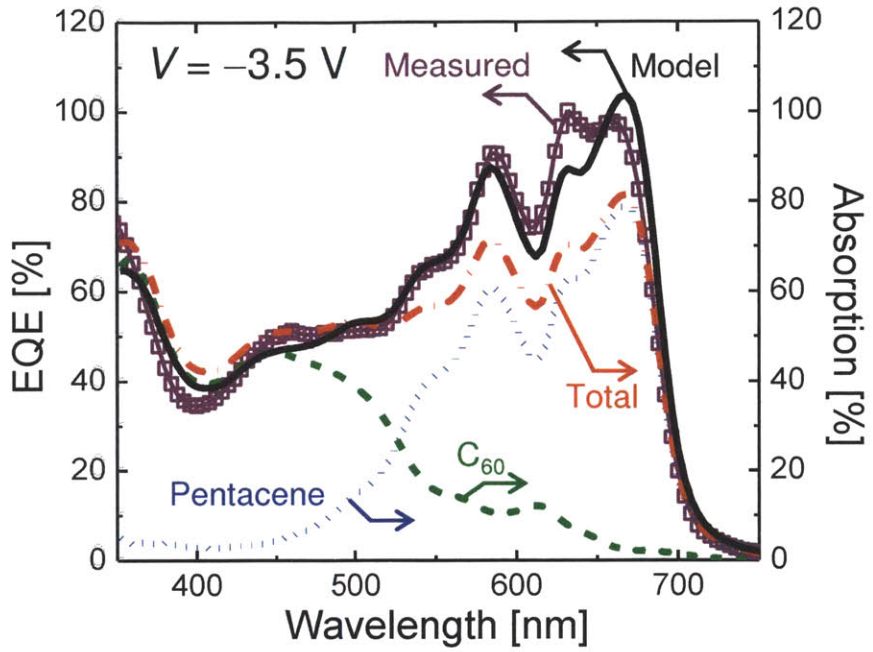

Figure 4-2 The external quantum efficiency (EQE) spectrum at a voltage of V = −3.5V and absorption spectrum of a pentacene/C_{60} multilayer device. The absorption of pentacene (dotted line), C_{60} (dashed line), and both layers (dash-dot line) are shown. The absorption inside the device structure was acquired using optical interference modeling. The EQE was fit using internal quantum efficiencies of (128±2)% and (89±4)% for pentacene and C_{60}, respectively, implying that the efficiency enhancement from singlet exciton fission is (145±7)%.

illumination of pentacene.[21] We presume this result also may be influenced by singlet exciton fission.

Figure 4-3a is a plot of the peak EQE as a function of the applied voltage at a wavelength of 660nm or 450nm, where pentacene or C_{60} dominates the absorption, respectively. At $V \sim -3.5$V, where the EQE of pentacene first exceeds 100%, the dark current is less than 25% of the photocurrent; see Figure 4-3b. But at higher reverse bias

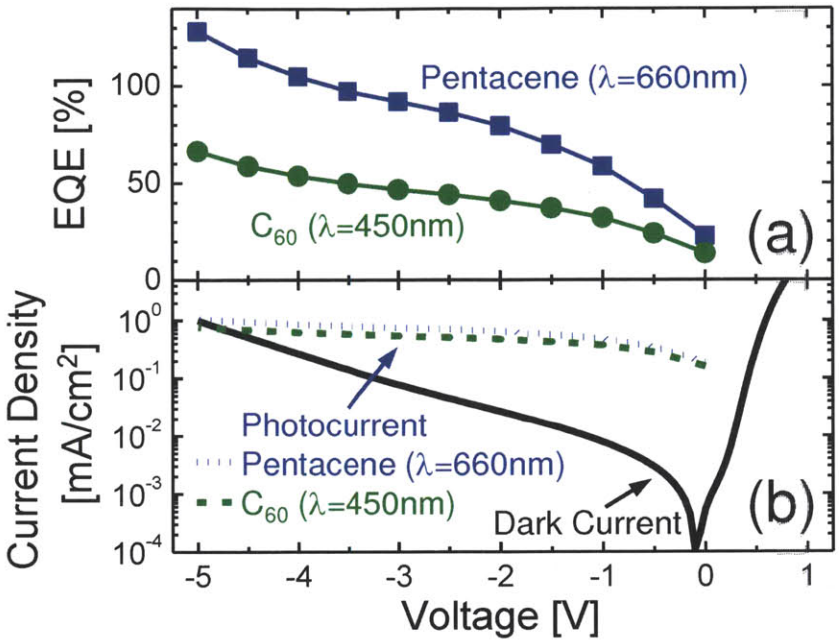

Figure 4-3 (a) The external quantum efficiency (EQE) as a function of applied voltage. To selectively excite pentacene and C_{60} we employed pump wavelengths of $\lambda = 660$nm (squares) and $\lambda = 450$nm (circles), respectively. **(b)** The current-voltage characteristics in the dark (solid) and under illumination at $\lambda = 660$nm (dotted) and $\lambda = 450$nm (dashed). The incident light intensity was chosen to approximately equalize the photocurrent densities and was 1.54mW/cm^2 and 3.21mW/cm^2 for $\lambda = 660$nm and $\lambda = 450$nm, respectively.

($|V| > 3.5$V), the photocurrent is similar to the dark current, and we cannot distinguish the increase in the EQE in this region from bulk photoconductive gain in pentacene.[24]

4.5 Magnetic Field Dependence of Photocurrent

Figure 4-4 plots the magnetic field dependence of the photocurrent for the selective illumination of pentacene and C_{60}. Diode lasers at the wavelength of 670nm and 408nm are used for photoexciting pentacene and C_{60}, respectively. The incident light intensity was adjusted using optical density filters to obtain a short-circuit current density of $J = 0.13\text{mA/cm}^2$. The magnetic field was applied parallel to the device plane. Figure 4-4a

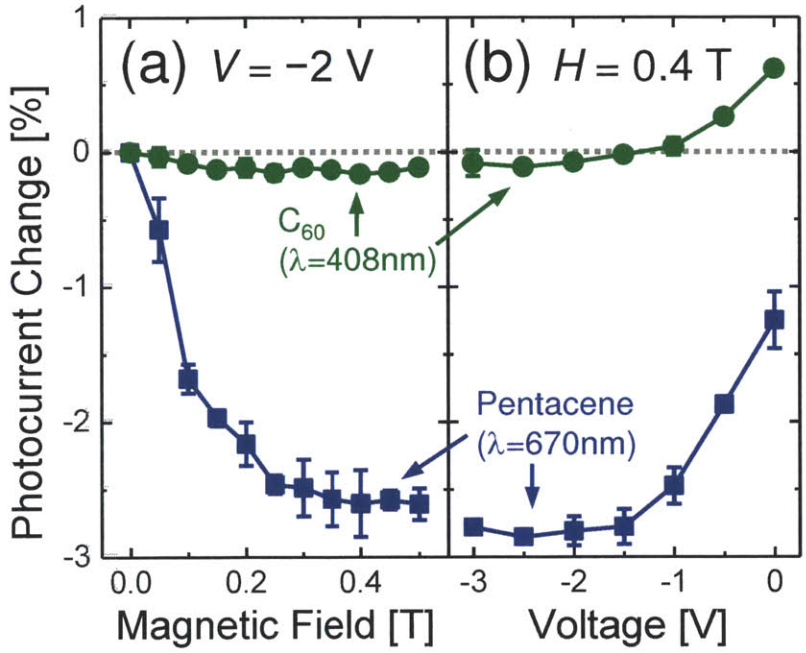

Figure 4-4 **(a)** The change in photocurrent under varying applied magnetic field at a voltage of $V = -2\text{V}$. Laser illumination at $\lambda = 670\text{nm}$ (squares) and $\lambda = 408\text{nm}$ (circles) is used to separately excite the pentacene and C_{60} layers, respectively. The photocurrent decreases by up to 2.7% under illumination of pentacene, confirming the presence of singlet exciton fission in pentacene. **(b)** The change in photocurrent change under a magnetic field of $H = 0.4\text{T}$ at varying reverse bias. The positive trend near short-circuit may be due to modulation of charge recombination rates.

shows the magnetic field dependence of photocurrent for pentacene and C_{60} absorption at a voltage of −2V. Pentacene exhibits a modulation of up to −(2.7±0.2)% whereas the photocurrent change upon C_{60} illumination is negligible.

Johnson and Merrifield's theory accounts for the magnetic field dependence of the exciton fusion process $T_1 + T_1 \rightarrow S_1$ in polyacene crystals.[25] The fission process is the reverse of fusion, having a rate constant nine times that of fusion when no thermal energy is required. In their theory, a singlet is coupled to two triplets via an interacting triplet pair.[26] The fission rate is proportional to the fractional singlet character of the interacting triplet pair which is determined by the triplet-pair spin Hamiltonian incorporating the Zeeman interaction and the triplet-exciton fine structure. As a magnetic field increases ($H > 0.2$T), the Zeeman interaction dominates the spin Hamiltonian and the singlet character of the pair spin states decreases. As a consequence, the fission rate decreases.[18,26]

Figure 4-4b displays the magnetic-field-induced photocurrent modulation as a function of voltage. It is notable that the magnetic field effect becomes more positive as the reverse bias is decreased. Since charge recombination also becomes more significant at low reverse bias, we speculate that the positive magnetic field effect may be due in part to the increased lifetime of triplet charge transfer (CT) states split by the Zeeman interaction.[27] Indeed, this effect has been observed in other organic photovoltaic heterojunctions.[28]

According to the schematic shown in Figure 4-1, the efficiency enhancement factor, η_{STT}, is

$$\eta_{STT}(H) = 2 \cdot \frac{\eta_H(H) k_{STT}}{\eta_H(H) k_{STT} + k_{CT}} + \frac{k_{CT}}{\eta_H(H) k_{STT} + k_{CT}}, \tag{4.1}$$

where the first term represents the charge carriers generated after undergoing singlet exciton fission, and the second term represents the charge carriers generated directly from the singlet exciton. In addition, k_{STT} is the rate of singlet exciton fission into two triplet excitons, k_{CT} is the exciton dissociation rate into a charge transfer state, and $\eta_H(H)$ accounts for the modulation of k_{STT} under an applied magnetic field. In the absence of an applied magnetic field, $\eta_H(H=0) = 1$ and the analysis of Figure 4-2 gives $\eta_{STT} = (145\pm7)\%$. Consequently, we calculate $k_{STT} = (0.8\pm0.2)k_{CT}$. The rate constant k_{STT} in pentacene microcrystalline thin films measured by pump-probe spectroscopy was $1.3\times10^{13}\text{s}^{-1}$.[17] The resulting value of $k_{CT} = 1.6\times10^{13}\ \text{s}^{-1}$ is comparable to the charge transfer rate measured in other organic donor-acceptor heterojunctions.[29]

In crystals of tetracene, another acene closely-related to pentacene, η_H is saturated at high fields ($H > 0.3$T) and varies between $0.75 < \eta_H < 0.9$ depending on the crystal orientation with reference to the magnetic field direction.[30] Since our films do not have a preferential crystal direction, we let $\eta_H(H = 0.4\text{T}) = 0.85$ by averaging $\eta_H(H > 0.3\text{T}, \theta, \phi)$ in all crystal directions. The photocurrent change induced by magnetic field is calculated from Eq. (4.1) to be $\Delta\eta_{STT} = -(2.7\pm0.1)\%$, which agrees well with the measured value presented in Figure 4-4.

4.6 Triplet Dissociation at Pentacene/C_{60} Heterojunction

Because the pentacene triplets have such low energy, $E(T_1) = 0.86$ eV, it has been questioned whether the pentacene/C_{60} donor-acceptor interface separates pentacene triplet excitons into charge. In this section, we review experimental and theoretical evidences from literature that confirm pentacene triplet excitons can dissociate at the C_{60} interface despite their relatively low energy.

The dissociation of pentacene triplets into charge at the pentacene/C_{60} interface has been studied by pump-probe spectroscopy[31] and time-resolved second harmonic generation (TR-SHG) spectroscopy[32]. Rao *et al.* probed the kinetics of triplet excitons and charges in pentacene/C_{60} bilayer films by employing transient absorption spectroscopy.[31] In Figure 4-5a, the photoinduced absorption (PIA) signal integrated over the probe wavelengths of 810–910nm corresponds to the triplet states and charges, although the contribution from triplets dominates. The electroabsorption (EA) signal comes from the electric field generated by charge generation at the heterojunction.[31] The population of charges (the EA signal) grows over 2–10ns as the number of triplets (the PIA signal) decreases.[31]

Chan *et al.* probed transient charge transfer dynamics at the pentacene/C_{60} junction by performing TR-SHG experiments, which detect the local electric field created by electron-hole pairs; see Figure 4-5b.[32] The kinetics of triplet populations at the pentacene/C_{60} interface was also measured by two-photon photoemission (2PPE) spectroscopy.[32] The comparison of TR-SHG and 2PPE signals shows that the charges are created at the same rate as the decay of triplets.[32] Note that the charge generation in this work occurs within a few picoseconds, much faster than what Rao *et al.* observed,

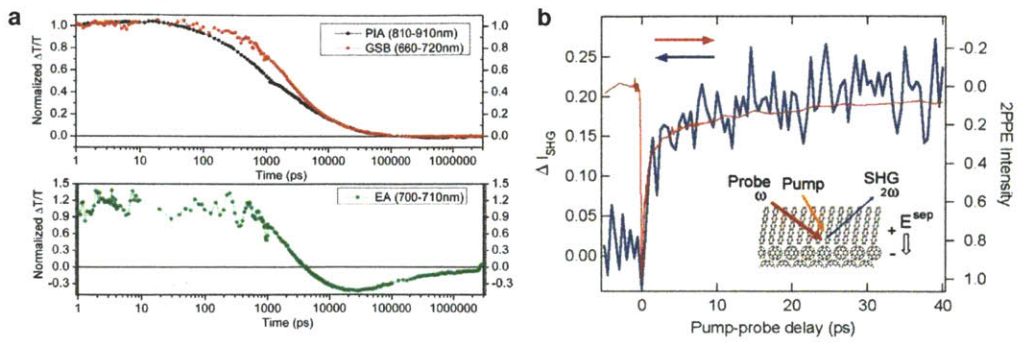

Figure 4-5 (a) Transient absorption dynamics of pentacene/C_{60} bilayers. The decay of the photoinduced absorption (PIA) averaged over the probe wavelengths of 810–910nm (black) is attributed to the decrease of triplet populations. The electroabsorption (EA) signal (green), created by charge generation at the heterojunction, grows as the PIA signal decays. Courtesy of Rao *et al.*[31] **(b)** Second harmonic generation (SHG) intensity (blue) as a function of pump-probe delay from a pentacene/C_{60} bilayer film. SHG probes the transient electric field, established by charge transfer at the donor-acceptor interface. Also shown is normalized two-photon photoemission signal (red) of the triplet state population at pentacene/C_{60} bilayers. Courtesy of Chan *et al.*[32] Both data shown in (a) and (b) suggests that the population of electrons and holes grow at the same rate as the triplets decay.

because the pentacene layer used by Chan *et al.* was almost a monolayer, whereas Rao *et al.* used 150nm-thick pentacene films.

Jadhav *et al.* and Ehrler *et al.* probed the dissociation of pentacene triplet excitons in devices by changing the HOMO level of donors and the LUMO level of acceptors[33, 34]; see Figure 4-6. Collectively, three classes of acceptors were examined in these studies: fullerenes, perylene diimides, and lead selenide (PbSe) and lead sulfide (PbS) nanocrystals (NCs). Jadhav *et al.* also used two types of pentacene molecules to vary the ionization potential of donors: unsubstituted pentacene and diphenyl-pentacene (DPP).[33]

First, triplet exciton dissociation at pentacene/C_{60} interfaces was investigated by examining the contribution from pentacene in EQE spectra; see Figure 4-7a. It is notable that the DPP/C_{60} junction generates very little current from photoexcitation of DPP relative to pentacene in junctions with C_{60}. As DPP has slightly deeper HOMO than pentacene (5.2±0.1 eV versus 4.9±0.1 eV, respectively), the tentative conclusion is that triplets in DPP cannot break up into charges due to the high barrier to charge transfer states.[33] Indeed, when DPP is paired with acceptors with deeper LUMO, such as N,N′-dioctyl-6,12-dicyano-3,4,9,10-tetracarboxyperylene diimide (PDI-CN2) and N,N0-1H,1H-perfluorobutyl dicyanoperylenecarboxydiimide (PDIF-CN2), charge transfer from triplets starts to work again.

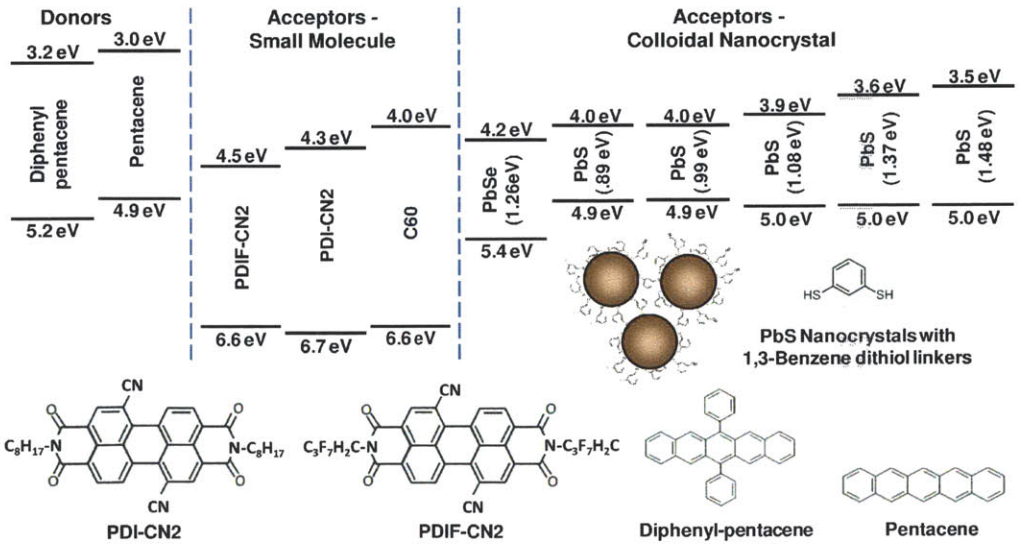

Figure 4-6 A summary of the energy levels and molecular structures used in the study on triplet exciton dissociation by Jadhav *et al.* Courtesy of Jadhav *et al.*[33]

Second, the polarity of magnetic field effect to photocurrent can be employed to probe the dissociation of triplets.[33] As shown in Figure 4-8, pentacene/C_{60} and DPP/PDIF-CN2 junctions, which convert triplets into charges efficiently, show the negative magnetic field effect in the photocurrent, because singlet fission slows down

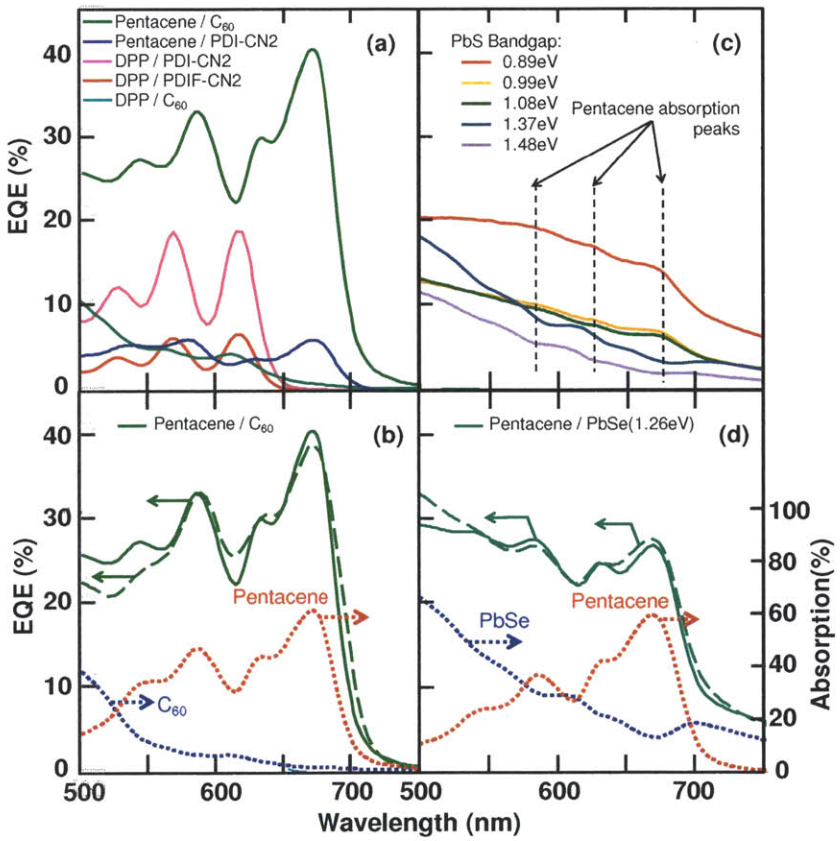

Figure 4-7 (a) Measured EQEs of small molecule acceptor devices. **(b)** Measured (solid) and calculated (dashed) EQEs of a pentacene/C_{60} device. Absorptions from pentacene and C_{60} layers are plotted together. Optical modeling finds that the IQE of pentacene is 63%. **(c)** Measured EQEs of pentacene/PbS nanocrystal devices. **(d)** Measured (solid) and calculated (dashed) EQEs of pentacene/PbSe nanocrystal devices. The IQE of pentacene is determined to be 35%. Courtesy of Jadhav *et al.*[33]

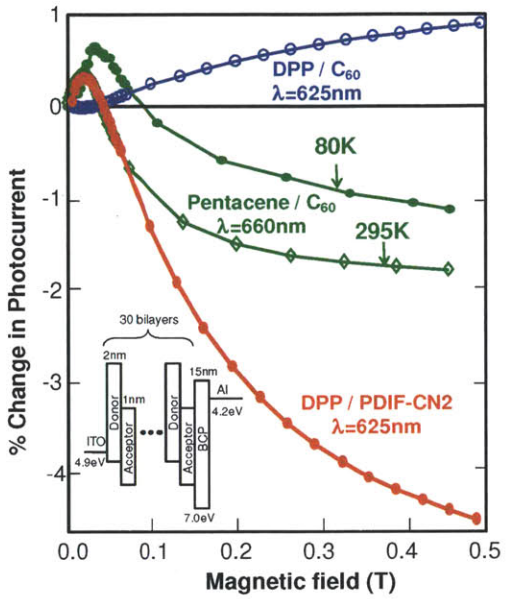

Figure 4-8 Photocurrent changes under magnetic fields for various donor-acceptor multilayer devices. Courtesy of Jadhav *et al.*[33]

under a magnetic field and fewer charges are formed. On the contrary, the DPP/C_{60} interface, where the triplet dissociation is disabled, exhibits a positive magnetic field effect. The reduced rate of singlet fission under applied magnetic field results in more singlet excitons, leading to more charges at the junction where triplets cannot be dissociated.[33]

Beyond the archetypal pentacene/C_{60} junction, Jadhav *et al.* and Ehrler *et al.* both studied junctions between pentacene and infrared-absorbing NCs.[33, 34] Figure 4-9a shows the pentacene/PbSe NC device structure and the EQE spectra with varying NC bandgaps in Ref. 34. The presence of the pentacene absorption in the EQE means that the excited state in pentacene has sufficient energy to dissociate at the donor-acceptor heterojunction.[34] By detecting the pentacene contribution from the EQE data, Ehrler *et al.*

showed that the pentacene triplet energy is at least 0.85eV and at most 1.00eV in operating devices.[34] As shown in Figure 4-7c–d, Jadhav *et al.* observed a similar phenomenon in the EQE of pentacene/PbS NC devices with varying NC LUMO levels.[33] The contribution to photocurrent from pentacene absorption changes from positive to negative as the LUMO level of the acceptor increases.

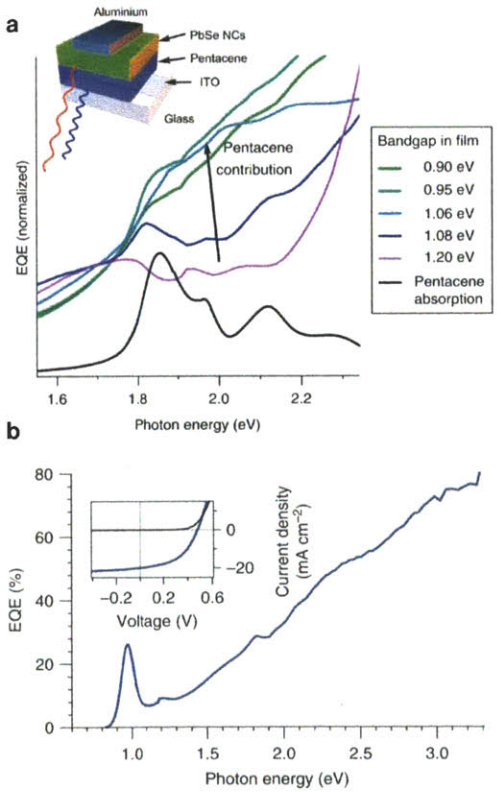

Figure 4-9 (a) Normalized external quantum efficiency spectra of pentacene solar cells prepared with a size series of PbSe NCs. A contribution from pentacene is observed in devices with NCs up to 1.08eV, indicated with an arrow. The inset shows the device structure studied. **(b)** EQE of the best PbSe-pentacene device. The inset shows the current-voltage data with a power conversion efficiency of 4.7% under AM 1.5G illumination. The NC bandgap in the film is 0.98eV. Courtesy of Ehrler *et al.*[34]

Figure 4-10 summarizes the relations between the CT energy and the effectiveness of triplet dissociation.[33] The junctions dissociating triplets are colored in blue and those not dissociating are represented in red. It was found that the pentacene/C_{60} interface is sensitive to small changes in the donor and acceptor energy levels, suggesting that pairing with proper acceptors is significant when studying pentacene derivatives.[33]

Theory also suggests that the pentacene/C_{60} junction is capable of dissociating pentacene triplet excitons. Jadhav *et al.* calculated the charge transfer (CT) state using constrained density functional theory.[33, 35] As shown in Figure 4-11, the CT state energy was computed to be 0.9–1.0 eV for the head-to-tail geometry, potentially low enough to break up the pentacene triplet state.[33] The face-to-face geometry is predicted to have a CT

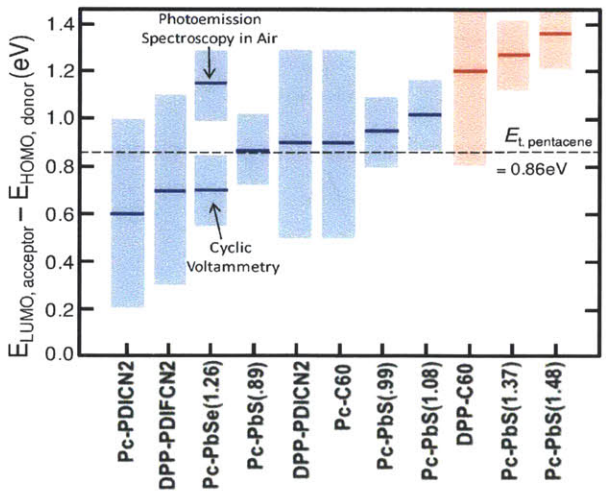

Figure 4-10 $E_{LUMO,acceptor}-E_{HOMO,donor}$, approximate energy of charge transfer states, for various donor-acceptor heterojunctions. Blue indicates that the EQE measurement and magnetic field effects in photocurrent confirmed the dissociation of triplets of those junctions, while red means that triplets cannot be separated into charges. Courtesy of Jadhav *et al.*[33]

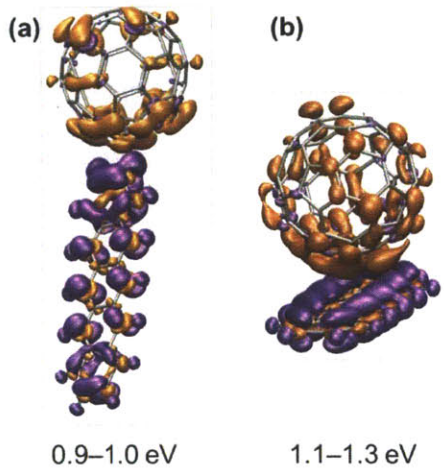

Figure 4-11 Calculated charge transfer state energies for pentacene-C_{60} donor-acceptor pairs in (a) head-to-tail and (b) face-to-face configurations. Courtesy of Jadhav *et al.*[33]

state energy of 1.1–1.3 eV, not low enough to separate the pentacene triplet.[33] The calculation supports the conclusion that the pentacene triplet and the pentacene/C_{60} CT state are roughly isoenergetic.[33]

Finally, it is important to note that pentacene/C_{60} bilayer solar cells show high EQEs up to ~70%[36]. Considering that the pentacene triplets are formed almost instantaneously (~80 fs) after photoexcitation[32, 37, 38], such high efficiencies are hard to explain if the photocurrent is only created by residual pentacene singlet exctions.

4.7 Conclusion

To summarize, we improved the quantum efficiency of organic photodetectors by utilizing singlet exciton fission in pentacene. We measure an exciton multiplication factor of (145±7)%. The photocurrent reduction of −2.7% during selective illumination of pentacene under a magnetic field confirms the presence of singlet exciton fission in

pentacene/C_{60} multilayer heterojunctions. These results suggest that singlet exciton fission can be employed to improve the quantum efficiency of various organic photodiodes including photodetectors, photovoltaics and dye-sensitized solar cells.

5. Singlet-exciton-fission-based organic photovoltaic cells with external quantum efficiencies above 100%

Singlet exciton fission transforms a molecular singlet excited state into two triplet states, each with half the energy of the original singlet. In solar cells, it promises to double the photocurrent from high energy photons. We demonstrate organic solar cells that exploit singlet exciton fission in pentacene to generate more than one electron per incident photon in a portion of the visible spectrum. Using a fullerene acceptor, a poly(3-hexylthiophene) exciton confinement layer, and a conventional optical trapping scheme, we show a peak external quantum efficiency of (109±1)% at $\lambda = 670$ nm for a 15-nm-thick pentacene film. The corresponding internal quantum efficiency is (160±10)%. Analysis of the magnetic field effect on photocurrent suggests that the triplet yield approaches 200% for pentacene films thicker than 5 nm.

5.1 Introduction

Conventional solar cells generate one electron for each photon that is absorbed. The output voltage is defined by the bandgap, and solar cells waste any excess photon energy

as heat. Summing the thermal loss over the solar spectrum yields the Shockley-Queisser efficiency limit of 34% for solar cells containing a single, optimized semiconductor junction[14].

Splitting excited states, or excitons, generated after the absorption of high energy photons presents one pathway beyond the single junction efficiency limit. Instead of harvesting a single electron, several charges can be obtained by dissociating the child excitons. For example, so-called multiple exciton generation mechanisms have been used to produce an average of more than one electron from an ultraviolet photon with energy four times the bandgap[39].

Singlet exciton fission is a type of multiple exciton generation mechanism found in organic semiconductors[40, 41]. It is notable because spin conservation disallows the usual competing loss process: thermal relaxation of the high-energy exciton into a single low-energy exciton. In fission, the low energy exciton is a dark state, inaccessible by a direct transition from either the high energy exciton or the ground state. Only the evolution of the high-energy state into two dark excitons is spin-allowed. Consequently, prior studies have suggested that singlet fission can be efficient even in the visible spectrum, harnessing photons of just twice the energy of the child excitons[17, 42-46].

There is a side effect of spin in singlet fission, however. The dark exciton controls the electrical properties of the cell. These are decoupled from the optical absorption, which is controlled by the bright, high-energy exciton. Thus, fission does not itself increase the power efficiency of a solar cell. It potentially doubles the photocurrent at the cost of losing at least half the open circuit voltage. To overcome the Shockley-Queisser limit, solar cells could combine fission with a conventional material that fills in the

absorption spectrum above the dark exciton[33, 47-50]. First, however, singlet-fission must demonstrate that it can break the conventional barrier of one electron per photon.

The best understood fission material to date is pentacene, an acene with five rings. Its dynamics are illustrated in Figure 5-1. Optical excitation generates a delocalized spin 0, or singlet, exciton. Within about 80 fs[17, 42-46], the pentacene singlet exciton splits into a

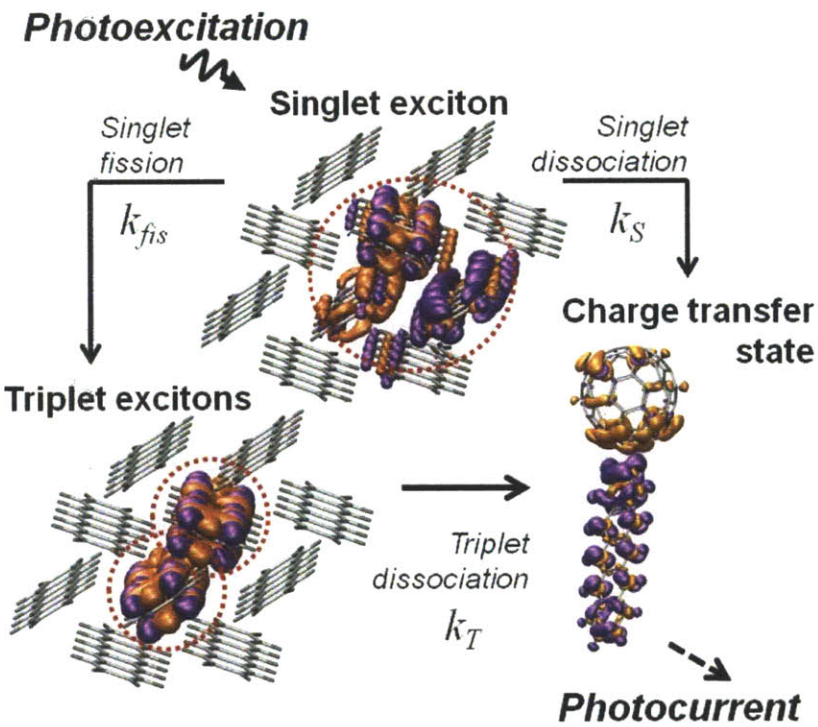

Figure 5-1 A schematic of singlet exciton fission in pentacene based on calculations of the singlet and triplet excitons and charge transfer states at the pentacene/fullerene interface, with the purple (orange) density indicating where less (more) electron density is found in the excited state. The delocalized singlet exciton and two localized triplet excitons are circled in red. The loss pathway for singlet excitons is direct dissociation into charge prior to singlet exciton fission.

pair of spin 1, or triplet, excitons. A pair of triplet excitons can be combined in nine different spin states. As some triplet-pair states have singlet character (total spin of 0), singlet fission is spin-allowed. Under an applied magnetic field, the singlet character of the triplet-pair states is redistributed, changing the number of states with singlet character. Thus, the rate of singlet fission is dependent on the local magnetic field, offering a unique probe of fission dynamics in thin films and devices[25, 33, 41, 47, 51]. Although triplet excitons are dark states, energy may be extracted from them if they are dissociated into charge. This is possible at a junction between pentacene and the fullerene C_{60} when the pentacene is oriented approximately perpendicular to the interface[33].

5.2 Previously Reported Pentacene-based Solar Cells

In pentacene, singlet fission occurs exothermically since the energy of the singlet exciton, $E(S_1) = 1.83$ eV, is slightly higher than twice the triplet energy, $E(T_1) = 0.86$ eV.[52, 53] Singlet exciton fission in pentacene has been observed to occur extremely rapidly, on the order of 80 fs.[37, 38] The ultrafast nature of singlet fission in pentacene enables the efficient conversion of a singlet into two triplets in a photovoltaic device because singlet fission can outcompete or match other decay channels such as singlet exciton dissociation into charge. Indeed, several researchers have observed high external and internal quantum efficiency from pentacene-based photovoltaic cells.

The first high-efficiency pentacene/C_{60} solar cells were reported by Yoo *et al.*, exhibiting high peak external quantum efficiencies (EQEs) up to 69%.[36, 54] Their device structure was indium tin oxide (ITO)/pentacene (50nm)/C_{60} (50nm)/bathocuproine (BCP; 6nm)/Al. Figure 5-2 displays their EQE spectrum and its analysis. Optical interference

modeling revealed that the internal quantum efficiency (IQE), defined as the external quantum efficiency divided by the absorption of active layers, was 85% for pentacene absorption[36]; see Figure 5-2c. While not considering the possibility of singlet fission, the authors determined the exciton diffusion length of ~70nm for pentacene thin films.[36]

Subsequent work by Pandey *et al.* demonstrated EQEs as high as 83% in bulk heterojunction solar cells based on pentacene and N,N′-ditridecylperylene-3,4,9,10-tetracarboxylic diimide (PTCDI-$C_{13}H_{27}$).[55, 56] A 100-nm-thick blend of pentacene and PTCDI-$C_{13}H_{27}$ in the ratio of 3:1 (by wt %) was grown on ITO anodes covered with poly(3,4-ethylenedioxythiophene):poly(styrenesulfonate) (PEDOT:PSS). The cathode was 8nm BCP/60nm Ag. The blend device delivered the maximum EQE of 83%[55]; see Figure 5-3 for the EQE spectrum. The optical modeling shows that the absorption of active layers at λ = 670nm is around 80%,[56] indicating that the IQE is close to 100%.

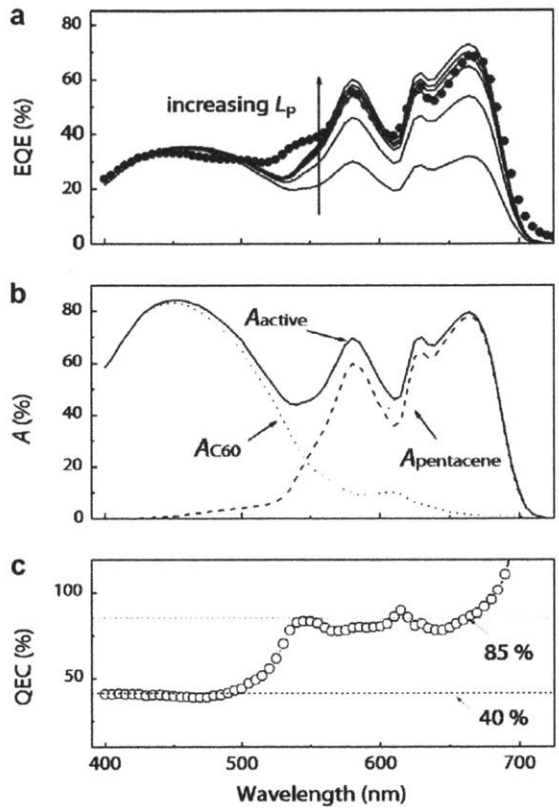

Figure 5-2 External quantum efficiency of pentacene/C_{60} bilayer solar cells. The device structure was ITO/pentacene (50nm)/C_{60} (50nm)/BCP (6nm)/Al. **(a)** Measured (circle) and calculated (solid) external quantum efficiency with pentacene exciton diffusion length of 20, 40, 60, 70, 80, and 100nm (from bottom to top). **(b)** Calculated absorption by both active layers (solid), absorption by pentacene layers (dashed), and absorption by C_{60} layers (dotted). **(c)** Internal quantum efficiencies (IQE), defined by the ratio of EQEs and absorption. Note that the IQE of pentacene is roughly double that of C_{60}. This may reflect the presence of singlet exciton fission, although differences in exciton diffusion lengths in the two materials may also be influential. Courtesy of Yoo *et al.*[36]

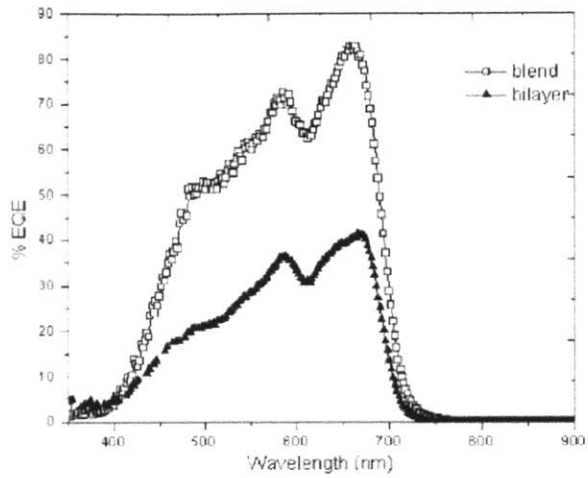

Figure 5-3. External quantum efficiency spectra for blend (open squares) and bilayer (filled triangles) devices. The active layers were 100-nm-thick pentacene:PTCDI-$C_{13}H_{27}$ (3:1) blend and pentacene (45nm)/PTCDI-$C_{13}H_{27}$ (45nm) layers for blend and bilayer devices, respectively. Courtesy of Pandey *et al.*[55]

5.3 Experimental Technique

5.3.1 Density Functional Theory Calculations

All plots in Figure 5-1 show the difference in the excited state density and the ground state density. The purple (orange) regions are where less (more) electron density is found in the excited state. In order to model the delocalization of the singlet state in a pentacene crystal, the two molecules in the unit cell is surrounded by their nearest neighbors, giving a total of ten pentacene molecules for the quantum region. The triplet-triplet state and the delocalized singlet state are calculated using the PBE0 functional and 3-21G basis set for the ten pentacene system. A ΔSCF calculation[57] is performed to acquire the delocalized singlet state and its density. The triplet-triplet state is obtained by a normal DFT

calculation with a total of 4 more alpha electrons than beta electrons. The face to face type geometry is used for the charge transfer state between pentacene and C_{60}, with a separation distance of 3 Å. The charge transfer state is calculated using constrained DFT[58], with an extra electron on C_{60} and one less electron on pentacene.

5.3.2 Device Fabrication

Pentacene, PTCBI, and C_{60} were purchased from Luminescence Technology Corporation and further purified twice by vacuum sublimation. BCP, P3HT (Regio-regular trace metal basis 99.995% purity, MW 54,000-75,000), and anhydrous chlorobenzene were purchased from Sigma-Aldrich and used as received. PEDOT:PSS (Clevios PVP AI 4083) was used as received.

Organic photovoltaic structures were fabricated on pre-patterned indium tin oxide (150 nm) purchased from Luminescence Technology Corp. with a resistance of 15 Ohm per square. The substrates were cleaned in order of Micro90 detergent solution, deionized water, acetone, boiling isopropanol and then subject to 5 minutes of oxygen plasma cleaning. PEDOT:PSS was filtered by a 0.45 μm PVDF filter and spun on the pre-cleaned substrates in air at 4000 rpm for 60 seconds. The substrates were baked in a nitrogen glovebox (base level with less than 1 ppm O_2 and H_2O) for 20 minutes at 135 °C. In the glovebox, P3HT was dissolved in chlorobenzene at a concentration of 4 mg/mL and heated and stirred at 60 °C for 30 minutes. Once fully dissolved, the P3HT was filtered with a 0.2 μm PTFE filter and spun at 2000 rpm for 60 seconds onto the PEDOT:PSS coated substrates. Substrates were then baked at 110 °C for 20 minutes to remove any residual solvent.

Deposition of the anti-reflection (AR) coating began with the previously stated cleaning procedure followed by a deposition of 120 nm MgF_2 on the front surface of the substrate. The substrate was subsequently cleaned using the previously stated cleaning procedure but starting with acetone sonication as water might damage the MgF_2 coating. Further processing continued as usual.

All other layers were thermally evaporated at pressures less than $3x10^{-6}$ Torr at ~1 Å/s. The thermal evaporator was directly attached to the glovebox. The metal cathode was defined by a 1.44 mm diameter shadow mask. Devices were packaged in a dry nitrogen environment using UV curing epoxy and glass substrates sized to cover all the active area. Thin film thicknesses were determined in-situ through use of quartz crystal oscillators. The tooling factor, the ratio between the nominal thickness and the actual thickness of thin films, was determined for each material before any device fabrication, and confirmed again at the conclusion using a Veeco optical interferometer using the monochromatic PSI mode (accurate 1–35 nm step heights). Rotation of the substrate holder during thermal evaporation resulted in a thickness variation of ±10% across the width of the substrate holder.

5.3.3 Device Characterization

External quantum efficiency measurements were performed using a 150 W Xenon lamp coupled to a Newport monochromator with the output light mechanically chopped at a frequency greater than 200 Hz. The photocurrent was measured with a lock-in amplifier under low light intensities (< 100 $\mu W/cm^2$). A Newport 818-UV silicon photodetector calibrated by Newport and reported accurate to within 1% was used to determine the

incident light intensity. This detector was also checked against a second Newport calibrated photodetector. A Keithley 2400 SourceMeter applied a reverse bias to the organic photodetectors reported in Figure 5-12.

In light-trapping geometries, devices were illuminated with a NKTPhotonics Supercontinuum laser. The photocurrent was collected with a lock-in amplifier while the laser was chopped. The device was then turned to 10° or 45°, and a mirror was placed such that the light reflected from the device was returned to it. Photocurrent measurements were taken for both s and p polarizations at each wavelength and then averaged to obtain the efficiency under incoherent illuminations.

Light-trapping experiments were designed to simulate pinhole and sawtooth solar cell configurations; however, they likely underestimate the realistic EQE when simulating the pinhole geometry, as the experiments with light incident at 10° simulate a single extra bounce, while a true pinhole structure provides multiple extra bounces.

We tested three different EQE illumination schemes using the lamp and monochromator system: illumination smaller than the device, illumination of the full device, and illumination of a thin strip of light that ran the full height of the device. For the latter two cases, the silicon photodetector was shielded by the shadow mask used for defining cathodes; in the first case it was not. A systematic error of an extra 2% photocurrent was observed when the illumination covered the full device, possibly due to incidental illumination of the device bus-bars; therefore, this configuration was not used in the measurements. Similar techniques were used to characterize the tunable laser used in the light-trapping geometries. By cross checking laser measurements at normal incidence to measurements performed using the lamp and monochromator, the collimated

beam of the laser was found to cause a 2% underestimate in the EQE at $\lambda = 670$ nm due to slight spreading of the initial laser spot outside the device boundaries. With the systematic errors corrected, we determine an overall error of 1%, largely due to the photodetector responsivity. The lamp intensity and lock-in amplifier output were both found to have the errors well below 1%.

P3HT is a key component of solar cells built with thin pentacene films. When the P3HT film is absent, the open circuit voltage drops to 0.24 V and the EQE is 24% at the peak pentacene absorption wavelength $\lambda = 670$ nm; see Figure 5-4. The P3HT likely acts to block triplet diffusion to the anode. Judging from changes in the open circuit voltage and the current-voltage characteristic in reverse bias, it appears to suppress recombination

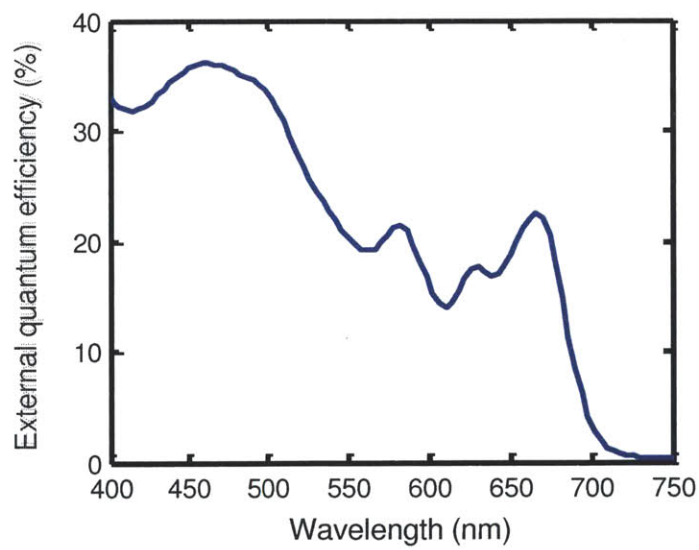

Figure 5-4 External quantum efficiency of a pentacene-C_{60} device without the exciton confinement of the P3HT layer. The device structure was ITO/pentacene 15 nm/C_{60} 35 nm/BCP 15 nm/silver.

and improve hole extraction. As shown in the atomic force micrographs of Figure 5-5, the P3HT underlayer appears to slightly lower the surface roughness of the pentacene film, but its effect, if any, on molecular orientation will need further characterization.

Charge extraction across exciton confinement layers was found to be sensitive to the hole transport level, which should lie above the 4.9 eV HOMO level of pentacene. We tested several materials that have HOMO levels of ~4.9 eV, including hole injection materials developed for OLEDs (m-MTDATA, MeO-TPD, spiro-TPD, but also α-6T); however, only P3HT did not hinder charge extraction.

Current–voltage characteristics were measured using a Keithley 2602 SourceMeter. The light current-voltage traces were obtained under illumination of a 150 W Xe arc lamp that is spectrally corrected to AM1.5G light and attenuated to 100 mW/cm^2. The active area of the device was measured using an optical microscope and the bus-bar was shadowed during the measurement.

The optical constants n and k were determined from measured reflection (R) and

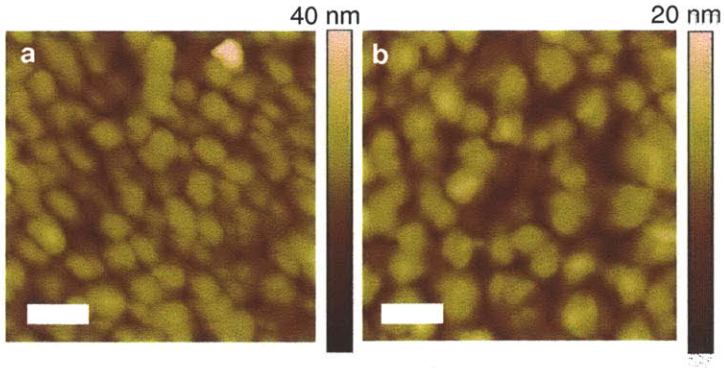

Figure 5-5 Atomic force microscopy images of 15-nm-thick pentacene films on **(a)** ITO and **(b)** ITO/PEDOT:PSS/P3HT. The scale bar is 200 nm long. The surface roughness was 3.7 nm rms and 2.4 nm rms for **a** and **b**, respectively.

transmission (T) of films deposited on a quartz substrate. As pointed out by Nitsche and Fritz[59] a simple calculation of k (from the absorption coefficient) and a Kramers-Kronig transform of k to obtain n are inaccurate when the frequency range over which k is measured is not infinite. Following their technique, we initially generated n by performing a Kramers-Kronig transform of k and refined both n and k iteratively until the simulated R and T curves had the least variance from the experimentally measured R and T. The n and k determined by this method are plotted in Figure 5-6 for each of the active materials.

Using the optical constants and the transfer matrix method[9, 59], we calculated the absorption of the active layers for the given cavity structure. To determine each material's IQE, we varied the IQE of a given material until the IQEs multiplied by the

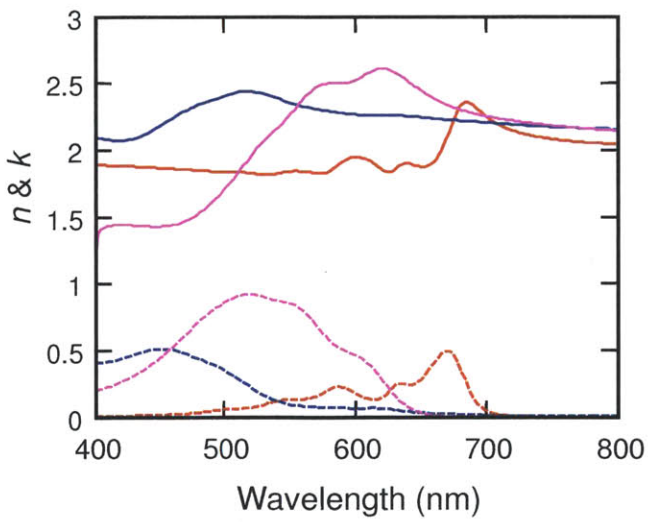

Figure 5-6 The real (—) and imaginary (– –) components of the index of refraction for pentacene (—), P3HT (—), and C_{60} (—) determined from layers deposited on quartz substrates.

absorption summed across all materials most accurately fit the measured EQE.

5.3.4 Change in Photocurrent under Applied Magnetic Field

Measurements of the change in photocurrent with application of magnetic field were performed using a 1000 W Xe arc lamp (OBB) coupled to an OBB monochromator or with monochromatic light emitting diodes. Results using either system were identical. Light incident on the devices was mechanically chopped. While the device was under illumination, an electromagnet was energized at a frequency of 13 mHz with a duty cycle of 50%. The device current (measured by a lock-in amplifier) and the magnetic field (measured by a FWBell 5100 gaussmeter) were queried at a frequency of 1 Hz. Calculations of the change in photocurrent occurred in the following steps: i) averaging the photocurrent when the applied magnetic field is at its maximum, ii) averaging the photocurrent when the applied magnetic field is zero, and iii) taking the difference between the two values and dividing by the current when the field is zero. Low incident light intensities (< 1 mW/cm^2) were used to prevent device degradation during the experiment.

The change in photocurrent with applied magnetic field traces the inverse of the change in the prompt fluorescence intensity or the change in the delayed fluorescence intensity as a function of magnetic field for tetracene[60]; see Figure 5-7. The shape of the photocurrent modulation versus magnetic field is a fingerprint for singlet fission as the photocurrent rises under a small magnetic field (B < 0.1 T) and decreases at a high magnetic field (B > 0.2 T). The singlet fission lineshape is distinct from other magnetic field dependent processes that occur in organic photovoltaic cells, such as triplet-charge

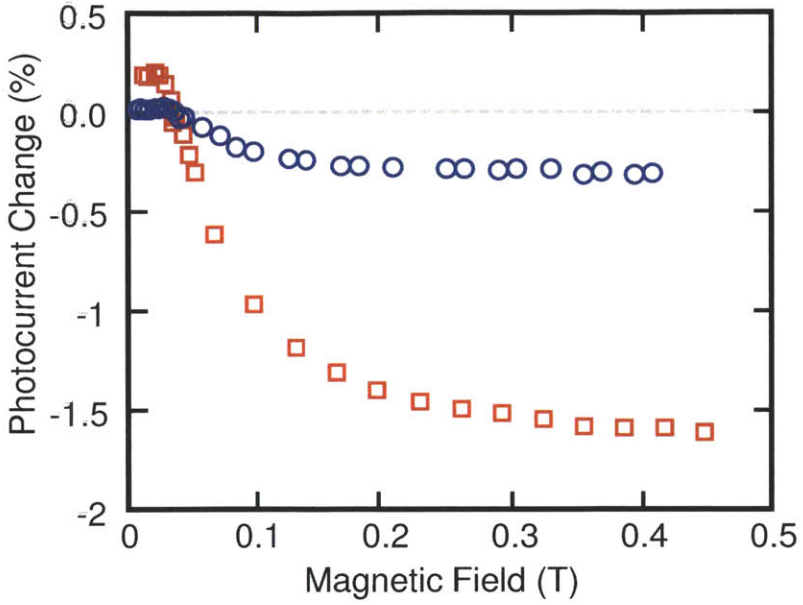

Figure 5-7 Change in photocurrent as a function of external magnetic field for a photodetector (□) and a solar cell (○). The photodetector curve was taken at a reverse bias of −4 V. Both curves first increase and then decrease before saturating at magnetic fields greater than 0.4 T. The same behavior is observed for delayed fluorescence in tetracene [60]. The large difference in the change in photocurrent observed at $B = 0.4$ T is due to the increased dissociation of the singlet into charge in the photodetector structure.

annihilation. All photodetector devices were reverse biased until the change in photocurrent was only attributed to singlet fission. The change in photocurrent reported in Figure 5-12 was measured at this reverse bias for an applied magnetic field of 0.4 T, where the photocurrent modulation is saturated with respect to the magnetic field.

We also studied the magnetic field dependence of P3HT within the device structure shown in Figure 5-9 to confirm that excitons generated in P3HT can be transferred to pentacene and subsequently split into two triplets, resulting in P3HT IQEs

above 100%. The wavelength dependence of the magnetic field effect is shown in Figure 5-8 and observed to be correlated with the optical absorption of pentacene and P3HT. Devices fabricated with only P3HT and C_{60} active layers, illuminated at $\lambda = 530$ nm, had no magnetic field dependence, demonstrating that there is no singlet fission in the absence of pentacene. This is consistent with prior studies that found no singlet fission in regio-regular P3HT, but suggested that singlet fission can occur in regio-random P3HT only under illumination of high energy photons[61]. Excitation of the acceptor in any device structure resulted in no magnetic field modulation of photocurrent.

We used the following kinetic scheme, which includes the rates essential to

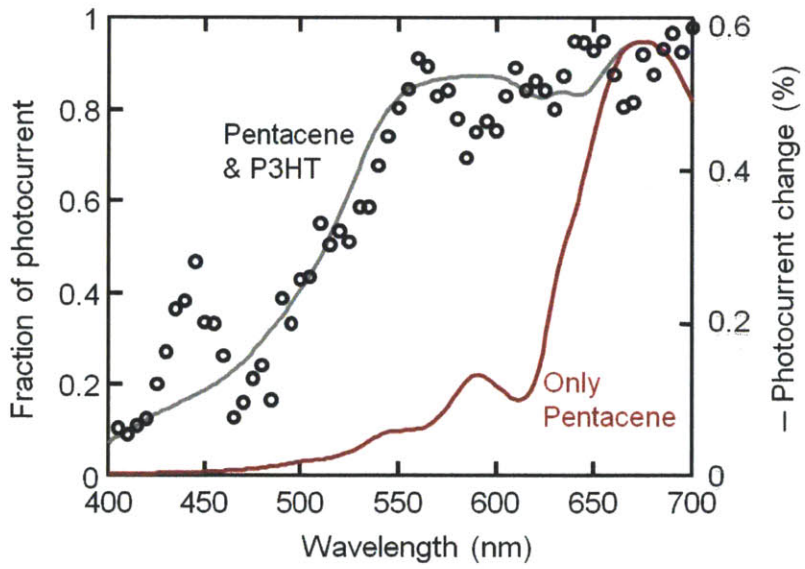

Figure 5-8 The absolute value of the change in photocurrent as a function of wavelength (○) for a solar cell with a 5-nm-thick pentacene film, so chosen to enhance the magnetic field effect. The shape is very similar to the fraction of photocurrent due to P3HT and pentacene (—) and distinct from the photocurrent contribution only from pentacene (—). The similarity is a secondary proof that P3HT is sensitized by pentacene.

Merrifield's theory of singlet fission, to explain the magnetic field dependence of photocurrent.

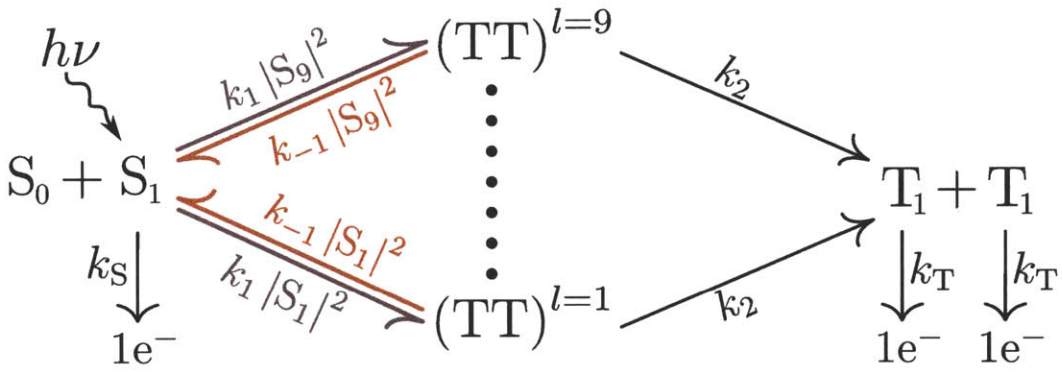

Scheme S1. Detailed kinetic scheme of singlet fission. k_1 is the conversion of a singlet exciton into a triplet-triplet pair. k_{-1} represents the reverse process, *i.e.* recombination of the triplet-triplet pair to a singlet excited state. A triplet-triplet pair is separated into two free triplets (k_2), which dissociate to charge (k_T). k_S is defined in the main text.

In Merrifield's theory, a singlet fission event takes place by way of one of nine spin-coupled triplets $(TT)^l$, where $l = 1,\ldots,9$ designates the quantum spin state. The factor $|S_l|^2$ is the singlet character of the spin state of $(TT)^l$ and changes under a magnetic field. We do not include backward recombination of the free triplets, *i.e.* $T_1+T_1 \rightarrow (TT)^l$, because such a process is endothermic by ~0.1eV; there are no reports of delayed fluorescence in pentacene.

Under steady-state conditions, the concentrations of all species are constant, leading to the following equations:

$$\frac{d[\mathrm{S_1}]}{dt} = \phi + \sum_{l=1}^{9} k_{-1}|S_l|^2\left[(\mathrm{TT})^l\right] - \sum_{l=1}^{9} k_1|S_l|^2[\mathrm{S_1}] - k_S[\mathrm{S_1}] = 0 \tag{5.1}$$

$$\frac{d\left[(\mathrm{TT})^l\right]}{dt} = k_1|S_l|^2[\mathrm{S_1}] - k_{-1}|S_l|^2\left[(\mathrm{TT})^l\right] - k_2\left[(\mathrm{TT})^l\right] = 0 \tag{5.2}$$

$$\frac{d[\mathrm{T_1}]}{dt} = 2\sum_{l=1}^{9} k_2\left[(\mathrm{TT})^l\right] - k_T[\mathrm{T_1}] = 0 \tag{5.3}$$

$$\frac{d\left[\mathrm{e}^-\right]}{dt} = k_S[\mathrm{S_1}] + k_T[\mathrm{T_1}] - k_{out}\left[\mathrm{e}^-\right] = 0 \tag{5.4}$$

where ϕ is the rate of singlet generation, and k_{out} is the rate constant for charge extraction. Solving Eq. (5.2) for $[(\mathrm{TT})^l]$, substituting into Eqs. (5.1) and (5.3), and simplifying gives

$$\begin{aligned}\frac{d[\mathrm{S_1}]}{dt} &= \phi + \sum_{l=1}^{9} k_{-1}|S_l|^2 \frac{k_1|S_l|^2}{k_{-1}|S_l|^2 + k_2}[\mathrm{S_1}] - \sum_{l=1}^{9} k_1|S_l|^2[\mathrm{S_1}] - k_S[\mathrm{S_1}] \\ &= \phi - k_1\sum_{l=1}^{9} \frac{|S_l|^2}{\frac{k_{-1}}{k_2}|S_l|^2 + 1}[\mathrm{S_1}] - k_S[\mathrm{S_1}] \\ &= \phi - k_{fis}(B)[\mathrm{S_1}] - k_S[\mathrm{S_1}] = 0\end{aligned} \tag{5.5}$$

and

$$\begin{aligned}\frac{d[\mathrm{T_1}]}{dt} &= 2\sum_{l=1}^{9} k_2\left[(\mathrm{TT})^l\right] - k_T[\mathrm{T_1}] \\ &= 2k_1\sum_{l=1}^{9} \frac{|S_l|^2}{\frac{k_{-1}}{k_2}|S_l|^2 + 1}[\mathrm{S_1}] - k_T[\mathrm{T_1}] \\ &= 2k_{fis}(B)[\mathrm{S_1}] - k_T[\mathrm{T_1}] = 0\end{aligned} \tag{5.6}$$

where we have defined an overall rate constant $k_{fis}(B)$ for the process of going from S_1 to $2T_1$ (i.e. singlet fission):

$$k_{fis}(B) = k_1 \sum_{l=1}^{9} \frac{|S_l|^2}{\frac{k_{-1}}{k_2}|S_l|^2 + 1} \tag{5.7}$$

Note that the expression for $k_{fis}(B)$ in Eqs. (5.5)–(5.7) is identical to the one in Merrifield's theory[62]. Our kinetic scheme can thus be simplified to Scheme S2:

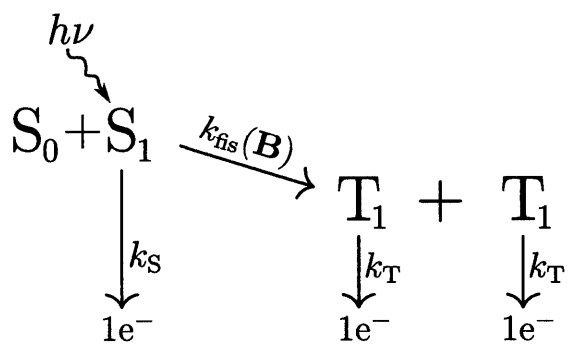

Scheme S2. Simplified kinetic scheme of singlet fission. k_S and k_T are defined in the main text and Scheme S1.

Combining Eqs. (5.4) through (5.6) gives an expression relating the photocurrent $I(B)$ to the rate constants:

$$I(B) \propto \frac{k_{out}}{\phi}\left[e^-\right] = \frac{k_S}{k_{fis}(B) + k_S} + 2\frac{k_{fis}(B)}{k_{fis}(B) + k_S} \tag{5.8}$$

For convenience, we write $k_{fis}(B) = \chi(B)k_{fis}^0$, where $\chi(B)$ is the modulation of the zero-field fission rate k_{fis}^0 due to an external magnetic field. The normalized change in photocurrent is thus given by

$$\delta = \frac{I(B) - I(0)}{I(0)} = \frac{k_S k_{fis}^0(\chi - 1)}{\left(2k_{fis}^0 + k_S\right)\left(\chi k_{fis}^0 + k_S\right)} \tag{5.9}$$

which is Eq. (5.10).

Finally, we note that while Merrifield's theory allows one to calculate $\chi(B) = k_{fis}(B)/k_{fis}^{0}$ from first principles, it requires knowledge of the zero-field-splitting parameters D and E in the Hamiltonian for pentacene triplet excitons and also the ratio k_{-1}/k_2. These were fitting parameters in Merrifield's work. As shown in the main text, we were instead able to obtain an expression for $\chi(B = 0.4\ \mathrm{T})$ requiring only the experimental values of δ_{max} at $B = 0.4$ T (see Eq. (5.11)). This leads to an expression that gives the fission yield of a device simply by measuring its δ at $B = 0.4$ T (see Eq. (5.12)). We do not need to calculate or fit the line shapes of the change in photocurrent versus magnetic field.

Implicit in our model is the assumption that $\chi(B)$ is invariant with pentacene layer thickness. This assumption might break down for very thin layers (< 2 nm) of pentacene, as χ represents a balance of the forward and backward rates linking the singlet exciton and the triplet-triplet pair. Direct dissociation of the triplet-triplet pair would alter the balance and increase $\chi(B)$ closer to one, resulting in a change in photocurrent trending toward zero as the pentacene layer thickness is decreased. Nevertheless, we assume that the change in $\chi(B)$ for very thin pentacene films is small because triplet dissociation into charge (~400 fs) is slower than singlet fission (80 fs) for pentacene monolayers on C_{60}[46].

5.4 Device Structure and External Quantum Efficiency

5.4.1 Device Structure

The structure of our pentacene-based solar cell is shown in Figure 5-9a. The core of the device is a pentacene/C_{60} donor-acceptor junction[33, 41, 54]. To minimize triplet exciton losses, we used a thin pentacene layer and also introduced an exciton blocking layer of regio-regular poly(3-hexylthiophene) (P3HT), which was placed between the pentacene and the anode. The combination of the wide energy gap and 1.5 eV triplet energy[67] of P3HT confines pentacene triplet excitons, and its highest occupied molecular orbital

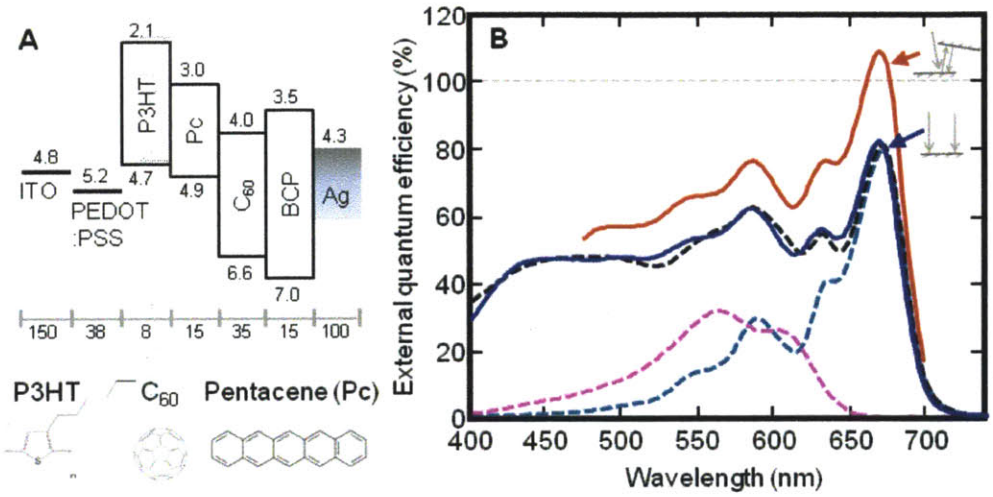

Figure 5-9 (a) Chemical structures and architecture of the solar cell with the thickness of each layer in nanometers and energy levels of the lowest unoccupied and highest occupied molecular orbitals in eV[33, 54, 63-66]. The anode is composed of indium tin oxide (ITO) and poly(3,4-ethylenedioxythiophene) poly(styrenesulfonate) (PEDOT:PSS). The cathode employs bathocuproine (BCP) and a silver cap. **(b)** External quantum efficiency of devices without optical trapping (—), and device measured with light incident at 10° from normal with an external mirror reflecting the residual pump light (—). Optical fits from IQE modeling are shown with dashed lines: modeled pentacene EQE (– –), modeled P3HT EQE(– –), and modeled device EQE (– –) for comparison to the measured device efficiency without optical trapping.

(HOMO) of 4.7 eV[63] helps extract holes from pentacene. To maximize light absorption, devices were fabricated with MgF_2 antireflection coatings on the front surface of the glass substrate.

5.4.2 Singlet Fission Sensitizer

Although the P3HT/pentacene/C_{60} device was designed to prevent quenching of pentacene excitons at the anode, it also shows singlet fission sensitization. In this section I introduce Reusswig *et al.*'s demonstration of singlet sensitization by rubrene.[68] Singlet fission molecules, including acenes, often exhibit low absorption coefficients ($< 10^5$ cm^{-1}), which limits the efficiency of singlet-fission-based solar cells. To overcome this problem, Reusswig *et al.* devised a solar cell architecture where a singlet fission sensitizer is inserted between a singlet donor and an acceptor; see Figure 5-10a for the device operation principle.[68] Excitons created by photon absorption of singlet donors migrate to a singlet fission sensitizer, where the number of excitons doubles. In this device, the process of singlet exciton fission is decoupled from photon absorption, exciton diffusion, and charge transport.[68] This architecture can convert a variety of highly light-absorbing molecules to effective singlet fission materials.[68]

Reusswig *et al.* built a tris[4-(5-phenylthiophen-2-yl)phenyl]amine (TPTPA)/PDI-CN2 planar heterojunction device with rubrene as the singlet fission sensitizer (see Figure 5-10b).[68] Figure 5-10c presents the boost in the efficiency of singlet donor photoexcitations by the singlet fission sensitizer. The EQEs at $\lambda < 450$nm, where TPTPA absorption dominates, doubles as a thin layer of rubrene is inserted.

The magnetic field effect on photocurrent confirms that the EQE enhancement owes to energy transfer from TPTPA to rubrene and consequent singlet fission in rubrene; see Figure 5-10d.[68] The singlet fission sensitizer device shows reduction in photocurrent down to −14% upon photoexcitation of TPTPA under applied magnetic fields, meaning that TPTPA absorptions undergo singlet fission. The control device shows almost no magnetic field effect.

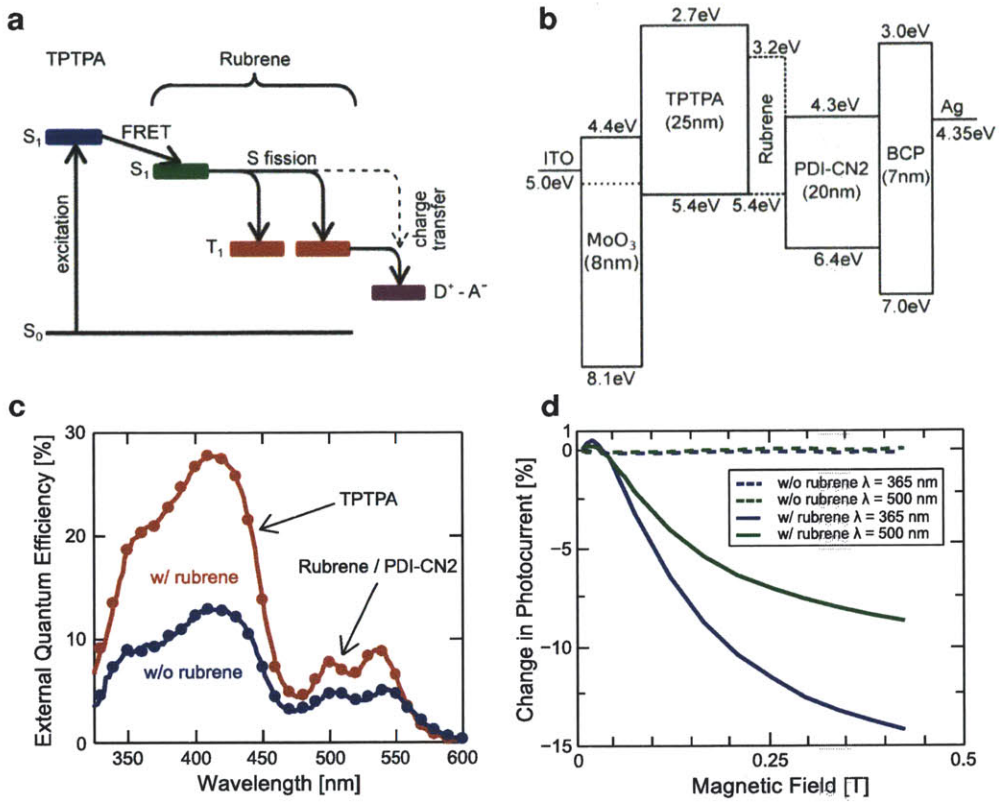

Figure 5-10. **(a)** Energy flow in photovoltaic devices that exploit a singlet exciton fission sensitizer. Optical excitation populates singlets on TPTPA. The singlet excitons are transferred to rubrene, a singlet fission sensitizer, where they undergo singlet fission, followed by charge transfer at the donor–acceptor interface. **(b)** A device structure of TPTPA/PDI-CN2 bilayer photovoltaic cells incorporating a singlet fission sensitizer. **(c)** EQE spectra of the TPTPA/rubrene/PDI-CN2 photovoltaic device compared to the control device. **(d)** Comparison of magnetic field dependence of photocurrent for TPTPA/PDI-CN2 devices without rubrene (dashed) and with rubrene (solid). The illuminations at $\lambda = 365$nm (blue) and $\lambda = 500$nm (green) photoexcite TPTPA and rubrene, respectively. Courtesy of Reusswig *et al.* [68].

5.4.3 External Quantum Efficiency

The external quantum efficiency (EQE) is defined as the ratio between the number of electrons flowing out of the device and the number of photons incident upon it. We measured the EQE (Figure 5-9B) for a device that features a 15-nm-thick pentacene layer. The EQE at normal incidence is (82±1)% at the peak pentacene absorption wavelength $\lambda = 670$ nm. Optical modeling predicts that the internal quantum efficiency (IQE), which is defined as the number of electrons collected per photon absorbed, for photoexcitation of pentacene and P3HT is (160±10)% and (150±10)%, respectively. The IQE of pentacene in this structure is approximately double that reported previously for pentacene[54, 70], and the high IQE of P3HT is consistent with the expected sensitization of P3HT by pentacene, as singlet excitons generated in P3HT are transferred to pentacene and then split into triplets[71]. The peak EQE drops to 24% when P3HT is absent. The P3HT appears to block triplet diffusion to the anode and suppress recombination by improving hole extraction; see Figure 5-4, 5-5, and 5-6 and accompanying text for further discussion of both sensitization and the efficiency enhancement due to P3HT.

The 15-nm-thick film of pentacene in the solar cell microcavity absorbs only 49% of the incident light at $\lambda = 670$ nm according to optical modeling and hence the efficiency should improve if a light-trapping scheme is employed. Therefore, we measured the EQE in configurations designed to simulate two conventional optical trapping schemes. The first scheme mounts the cell at 45° to the incident light, with a mirror that directs reflected photons back to the device. This configuration models a saw tooth geometry such that incident light bounces at least twice within the structure[72, 73]. In the second scheme, the incident angle is reduced to 10° from the normal, modeling an optical

collector that focuses light through a small hole in a mirror held parallel to the surface of the cell[9]. The peak EQE at $\lambda = 670$ nm for the solar cell mounted at 45° is (102±1)%, increasing to (109±1)% for incidence at 10° from the normal. Both light-trapping schemes yield efficiencies that meet or exceed the one electron per incident photon benchmark.

5.5 Current-voltage characteristics

The current-voltage characteristics of the planar pentacene solar cell are shown in Figure 5-11. The short circuit current measured at AM1.5 matches the integrated EQE measured at < 1 mW/cm^2 to within 6%, demonstrating that the fission process in pentacene is not significantly intensity dependent. As expected, the enhanced EQE does not correspond to a high power efficiency. The open circuit voltage is 0.36 V, identical to the values of previous pentacene devices[54]. It is defined by the pentacene triplet energy of 0.86 eV[40, 49]. With C_{60} as the acceptor, the device absorbs light only above the pentacene singlet energy at 1.8 eV. Consequently, the power efficiency is (1.8±0.1)%.

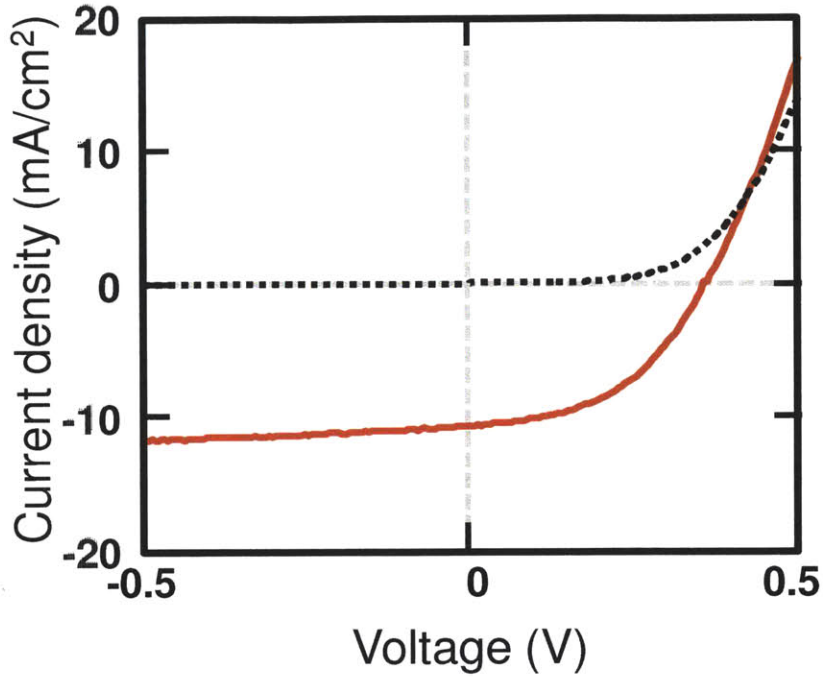

Figure 5-11 The current-voltage characteristic of the pentacene solar cell measured under dark (– –) or AM1.5 (—) conditions without optical trapping. The power efficiency is (1.8±0.1)%.

5.6 Determination of Singlet Fission Efficiency Using Magnetic Field Effect

Independent confirmation of the high internal quantum efficiency within the cell is provided by analysis of the photocurrent under a magnetic field. The crucial rates are identified in Figure 5-1. The singlet exciton can either directly dissociate into a single electron-hole pair, k_S, or undergo fission resulting in generation of two electron-hole pairs, $k_{fis}(B)$. In absence of a magnetic field, three out of nine triplet-pair states have

singlet character. Under a high magnetic field ($B > 0.2$ T), the number of triplet-triplet pairs with singlet character reduces to two, reducing the singlet fission rate, $k_{fis}(B)$. The photocurrent yield changes if there is effective competition between fission and the dissociation of the singlet exciton. Note that it is not possible to generate a magnetic field effect on the photocurrent yield unless there is a singlet loss mechanism that competes with the fission process.

For convenience, we write $k_{fis}(B) = \chi(B) k_{fis}^0$, where $\chi(B)$ is the modulation of the zero-field fission rate k_{fis}^0. The normalized change in photocurrent in steady state, δ, is then given by

$$\delta = \frac{I(B) - I(0)}{I(0)} = \frac{k_S k_{fis}^0 (\chi - 1)}{(2k_{fis}^0 + k_S)(\chi k_{fis}^0 + k_S)}, \tag{5.10}$$

where $I(B)$ is the photocurrent as a function of magnetic field strength. Dissociation of the singlet exciton directly into charge is only likely to compete with fission for pentacene molecules directly adjacent to the acceptor. Indeed, reductions in the singlet exciton lifetime of pentacene have been observed in very thin pentacene films (0.6 monolayer) adjacent to a C_{60} layer[46]. Thus, we can approximately model pentacene films of varying thickness by changing the effective rate of singlet dissociation in Eq. (5.10).

Analytically, we can solve for χ at a given value of the magnetic field by noting that the magnitude of δ is maximized when $k_S = k_{fis}^0 \sqrt{2\chi}$. This yields

$$\chi = \frac{2\delta_{max}^{\ 2} + \delta_{max} + 1 + 2\sqrt{2}\delta_{max}\sqrt{\delta_{max} + 1}}{(\delta_{max} - 1)^2}. \tag{5.11}$$

The result for χ can be used to directly obtain the triplet yield of singlet fission from the magnetic field modulation in photocurrent:

$$\eta_{fis} = \frac{2}{1+k_S/k_{fis}^0} = \frac{(1-\delta)\chi - 1 \pm \sqrt{(\delta(\chi+2)-\chi+1)^2 - 8\delta^2\chi}}{(\delta+1)(\chi-1)}. \qquad (5.12)$$

To obtain an independent measure of the yield of singlet fission, we fabricated multiple devices while varying the thickness of pentacene, see Figure 5-12. For thin layers of pentacene (d < 5 nm) we increased the optical absorption by employing the multilayer photodetector architecture[9, 41]. Photodetectors were measured in reverse bias to improve charge extraction. As a test of generality, both C_{60} and 3,4,9,10-perylene tetracarboxylic bisbenzimidazole (PTCBI) were used as acceptor molecules and found to yield similar results. Devices with thicker layers of pentacene employed the same device architecture as Figure 5-9. The magnetic field modulation of photocurrent at 0.4 T is shown in Figure 5-12A. It peaks at $\delta_{max} = -(2.7\pm0.1)\%$ in 2-nm-thick layers of pentacene sandwiched between acceptor layers. From Eq. (5.11), we obtain $\chi = 0.85$, identical to the value assumed in Ref. 41 based on tetracene measurements[74].

In Figure 5-12b we apply Eq. (5.12) to transform the magnetic field modulation data into the expected yield of triplet excitons from singlet fission. We find that singlet fission is incomplete in pentacene films with thickness d < 5 nm, accounting for the relatively low IQE in the photodetector structures. The triplet yield approaches 200% in thicker films, providing independent confirmation of the high IQE calculated for the device structure shown in Figure 5-9.

The IQE, as evaluated using optical modeling[9], is shown in Figure 5-12c and compared to predictions based on the magnetic field effect. The IQE is suppressed in thin

layers of pentacene, increases to a maximum for $d \sim 15$ nm, and then is reduced in thicker films. Decreases in IQE for thicker films are presumably due to triplet exciton diffusion limitations and lower than unity charge collection efficiency. There are two important conclusions from this IQE comparison. First, the yield of singlet fission can be conveniently determined directly from the normalized change in photocurrent under a magnetic field. A high yield is characterized by a vanishing modulation of photocurrent under magnetic field. Second, singlet fission in pentacene requires a relatively thick film to minimize losses due to singlet exciton dissociation. Fission is not effective in fine-grained blends of pentacene and fullerene or perylene-based acceptors.

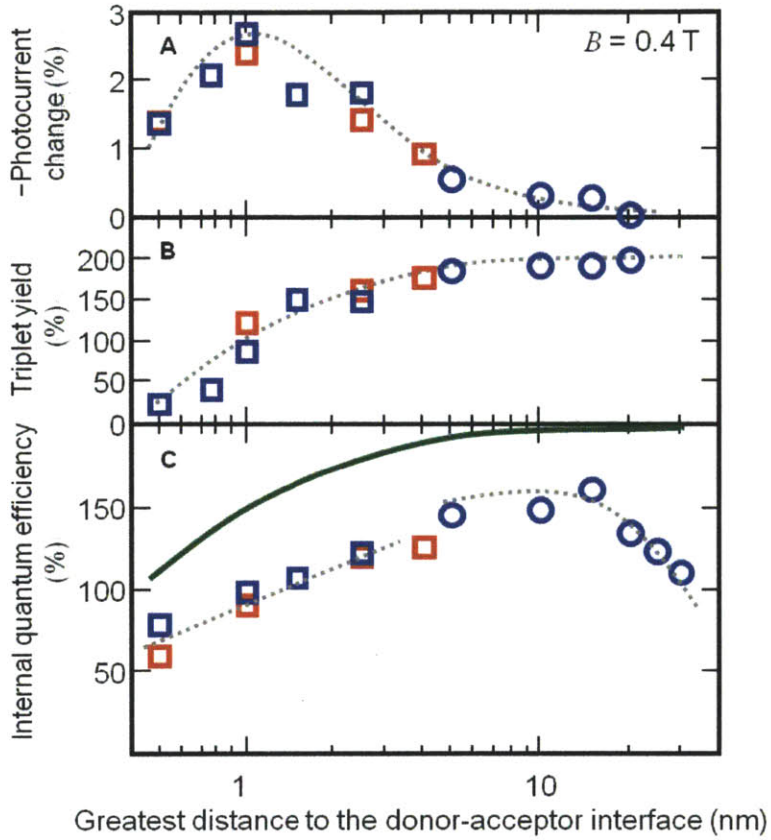

Figure 5-12 (A) The magnetic field dependent change in photocurrent measured at $B = 0.4$ T as a function of pentacene layer thickness. Square symbols are measured in photodetector structures and each pentacene layer is sandwiched between C_{60} (□) or PTCBI (□) acceptor films. Measurements in the solar cell architecture of Figure 5-9A are circles (○). **(B)** The triplet yield from singlet exciton fission as obtained from Eq. (5.12). **(C)** A comparison of the maximum achievable quantum yield determined from the magnetic field effect (—) with the internal quantum efficiency as determined from EQE measurements and the calculated optical absorption. The reduction in quantum efficiency observed in thin layers of pentacene is found to originate in incomplete singlet exciton fission. Grey dashed lines are a guide to the eye.

5.7 Conclusion

The observation of external quantum yields exceeding 100% in the visible spectrum represents a significant advance in the application of singlet fission to solar cells. Next, fission should be paired with a low bandgap material that harvests photons below the singlet exciton energy. This could be an organic material[47], inorganic semiconductor nanocrystal[33, 48, 49], or a conventional inorganic semiconductor [50]. High quality contemporary silicon solar cells show an AM1.5 efficiency of approximately 25%[75]; singlet fission materials such as tetracene or rubrene could be integrated with silicon cells to double the photocurrent from high-energy solar photons ($\lambda < 550$ nm), ultimately boosting the efficiency of the silicon cell to over 30%.

6. Universal Mechanism for Singlet Exciton Fission

Exciton fission is a process whereby one singlet exciton splits into two independent triplets. It has the potential to increase the power conversion efficiency of single junction solar cells above 40% by doubling the current from high energy photons. Here, we measure fission dynamics using ultrafast photoinduced absorption and derive a first principles expression that successfully predicts the rate of fission for a range of materials with vastly different intermolecular structures, spanning more than three orders of magnitude in fission rates. Our results show that the experimental rates are consistent with a nonadiabatic Marcus-like mechanism in weakly interacting systems and an adiabatic, coupling independent pathway at larger interaction strengths. Unlike alternative multiple exciton generation and inverse Auger processes, singlet exciton fission is found to be robust against both variations in nanostructure and thermalization losses, yielding unity efficiency across the wide range of materials studied. The success of the kinetic model developed here paves the way for the rational design of singlet fission photovoltaic materials.

6.1 Introduction

Singlet exciton fission was first observed in crystalline acene materials in the 1960s[69]. In a simple dimer picture, labeling the monomer electronic states as S_0, S_1 and T,

$$S_0S_0 \xrightarrow{h} S_1S_0 \xrightarrow{k_{fis}} TT$$

Because fission generates two independent triplet excitons from a single high energy photon, fission-based solar cells can produce quantum yields in excess of 100%[41] and in principle could lead to single junction photovoltaics with power efficiencies above 40%[13].

Singlet fission has only been observed in a handful of materials – primarily several acenes[32, 37, 41, 69, 76], an isobenzofuran[77] and some carotenoids[78]. The rational design of new materials for singlet fission-based devices has been limited because the mechanism of singlet fission is not well understood. Numerous time-resolved studies have confirmed that fission can occur very quickly – on timescales as short as 80 fs[32, 37, 38]. However, it is not clear *why* it is so fast or what material properties must be controlled to ensure efficient fission. In this article, we resolve this mystery by presenting a theoretical model that correctly predicts measured fission rates across three orders of magnitude in k_{fis}.

From a physical perspective, the dominant pathway for fission will be determined by the sizes of two different parameters: the coupling, $V = \langle S_1S_0 | \hat{H} | TT \rangle$, between the singlet excited state and the triplet pair state and the energy difference, $\Delta E_{CT} = E_{S_1} - E_{CT}$, between the singlet and charge transfer excited states. We can then identify four possible mechanisms, each with its own rate expression (See Figure 6-1): 1) Activated charge

transfer when ΔE_{CT} is very small[79] and V is negligible 2) Superexchange (or CT mediated fission[13]) when ΔE_{CT} is on the order of the electron hopping integral, t,[80, 81] 3) Direct fission when V is moderately large[82] and 4) Coherent fission when V is of the same order of magnitude as the energy difference between S_1S_0 and TT[83].

6.2 Selection of Materials

In order to quantify which of these models is correct, we study thin films of the six different pentacene derivatives shown in Figure 6-2: pentacene, 6,13-bis(triisopropyl-silylethynyl) pentacene (TIPS-P), 6,13-diphenylpentacene (DPP), 6,13-di-biphenyl-4-yl-pentacene (DBP), 6,13-di(2'-thienyl)pentacene (DTP), and 6,13-di-benzothiophene-pentacene (DBTP). The crystal structures were either obtained from literature[84-86] or determined from X-ray crystallography. As is clear from the Figure, while chemically

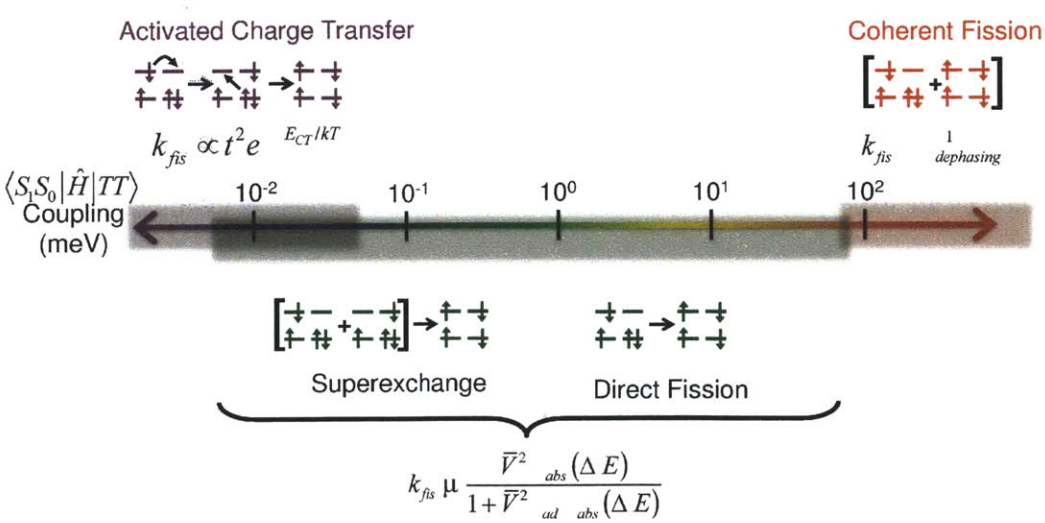

Figure 6-1 Four possible mechanisms for singlet fission: 1) Activated charge transfer, 2) Superexchange, 3) Direct singlet fission, and 4) Coherent fission.

	Pentacene	TIPS-P	DTP	DBTP	DBP	DPP
Crystal Structure	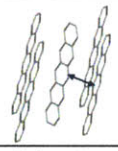	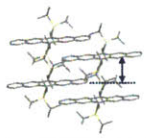	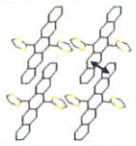	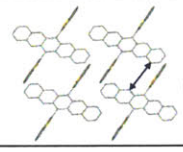	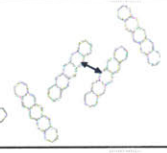	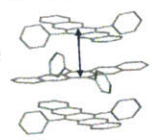
Structure Name	Edge-to-face, herringbone	2D π stack	Cofacial slip stack	Side slip stack	Side slip stack	Orthogonal
Distance (Å)	3.5	3.3	3.6	5.0	5.5	5.0
Coupling (meV)	63.6	119.0	17.6	5.80	1.75	0.791
Time Constant (ps)	0.090	0.10	0.16	0.90	3.8	11.8

Figure 6-2 Pentacene derivatives examined in this study and their crystal structures, structure characteristics, intermolecular distances, coupling ($V = \langle S_1 S_0 | \hat{H} | TT \rangle$), and time constants for singlet fission.

similar, these compounds adopt radically different crystal structures from one another. Pentacene packs in a herringbone arrangement, TIPS-P creates a 2D π-stacked structure, DTP shows cofiacial 1D stacking, while in DBP, DPP, and DBTP the sidechains prevent significant π overlap between the pentacene cores. The structural variations in these materials are expected to have a dramatic impact on the electronic coupling (V) between monomers, leading to significant variation of k_{fis}.

6.3 Theoretical Determination of Coupling

For each material, we compute the coupling V using constrained density functional theory (CDFT)[87, 88]. We model the electronic states of a dimer embedded in the crystal electrostatic field[89]. For each dimer, we obtain localized, diabatic states by constraining

the charge and spin of each monomer (M) to match the appropriate physical state: S_1S_0, S_0S_1, M^+M^-, M^-M^+, TT. Using these states to compute V directly[90], we obtain couplings spanning a range of almost three orders of magnitude for the materials in Figure 6-2. This prescription has been shown previously to quantitatively predict triplet hopping rates in acenes[91]. Because triplet hopping relies on a coupling ($V_{TT} = \langle T_1S_0 | \hat{H} | S_0T_1 \rangle$) that is physically similar to the fission coupling, one thus expects that these theoretical estimates should be reliable. For pentacene, our calculations are in semi-quantitative agreement with existing theoretical estimates of V [92].

In agreement with electroabsorption data, CDFT predicts the energy gaps ΔE_{CT} are fairly small (0.3–1.0 eV). Thus, superexchange might play a significant role in fission[80, 81]. Indeed, the absorption spectra (see Figure 6-3) for pentacene, TIPS-P and DTP show the clear signature of CT mixing in the bright excited state[93]. We can account for superexchange and direct fission simultaneously by mixing the four states (S_1S_0, S_0S_1, M^+M^-, M^-M^+) to obtain four quasi-adiabatic states that account for superexchange-type CT mixing. Then, selecting the bright state from among these four, we compute the modified coupling $\overline{V} = \langle Bright | \hat{H} | TT \rangle$, shown in Figure 6-2. In agreement with the experimental spectra, we find that superechange only appreciably changes the coupling for materials (Pentacene, TIPS-P and DTP) where CT mixing is significant in the bright state.

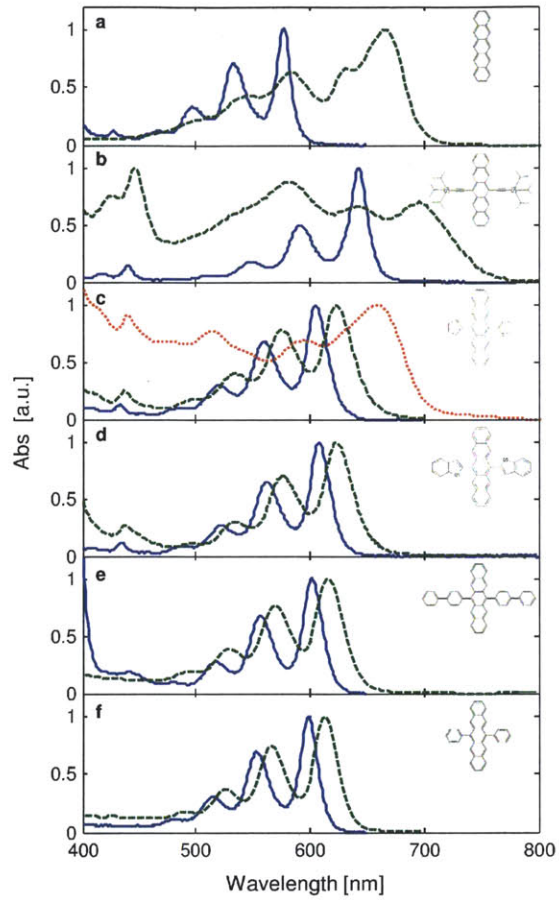

Figure 6-3 Absorbance spectra of toluene solutions (blue solid) and thin-films (green dashed) of (a) pentacene, (b) TIPS-P, (c) DTP, (d) DBTP, (e) DBP, and (f) DPP. The red dotted line in (c) shows the spectra of annealed DT-P thin-films.

6.4 Rate Model for Singlet Fission

To model the rate of fission, we borrow from the extensive literature on electron transfer rates as a function of electronic coupling[82, 94-96]. For weak coupling, k_{fis} is expected to follow the celebrated Marcus nonadiabatic rate expression: $k_{na} = 2\pi/\hbar(DWFC)$ $\approx \overline{V}^2 e^{-\frac{(\Delta G+\lambda)^2}{4\lambda kT}}$. DWFC is the density weighted Franck-Condon factor, which can be

approximated classically for low frequency modes[97]. k_{na} assumes activated motion in the bright diabatic state and sudden, rare transitions to the TT state, as illustrated in Figure Figure 6-4. For large coupling, this nonadiabatic picture ceases to be appropriate. Instead, the system follows the adiabatic state, which evolves continuously from S_1-like to TT-like as the reaction progresses. In the adiabatic limit, the rate is governed by the speed of nuclear rearrangement (which may or may not be activated) and thus k_{fis} will become independent of $\bar{V}$ for large enough $\bar{V}$. These two limits can be unified into a single rate expression as shown by Bixon and Jortner (BJ)[82]:

$$k_{fis} = \sum_n \frac{\bar{V}^2 k_n}{1+\tau_n^{ad}\bar{V}^2}$$
$$k_n \equiv \left(\frac{\pi}{\hbar^2 \lambda kT}\right)^{\frac{1}{2}} \left|\langle 0|n\rangle\right|^2 e^{-\frac{(\Delta G + n\hbar\omega + \lambda)^2}{4\lambda kT}} \qquad \tau_n^{ad} \equiv \frac{4\pi}{\hbar\lambda}\tau_{ad}\left|\langle 0|n\rangle\right|^2 \tag{6.1}$$

The BJ rate predicts k_{fis} will follow the nonadiabatic rate (k_n) when $\bar{V}$ is small but be

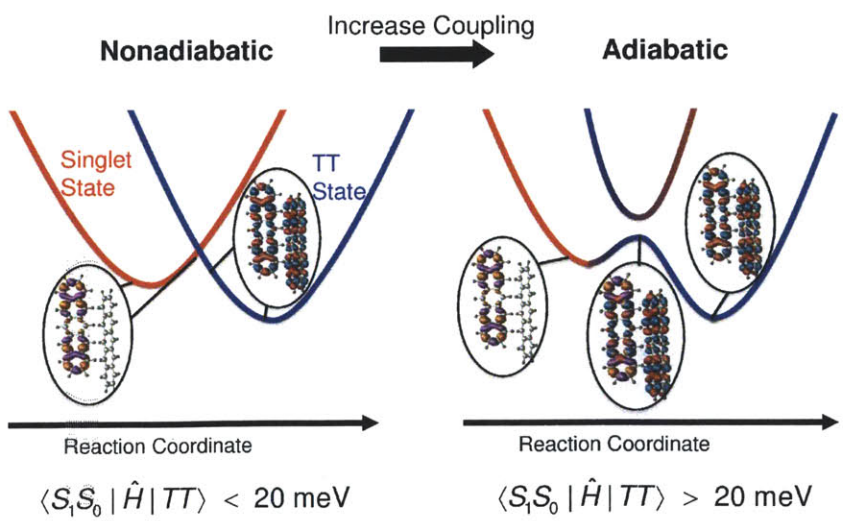

Figure 6-4 Nonadabatic versus adiabatic models for singlet fission.

limited by the adiabatic timescale (τ_{ad}) for large $\bar{V}$. This rate expression depends on several parameters – the reorganization energy (λ), the driving force (ΔG), the frequency and displacement of the primary accepting mode (ω, Δ) – all of which can be estimated based on experimental spectra and simple monomer calculations.

We fix ΔG based on the experimental estimates of the S_1-TT energy gap in pentacene: $\Delta G = -0.1$ eV. Meanwhile, we fix the frequency of the accepting mode based on the frequency of the vibrational progression in the S_1 absorption spectrum: $\omega = 1450\ \mathrm{cm}^{-1}$. Next, we estimate the displacement to be $\Delta \sim 0.75$, based on the vibrational progression in acene absorption and emission spectra. Next, we compute the overall reorganization energy using PBE0/6-31G* geometry optimizations of the S_0, S_1 and T states of each monomer in conjunction with the four point rule:

$$\lambda_{full} = \tfrac{1}{2}\,([S_1S_0|TT] + [TT|S_1S_0] - [S_1S_0|S_1S_0] - [TT|TT])$$

$$\rightarrow \lambda_{full} \sim \tfrac{1}{2}\,([S_1|T] + [S_0|T] + [T|S_1] + [T|S_0] - [S_1|S_1] - [S_0|S_0] - 2[T|T])$$

where [A|B] means "the energy of state A at the relaxed geometry of state B". The reorganization energy in the BJ formula is the total reorganization energy minus the amount accounted for by the accepting mode: $\lambda = \lambda_{full} - h\omega\Delta$. Finally, we can estimate τ_{ad} (which is basically the attempt frequency) based on the C-C stretching frequency in acenes, so $\tau_{ad} \sim 40$ fs.

Finally, in order to apply Eq. (6.1) to the materials here, we note that for a given singlet state, there will always be two equally likely final states after fission. Expanding our notation to include three monomers: $|S_0S_1S_0\rangle \rightarrow |S_0TT\rangle$ *or* $|TTS_0\rangle$. Since there are two equally likely final states, each generated with a rate according to Eq. (6.1), we

assume the observed rate (which corresponds to the total rate of triplet generation) corresponds to $2k_{fis}$. A more sophisticated treatment would involve proper treatment of the periodic boundary conditions and coupling of the manifold of delocalized excitonic states onto the manifold of final TT states. Multiplying the rate by two is a rough approximation to these effects.

6.5 Experimental Determination of Fission Rates

To test Eq. (6.1), we measure the fission rate by photoinduced absorption (PIA). The bright state is excited by a 610 nm pump and the formation of triplets is probed by monitoring the intensity of $T_1 \rightarrow T_2$ (880 nm) and $T_1 \rightarrow T_3$, (520 nm) transitions at various time delays. We obtain the rate of singlet fission by fitting the PIA signal to a single exponential in time.

Figure 6-5 presents the transient absorption (TA) spectra of various pentacenes to identify the triplet absorption region. The pump wavelength was 550–650 nm and the pulse irradiance was 30–45 μJ/cm^2. The TA spectrum of pentacene is from Ref. 37. Our TIPS-P spectrum is consistent with previously reported results.[98] The broad peak around 480 nm that appears immediately upon photoexcitations was previously attributed to the $S_1 \rightarrow S_n$ transition.[98]

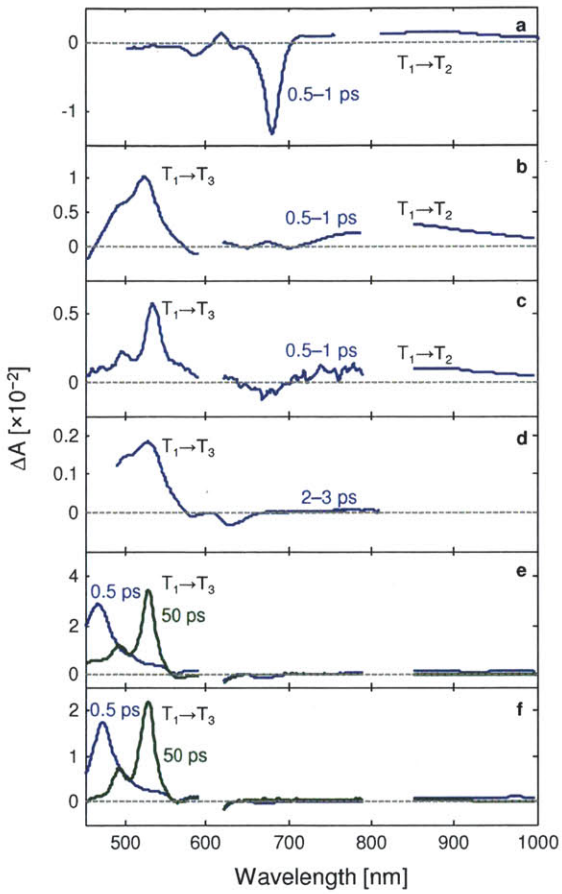

Figure 6-5 Femtosecond transient absorption spectra of **(a)** pentacene, **(b)** TIPS-P, **(c)** DTP, **(d)** DBTP, **(e)** DBP, and **(f)** DPP with various time delays.

The broad photoinduced absorption around 880 nm has been assigned as the $T_1 \rightarrow T_2$ transition from previous theoretical calculations[99] and experimental reports.[37, 52, 100] Yet this $T_1 \rightarrow T_2$ transition has not been observed for isolated pentacene molecules in solutions[101] and Pabst *et al.* estimated that the $T_1 \rightarrow T_2$ transition at 880nm would be much weaker than the $T_1 \rightarrow T_3$ transition.[99] We observe the $T_1 \rightarrow T_2$ transition only in the films with strong coupling: unsubstituted pentacene, TIPS-P and DTP, which suggests that the $T_1 \rightarrow T_2$ transition becomes strengthened from enhanced intermolecular interactions.

The photoinduced absorption around 520 nm, which appears in all the pentacene derivatives investigated here except unsubstituted pentacene, has been attributed to $T_1 \rightarrow T_3$ transition[99] and observed in pentacene dissolved in solution[101]. Rao *et al.* showed that this peak is not observable in pentacene thin films due to a minimum overlap between the polarization of the triplet-triplet absorption and the pump laser electric field.[100] Also, they demonstrated that the triplet dynamics probed at 520nm ($T_1 \rightarrow T_3$) and 880nm ($T_1 \rightarrow T_2$) are identical.[100]

Figure 6-6 presents the transients of triplet formation in a series of pentacene derivatives. The peak of the transient absorption spectra at 520 nm (880 nm) was chosen for DBTP, DBP and DPP (pentacene, TIPS-P and DTP). The pump intensity was 5–40 μJ/cm^2, and we verified the absence of singlet-singlet annihilation by confirming the independence of the transient shape on intensity dependence. We obtained the rate of

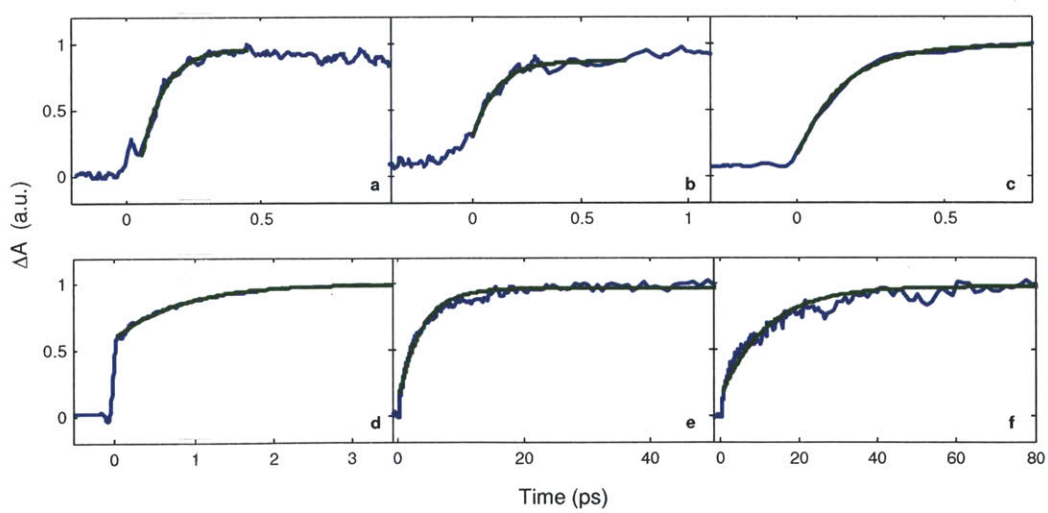

Figure 6-6 Photoinduced absorption kinetics of triplets (blue) for **(a)** pentacene, **(b)** TIPS-P, **(c)** DTP, **(d)** DBTP, **(e)** DBP and **(f)** DPP. Green lines are exponential fittings for the corresponding data.

singlet fission by fitting an exponential curve to the data. Figure 6-2 summarizes the time constant of singlet fission in various pentacenes.

6.6 Prediction of Fission Rates

Figure 6-7 compares the observed fission rates to the values of k_{fis} predicted by Eq. (6.1) for the compounds in Figure 6-2. The theoretical expression reproduces the experimental rates to within the anticipated accuracy in all cases. For compounds with $\bar{V} < V_c \approx$ 20 meV the rates increase as $\bar{V}^2$ while materials with $\bar{V} > 20$ meV show essentially the identical fission rates. Thus the experimental data are in quantitative agreement with the expected picture of a nonadiabatic-to-adiabatic transition in k_{fis}.

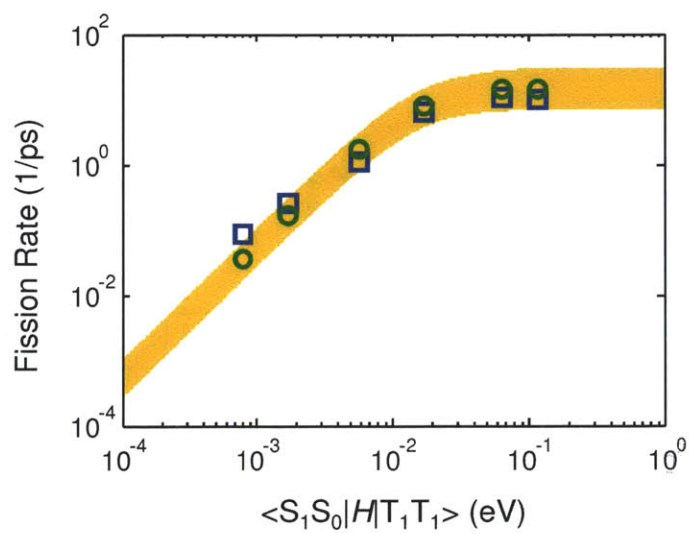

Figure 6-7 Measured (□) and predicted (○) rates of singlet fission for various pentacene derivatives. The values of parameters used for prediction were $\Delta G = -0.1$ eV, $\tau_{ad} \sim 40$ fs, and $\lambda = 0.15$ eV. The yellow area represents the range of predicted fission rates when the parameter values were varied by ±30%.

6.7 Discussion

Our results are in qualitative agreement with recent theoretical predictions that superexchange can significantly increase the coupling[80, 81] (i.e. $\bar{V}$ can be much larger than V). However, we do not find compelling evidence that superexchange is necessary for fast, efficient fission. Even neglecting the contributions of CT mixing, we find that a direct coupling governed by V still results in ultrafast fission rates in every material studied (see Figure 6-2). In particular, for cases where CT mixing significantly increases the coupling (Pc, TIPS-P, DTP) the reaction occurs adiabatically, so that changes in the coupling have a negligible effect on the rate. This observation is significant for the purposes of rational design, as it implies that one need not control ΔE_{CT} in order to ensure fast fission. A reasonably large V is sufficient.

The most significant loss mechanism for singlet fission is radiative decay from S_1, which typically occurs on the nanosecond timescale. Thus, every material in Figure 6-2 undergoes efficient fission, as confirmed by the absence of significant photoluminescence from any sample. This stands in contrast to the situation for MEG, where exicton multiplication must outcompete thermal relaxation on a sub-picosecond timescale, necessitating an MEG mechanism analogous to coherent fission. Thus, organic materials have a larger dynamic range and more freedom to accomplish carrier multiplication than their inorganic counterparts.

6.8 Conclusion

We have presented experimental confirmation of a fundamental model that correctly predicts the kinetics of singlet fission across a wide range of organic materials. Our results suggest that the rational design for novel fission materials should focus primarily on two features: 1) Making $E_S \gtrsim 2E_T$ and 2) Maintaining a reasonable coupling, V. It is not necessary, for example, to control the value of ΔE_{CT} or to maximize V. As long as the crystal is reasonably well-packed, V can be large enough to guarantee efficient fission. The necessary ingredients for rational design of singlet fission-based photovoltaic materials are now in place.

7. Singlet Exciton Fission in Hexacene: Toward Singlet Fission into Three Triplets

Hexacene, an acene with six benzene rings, is notable for its exceptionally small triplet energy, around one third of the singlet energy. We demonstrate singlet fission, conversion of a singlet exciton into two triplets, in a thin film of hexacene derivative employing both transient absorption spectroscopy and magnetic field effects on photocurrent.

7.1 Introduction

Singlet exciton fission, a process that converts a singlet exciton into two triplet excitons, has the potential to realize a high-efficiency solar cell that exceeds the Shockley-Queisser limit.[13] Singlet exciton fission has been previously employed to improve the photovoltaic efficiency of organic nanostructured solar cells,[102] photodetectors,[41] and hybrid organic-inorganic solar cells containing quantum dots.[33, 34, 103] It is typically observed when the energy of the singlet is close to or larger than twice the energy of the triplet. Tetracene and pentacene satisfy this criterion and have been shown to exhibit singlet fission.[13, 38, 69] Here, we confirm the presence of singlet fission in a derivative of hexacene, a six-ringed

acene, by employing both transient absorption spectroscopy and photovoltaic device measurements.

Singlet fission in hexacene attracts attention due to hexacene's exceptionally small triplet energy relative to the singlet energy. Whereas singlet exciton fission is approximately isoenergetic in tetracene and pentacene, hexacene is notable for its extremely small triplet energy, around one third of the singlet energy; see Figure 7-1b. The triplet energy of hexacene is predicted to be 0.46 eV from density functional calculations.[104] Extrapolation of triplet energies of smaller acenes estimates the hexacene triplet energy of 0.54±0.5 eV.[105] Optical absorption measurements yield singlet energies of 1.82 eV [105] and 1.65 eV (Figure 7-4b) for unsubstituted hexacene and substituted hexacene used in this study (Figure 7-1a), respectively. Thus, in hexacenes, the singlet energy ($E(S_1)$ = 1.65–1.82 eV) is around 0.6–0.8 eV higher than twice the triplet energy ($E(T_1)$ = ~0.5 eV), placing a singlet fission process in the Marcus inverted region,[13] in contrast to tetracene and pentacene. Furthermore, the unusual energy structure of hexacene satisfies the energetic requirements for fission of a singlet into *three* triplets, a potentially useful phenomenon in solar cells.

Unsubstituted hexacene is known to be very unstable and dimerize quickly in solution.[106] Its stability can be improved by functionalization.[107, 108] Alternatively, it has been recently reported that hexacene crystals can be synthesized by heating solid-state precursors, avoiding the problem of low stability in solution.[109] In this work, we use hexacene substituted with tricyclohexylsilylethynyl (TCHS) groups, which increases stability and solubility[108]; see Figure 7-1a for the molecular structure. The improved

stability has been used to demonstrate charge transport through TCHS-hexacene thin films on a field-effect transistor.[110]

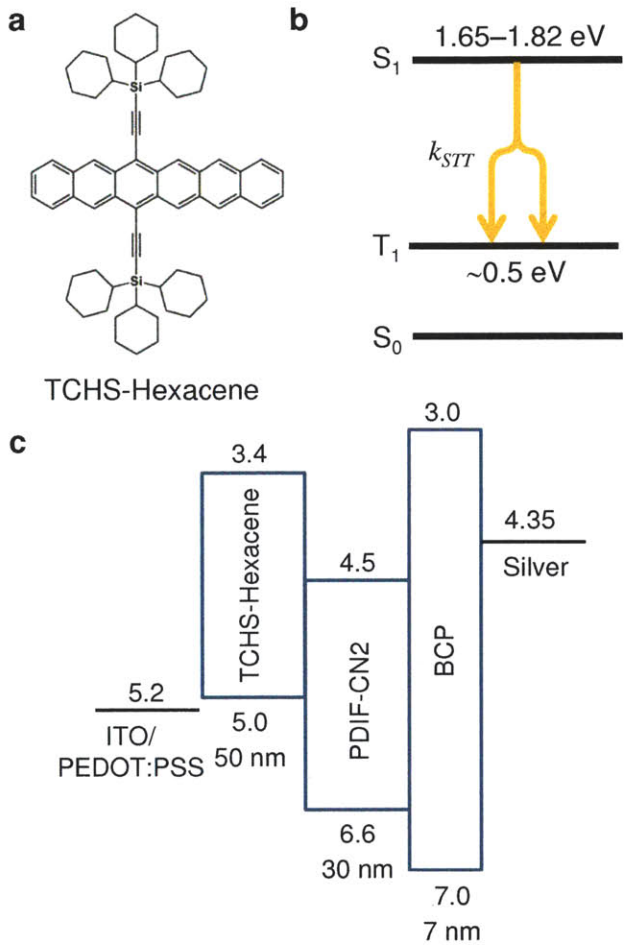

Figure 7-1 **(a)** The molecular structure of TCHS-hexacene. **(b)** Singlet fission process in hexacene. The singlet energy level is from optical absorption measurements. The triplet energy is from density functional calculations ($E(T_1)$ = 0.46eV) [104] and extrapolation of triplet energies of smaller acenes ($E(T_1)$ = 0.54±0.5eV) [105]. **(c)** Schematic energy diagram of a photovoltaic device incorporating TCHS-hexacene. The energy levels are from Ref. 110, 111, and Polyera Corp.

7.2 Experimental Technique

7.2.1 Sample Fabrication

TCHS-hexacene was synthesized as reported in Ref. 108. Devices were fabricated on precleaned glasses coated with ITO. PEDOT:PSS was spin-coated on the glass. TCHS-hexacene was dissolved in chlorobenzene at the concentration of 10 mg/ml and spin-coated on the substrates. All other layers were thermally evaporated at the pressure of 3×10^{-6} torr. The silver cathode was defined by a 1 mm diameter mask. Devices were packaged in a nitrogen environment. The samples for transient absorption measurements were prepared by spin-coating TCHS-hexacene solutions on quartz substrates and packaged in nitrogen. The optical absorption of thin films was measured using integrating spheres.

7.2.2 Transient Absorption Spectroscopy

Broadband transient absorption spectra in the visible and near-infrared were obtained using a 1 kHz repetition rate Ti:Sapphire amplified laser system and optical parametric amplifier (OPA). Briefly, a typical pump-probe setup is employed whereby materials are resonantly excited with ~100 fs laser pulses generated by the OPA and probed with a broadband supercontinuum pulse produced by focusing a small portion of the amplified laser fundamental into a sapphire plate [112]. Multi-wavelength transient spectra are recorded at various time delays between the pump and probe pulses using dual spectrometers (signal and reference channels) equipped with fast Si or InGaAs based array detectors.

7.3 Transient Absorption on Singlet Exciton Fission

Figure 7-2 presents a demonstration of singlet fission in TCHS-hexacene thin films using

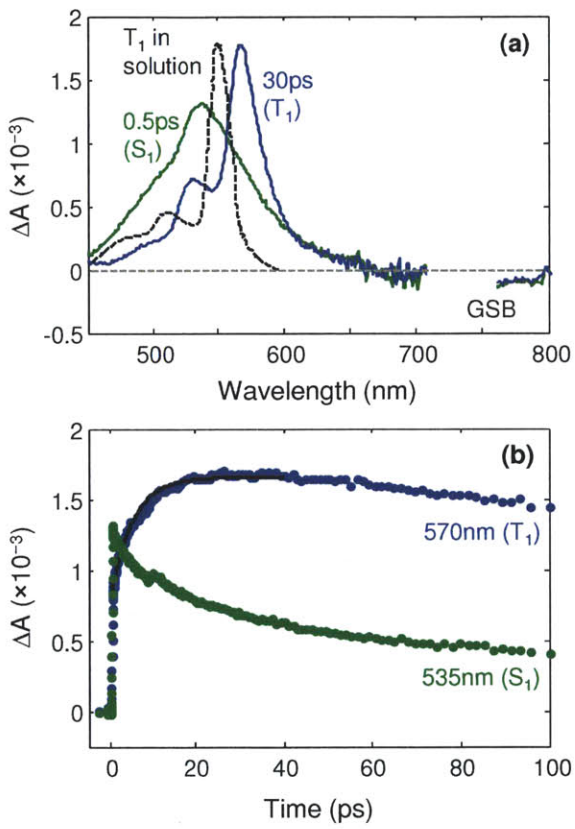

Figure 7-2 (a) Transient absorption spectra of TCHS-hexacene thin films. The photoinduced absorption spectra of singlets (solid green) and triplets (solid blue) were captured at 0.5 ps and 30 ps after laser excitations, respectively. GSB means ground state bleaching. The photoinduced absorption spectrum of triplets of unsubstituted hexacene in solution (dotted black) is from Ref. 105 and its scale is arbitrary. **(b)** Photoinduced absorption kinetics of the 535 nm (green) and 570 nm (blue) peaks, where singlets and triplets dominate, respectively. The black solid line is an exponential fitting with $\tau =$ 5.1±0.3ps.

transient absorption spectroscopy. Figure 7-2a shows the change of transient absorption spectra over time. The pump wavelength was 750 nm and the pulse irradiance was ~10 μJ/cm^2 and we verified the absence of singlet-singlet annihilation by confirming the independence of the transient shape on the pump intensity. The signal around $\lambda = 750$ nm was omitted due to the scattering of incident pump light. The broad peak around 535 nm is assigned as photoinduced absorption of singlets as it appears immediately after photoexcitation. The spectrum changes to the peak around 570 nm over tens of picoseconds, which is attributed to the $T_1 \rightarrow T_n$ transition, because the spectrum resembles the triplet photoinduced absorption spectrum of unsubstituted hexacene measured in solution [105]. Previously, the triplet-triplet absorption spectrum of silylethynyl-substituted pentacene was shown to be almost identical to that of unsubstituted pentacene [98]; thus we assume that the insertion of TCHS groups does not greatly alter the photoinduced absorption spectrum of hexacene triplets. However, the TCHS group could be responsible for the 20 nm redshift of the triplet photoinduced absorption in TCHS-hexacene thin films compared to unsubstituted hexacene solutions. Alternatively, the redshift may be due to the higher polarizability in solid-state films than in solutions; a similar effect was observed in pentacene [98] and tetracene [113, 114].

The small negative signal at $\lambda = 770$–800 nm is assumed to originate from bleaching of the ground state as the spectrum agrees with the absorption spectrum shown in Figure 7-4b. The analysis of time-resolved dynamics in this region was obscure because the signal was noisy and a residual of triplet photoinduced absorption may also contribute to this region.

Figure 7-2b displays the kinetics of singlet and triplet photoinduced absorptions. The 535 nm and 570 nm peaks represent singlets and triplets; however, note that the singlet and triplet photoinduced absorption spectra overlap and the 535 nm (570 nm) signal includes some contribution from the triplet (singlet) photoinduced absorption. As the singlets decay, the triplets rise, demonstrating singlet fission in TCHS-hexacene thin films. The rate of triplet formation is determined to be $1/(5.1\pm0.3)\ \mathrm{ps}^{-1}$ by fitting the growth of triplet populations. It is much faster than the fluorescence decay rate ($1/1.5\ \mathrm{ns}^{-1}$) of hexacene in solution.[115] The attachment of silylethynyl groups does not induce intersystem crossing as shown in silylethynyl-functionalized pentacene exhibiting the fluorescence time constant of 11.8 ns [116]. Both 535 nm and 570 nm signals start to drop after $t = 40$ ps; quenching of the excitons could be caused by the air/molecule interface and the bulk trap states inside thin films.

7.4 Magnetic Field Effect on Photocurrent

7.4.1 Device Structure and External Quantum Efficiency

Confirmation of singlet fission in TCHS-hexacene thin films is obtained by monitoring the photocurrent change of TCHS-hexacene photovoltaic devices under magnetic fields. We built a bilayer photovoltaic cell with the heterojunction based on TCHS-hexacene and N,N'-bis(1H, 1H-perfluorobutyl)-(1,7 & 1,6)-dicyano-perylene-3,4:9,10-bis(dicarboximide) (PDIF-CN2) [33]. The LUMO level of PDIF-CN2 is low enough to dissociate the triplets of TCHS-hexacene; see Figure 7-1c for the device structure and energy diagrams. The device structure was indium tin oxide (ITO)/poly(3,4-

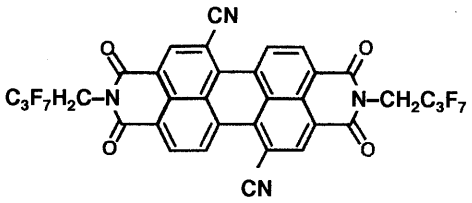

PDIF-CN2

Figure 7-3 The molecular structure of PDIF-CN2

ethylenedioxythiophene):poly(styrenesulfonate) (PEDOT:PSS, 38 nm)/TCHS-hexacene (50 nm)/PDIF-CN2 (30 nm)/ bathocuproine (BCP, 7 nm)/aluminum (100 nm).

Figure 7-4a plots the external quantum efficiency (EQE) spectrum of a TCHS-hexacene photovoltaic cell. It is notable that TCHS-hexacene shows photocurrent responses at $600 < \lambda < 800$ nm; see Figure 7-4b for the absorption spectrum of a TCHS-hexacene layer. The low external quantum efficiency is likely due to the poor charge extraction at the heterojunction of TCHS-hexacene and PDIF-CN2. The photocurrent at $V = -1$ V is 15 times larger than at $V = 0$ V, indicating severe charge recombination in the device; see Figure 7-5 for the dark and light current–voltage characteristics. Poor charge collection may be due to the low charge mobility of TCHS-hexacene (1.7×10^{-4} $cm^2V^{-1}s^{-1}$) [110] and the small energy gap of charge transfer states (~0.5 eV), which results in fast charge recombination under Marcus theory[117].

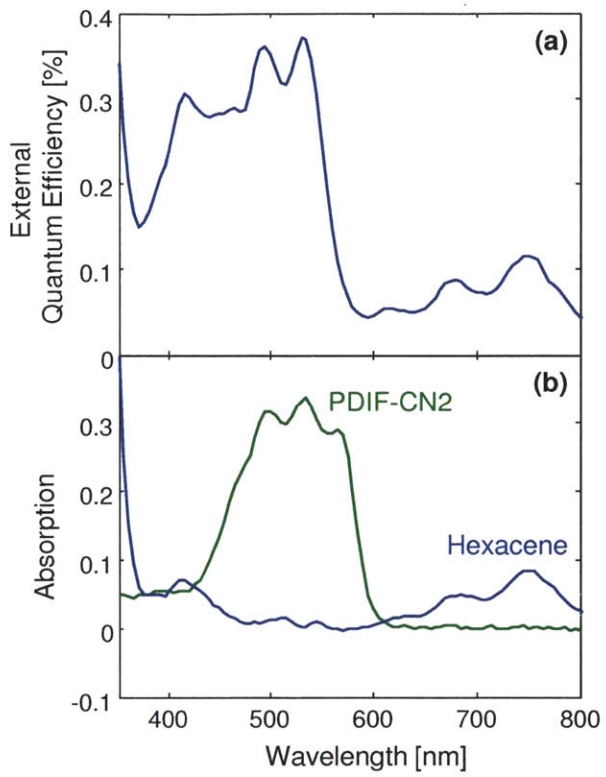

Figure 7-4 **(a)** Short circuit external quantum efficiency as a function of wavelength for a TCHS-hexacene photovoltaic cell. **(b)** Absorption spectra of TCHS-hexacene and PDIF-CN2 thin films.

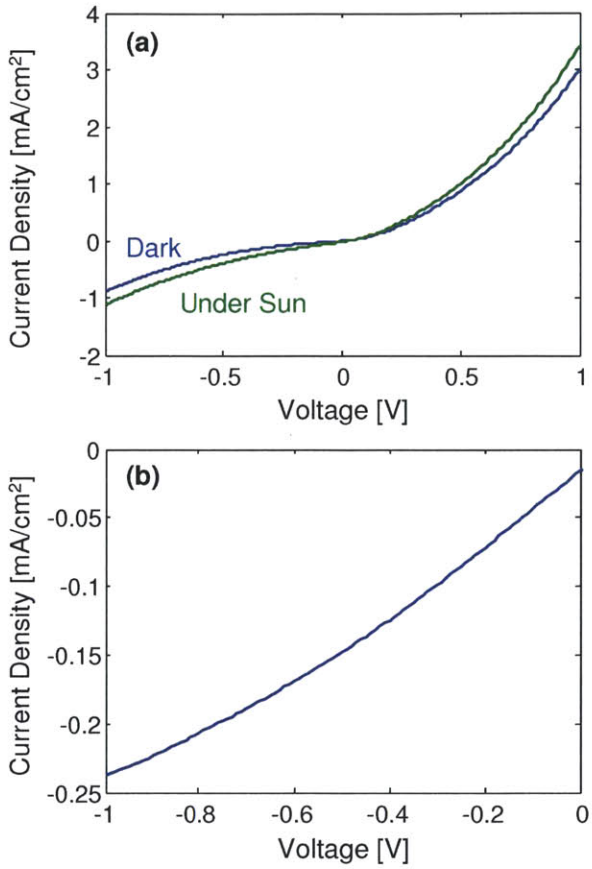

Figure 7-5 **(a)** Current–voltage characteristics of hexacene photovoltaic cells under dark (blue) and 1 sun illumination (green) conditions. **(b)** The difference between light and dark current. The photocurrent, obtained by subtracting the dark current from the current under illuminations, exhibits 15 times more current at $V = -1$V than at $V = 0$V.

7.4.2 Magnetic Field Dependence of Photocurrent

Figure 7-6 plots the magnetic field dependence of the photocurrent for the selective illumination of TCHS-hexacene and PDIF-CN2. LEDs with the wavelengths of 660 nm and 530 nm are used to photoexcite TCHS-hexacene and PDIF-CN2 layers, respectively. A voltage of −0.25 V was applied to promote charge extraction and minimize the secondary magnetic field effect coming from triplet-polaron annihilation.[41, 118] It is notable that TCHS-hexacene exhibits the strong positive modulation up to 4.7 % at a small magnetic field of $H < 0.1$ T and the negative response down to −5 % at a magnetic field of $H > 0.2$ T, whereas the photocurrent upon PDIF-CN2 illumination exhibits nearly constant positive modulation of 1–2 %. Similar phenomena were observed in tetracene- and pentacene-based photovoltaic devices,[41, 102] verifying the existence of singlet fission. The magnetic field effects from the donor and acceptor sides are distinct, confirming that the energy transfer from the acceptor to the donor is negligible.

Johnson and Merrifield's theory explains the characteristic shape of the magnetic-field-induced photocurrent change upon TCHS-hexacene illuminations.[8, 25] The rate of singlet fission is proportional to the fractional singlet character of a pair of triplet excitons resulting from singlet fission, which has nine different spin configurations. In the absence of a magnetic field, three configurations out of nine have singlet character. Under a small magnetic field, i.e. $H < 0.1$ T, the singlet character is distributed over six states, increasing the rate of singlet fission. At a high magnetic field, i.e. $H > 0.2$ T, there are only two states with singlet character, slowing down a singlet fission process. This behavior of the fission rate under a magnetic field agrees well with our magnetic field effect on photocurrent, which rises at $H < 0.1$ T and decreases at $H > 0.2$ T. Also, the

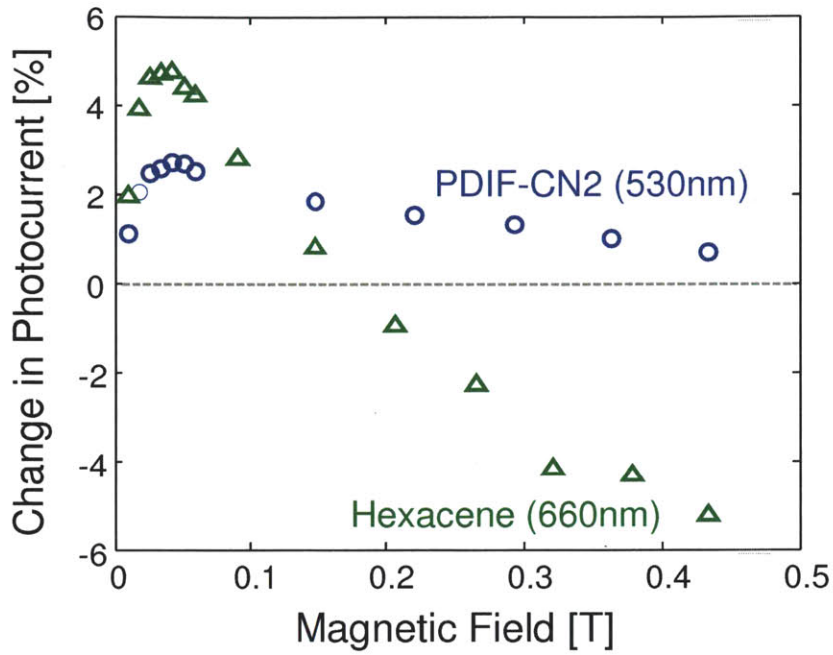

Figure 7-6 Photocurrent change under magnetic fields upon photoexciting TCHS-hexacene (λ = 660nm) and PDIF-CN2 (λ = 530nm) in a hexacene solar cell. A voltage of –0.25 V was applied during the measurement.

negative magnetic field effect under a high magnetic field confirms that TCHS-hexacene triplet excitons indeed break up into charges; the positive magnetic field effect has been observed in the donor-acceptor system where triplet excitons generated from singlet fission cannot dissociate into charges due to the large energy barrier to charge transfer.[33] It is also notable that the magnetic field effect can be observed only when triplet generation competes with dissociation of singlet excitons into charge.[41] This implies that singlet exciton diffusion and charge transfer processes in TCHS-hexacene devices take place on the picosecond timescale, comparable to singlet fission.

The small positive magnetic field effect upon PDIF-CN2 photoexcitation may be due in part to the magnetic field response from triplet-polaron annihilation [118] and was also observed in pentacene/C_{60} photovoltaic devices upon C_{60} illumination [41].

7.5 Conclusion

To summarize, we demonstrated singlet fission in substituted hexacene, which features an extremely small triplet energy compared to the singlet energy, by employing transient absorption spectroscopy and magnetic field effect on photocurrents produced from singlet fission. We measure the fission rate of $1/(5.1\pm0.3)$ ps^{-1} in TCHS-hexacene thin films. In TCHS-hexacene/PDIF-CN2 heterojunction devices, we observe the photocurrent reduction of -5 % during selective illumination of TCHS-hexacene, confirming the presence of singlet fission. Our findings should provide the device and spectroscopic basis for further work on molecules with low energy triplet excitons where fission may yield more than two triplets per singlet exciton.

8. Charge Transfer State Versus Hot Exciton Dissociation in Organic Solar Cells

We examine the significance of hot exciton dissociation in two archetypical polymer-fullerene blend solar cells. Rather than evolving through a bound charge transfer state, hot processes are proposed to convert excitons directly into free charges. But we find that the internal quantum yields of carrier photogeneration are similar for both excitons and direct excitation of charge transfer states. The internal quantum yield, together with the temperature dependence of the current-voltage characteristics, is consistent with negligible impact from hot exciton dissociation.

8.1 Introduction

The conversion of excitons into charge within organic solar cells is complicated by the uncertain role of bound electron-hole pairs, or charge transfer (CT) states at donor-acceptor interfaces.[119-121] In this report, we perform direct photocurrent spectroscopy on CT states within organic solar cells. Our techniques allow us to decisively conclude that bound CT states mediate the conversion of excitons into charge. In contrast with

expectations,[119, 122-125] we find that charge generation is efficient despite the absence of 'hot' dissociation of excitons directly into charge. These findings confirm prior suggestions[120, 121, 126] that the photocurrent generation in organic solar cells is controlled by the recombination dynamics of thermally relaxed CT states.

Spectroscopy by Muntwiler *et al.* has determined that the binding energy of CT states is typically well in excess of 0.1 eV.[119, 122] However, modern organic solar cells exhibit near-unity quantum yield, demonstrating that charge is efficiently generated despite the large binding energy of the CT state.[127] To resolve this possible conflict, a hot process of charge transfer has been proposed, whereby the excess energy from exciton dissociation, $E_{CT} = E_X - E_{CT}$, contributes to the dissociation of CT states. Here, E_X and E_{CT} are the energies of the exciton and CT states, respectively. In support of this model, it was observed that the population of free charge carriers increases as E_{CT} gets larger,[123, 124] and Pensack *et al.* showed that the rate of free carrier formation is temperature-independent; implying that charge separation is barrier-less.[125]

In this report, we investigate the significance of hot exciton dissociation processes by comparing CT states generated from either excitons or direct photoexcitation. This approach is feasible because mixtures of polymers (donors) and fullerene molecules (acceptors) exhibit a new absorption band at infrared wavelengths. This broad absorption band is attributed to the formation of bound CT states, mediated by the interaction of the highest occupied molecular orbital (HOMO) of donors with the lowest unoccupied molecular orbital (LUMO) of acceptors.[128-130] Thus, one can create thermally-relaxed CT states by optically exciting the CT transition band directly.

8.2 Charge Transfer State or Hot Exciton Dissociation?

As shown in Figure 8-1, CT states are excited directly and indirectly by below-gap and above-gap illumination, respectively. The existence of a hot CT process should yield observable differences in free carrier generation. First, we compare the internal quantum efficiency of directly-excited CT states and CT states generated from excitons. Second, we measure the open-circuit voltage (V_{OC}), a key charge recombination metric, under below-gap and above-gap illuminations with equivalent CT state generation rates. We

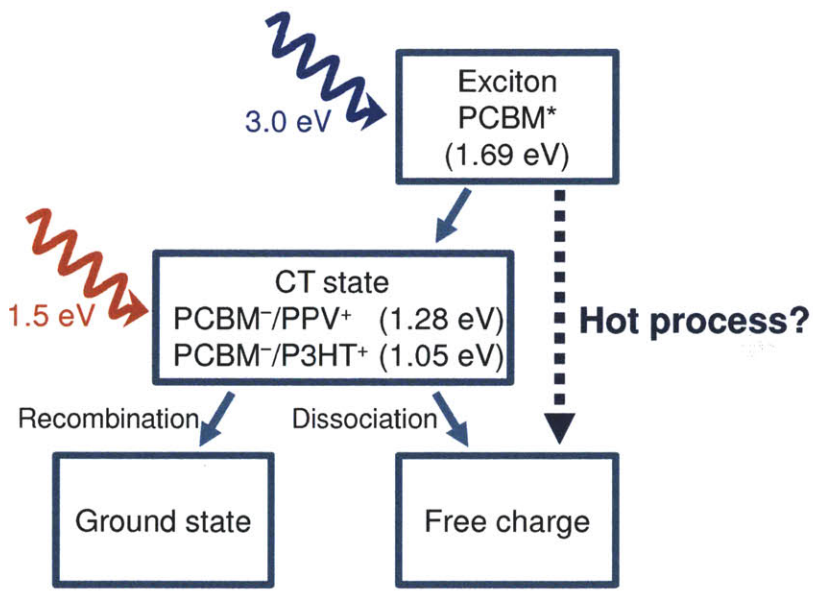

Figure 8-1 Hot exciton dissociation processes are probed by comparing the output of solar cells under direct photoexcitation of either excitons or CT states. In a hot dissociation process, a donor or acceptor exciton breaks directly into free charge carriers without populating a bound, relaxed CT state. Alternatively, direct photoexcitation of CT states creates these bound CT states. The energy levels of excitons on PCBM molecules and CT states at the MDMO-PPV (P3HT)/PCBM interface are determined from the luminescence spectra.[13]

also evaluate the temperature dependence of photocurrent for those two excitations.[131]

We study two archetypical photovoltaic systems: bulk heterojunctions of poly[2-methoxy-5-(3′,7′-dimethyloctyloxy)-1,4-phenylenevinylene] (MDMO-PPV) and poly-3(hexylthiophene) (P3HT) mixed with 1-(3-methoxycarbonyl)-propyl-1-phenyl-[6,6]C61 (PCBM). Goris *et al.*[132, 133] and Vandewal *et al.*[129] previously demonstrated weak absorption and photocurrent generation from CT states in these heterojunctions. Time-resolved transient absorption spectroscopy by Drori *et al.* on polymer-fullerene blends has shown that below-gap excitation efficiently produces polarons on the polymer chains and fullerene molecules.[134]

8.3 Calculation of Charge Transfer States

The existence of below-gap CT states in these blends is supported by constrained density functional calculations.[88] Several MDMO-PPV/PCBM and P3HT/PCBM heterodimers were simulated with various intermolecular orientations. The surrounding molecules were assumed to provide a uniform dielectric surrounding the pair with $\varepsilon = 4$. The resulting CT states were bound by 0–0.4 eV for MDMO-PPV/PCBM and 0–0.5 eV for P3HT/PCBM. The HOMO-LUMO band offset at the interface was 1.6 eV (1.6 eV) for MDMO-PPV/PCBM (P3HT/PCBM) suggesting CT absorption should be active between 1.2–1.6 eV for MDMO-PPV/PCBM and 1.1–1.6 eV for P3HT/PCBM. The calculated CT energies may be redshifted because the density functional calculation over- delocalizes the electrons and, consequently, underpredicts the ionization potential of the polymers significantly.[135] The predicted CT energies are in agreement with the optical characterization by Goris *et al.*[132, 133] and Vandewal *et al.*[129]

Here we describe the details of our constrained density function calculations. Two different sets of calculations were performed on MDMO-PPV/PCBM and P3HT/PCBM heterodimers. In the first set, the transport gaps (TGs) of each polymer and PCBM were

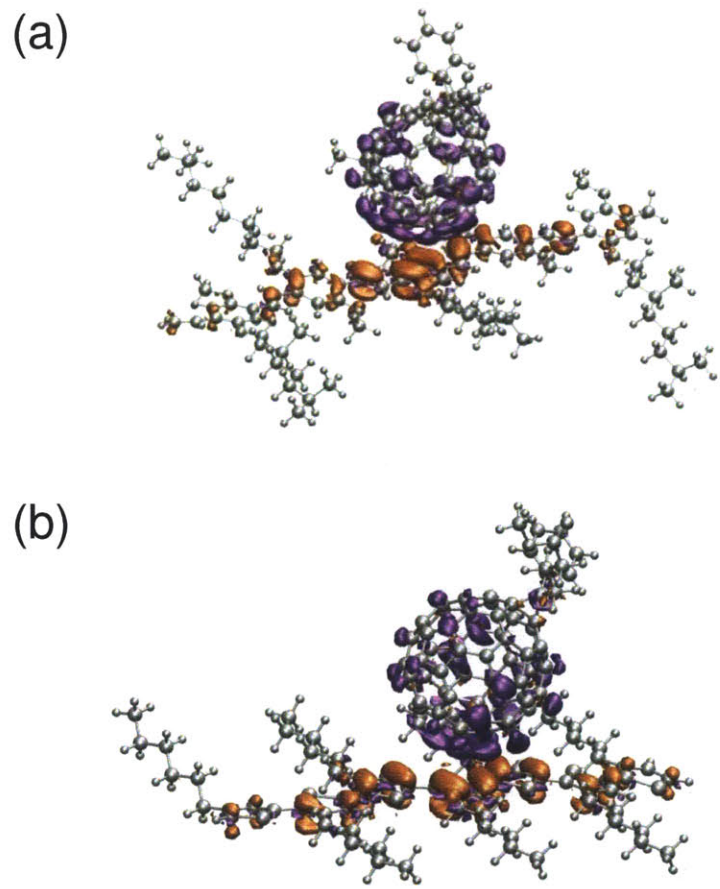

Figure 8-2 (a) The calculated charge-density difference between the CT state and the ground state of an MDMO-PPV/PCBM heterodimer. The violet (orange) surfaces show where the CT state has more (less) electron density. In each picture PCBM is constrained to have an extra electron and a 5-unit MDMO-PPV is constrained to have a hole. **(b)** The corresponding picture for a P3HT/PCBM pair. The PCBM is constrained to have an extra electron and the 7-unit P3HT is constrained to have one less electron.

calculated using Turbomole. In the second set, the charge transfer (CT) states were simulated using constrained density functional theory (CDFT)[136] in Q-Chem. Both sets used the B3LYP functional. Due to the limits of our computational power, the calculated CT energies and TGs of finite chain lengths (n = 3–6 for MDMO-PPV, n = 4–8 for P3HT) were exponentially fitted to extrapolate the energies of infinite chain length. For the same reason, the CT state calculations with the larger basis set (6-311++G**) could not be completed. Therefore, we computed the TG and CT states with a smaller basis set (6-31G*) to obtain the binding energy, which is an energy difference between free and bound charges, because it will change by very little when the basis set is increased. Final TG calculations were done in the larger basis set (6-311++G**) in order to approach the basis set limit for these calculations and obtain a more accurate prediction.

The CT state geometries were created by placing the geometry-optimized donor and acceptor at varying intermolecular distances and orientations, while optimizing each polymer and PCBM geometry in Q-Chem with the 6-31G* basis set in gas phase. Our goal in this simulation is to find a lower bound to the CT state energy. Thus, we selected the geometry in which the plane of a polymer is parallel to one of the hexagonal faces on PCBM, maximizing the orbital overlap; see an example for MDMO-PPV/PCBM and P3HT/PCBM in Figure 8-2, respectively. PCBM's solvation group was pointed away from the interface. The separation distance was varied (d = 3–4.3 Å), and the CT energy with PCBM rotated by 90° was also probed. The chosen geometries are optimal for electron transfer, and any distortion of the planes of polymers or large separation between the two molecules leads to a higher CT energy.

The TGs were calculated in Turbomole with the COSMO solvation model and the 6-311++G** basis. A dielectric constant of $\varepsilon = 4$ was used for MDMO-PPV and PCBM, and $\varepsilon = 3.5$ was used for P3HT[137, 138]. For each geometry, the anion (cation) energies $E_{a(c)}$ and ground state energies E_g were computed for PCBM (MDMO-PPV, P3HT). Figure 8-3 displays the ionization potential (IP = $E_c - E_g$) of MDMO-PPV and P3HT with different chain lengths. The electronic affinity (EA = $E_g - E_a$) of PCBM was found to be 3.27 eV. Thus, the TG (TG = IP – EA) calculated in the 6-311++G** basis is 1.6 eV (1.6 eV) for MDMO-PPV (P3HT)/PCBM pairs.

The CT calculations could not be completed in the 6-311++G** basis due to computational limits. Therefore, in order to determine the CT binding energies, we repeated the TG calculations in the 6-31G* basis; see Figure 8-3. The EA of PCBM was found to be 2.87 eV. We obtained the TGs for MDMO-PPV/PCBM (P3HT/PCBM) of 1.7 eV (1.8 eV) in the 6-31G* basis. The CT binding energies were finally determined from the difference between the TG and CT state energies.

The CT state energies were calculated using the 6-31G* basis with CDFT and the SM8 solvation model in Q-Chem. The constraints of the model placed an extra electron on PCBM and removed one electron from MDMO-PPV and P3HT. Hexanoic acid was selected as the solvent for the SM8 model, ensuring that the solvation energy acquired from Q-Chem is comparable to that from Turbomole. Figure 8-3 shows the calculated CT state energies; note that both systems have a negligible variance up to 0.04 eV for different intermolecular geometries. We find that the CT states are bound by up to a maximum of 0.4 eV (0.5 eV) for MDMO-PPV/PCBM (P3HT/PCBM). The resulting CT state energies range between 1.2–1.6 eV (1.1–1.6 eV) for MDMO-PPV/PCBM

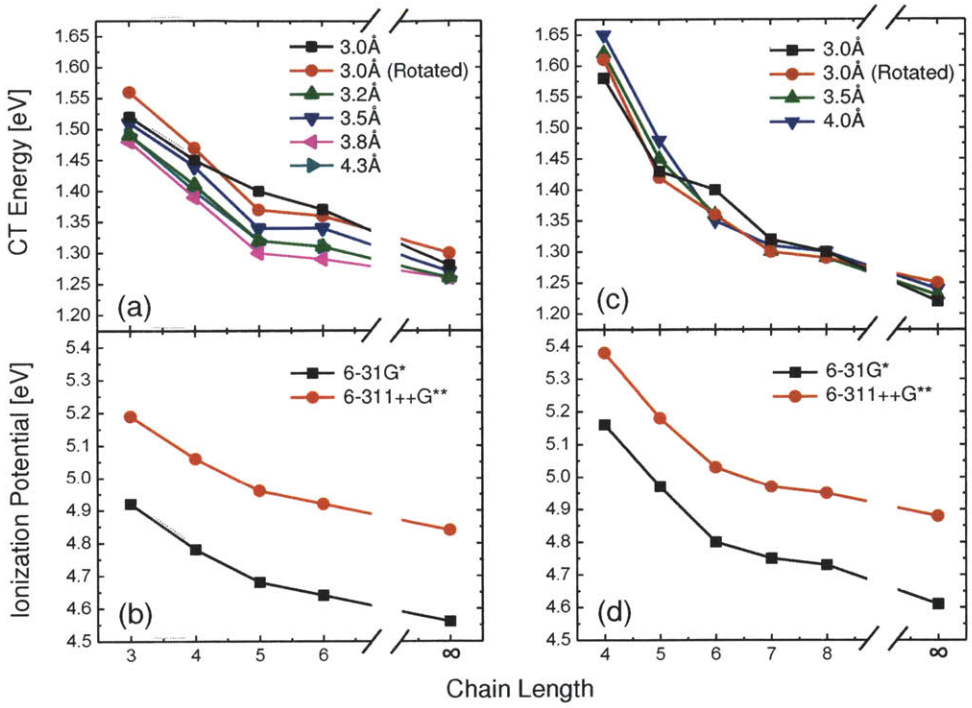

Figure 8-3 **(a)** The CT state energies of MDMO-PPV/PCBM with respect to chain lengths for different donor-acceptor separations. The configuration with PCBM rotated by 90° was also investigated. **(b)** The ionization potentials (IP) of MDMO-PPV with respect to chain lengths calculated in the different basis sets. **(c), (d)** The equivalent of (a) and (b) for P3HT/PCBM.

(P3HT/PCBM). These results verify that the below-gap illuminations for the MDMO-PPV/PCBM and P3HT/PCBM systems are most likely to excite the CT states directly.

8.4 Experimental Method

The spectral quantum efficiency and the absorption coefficient of organic layers were measured with a high sensitivity using Fourier-transform photocurrent spectroscopy (FTPS) and photo-thermal deflection spectroscopy (PDS), respectively, as described in

Ref. 129 and 132. PDS was performed on ~200nm-thick MDMO-PPV:PCBM and ~250nm-thick P3HT:PCBM films on quartz substrates. FTPS was carried out on devices prepared with the same film thickness, sandwiched between indium tin oxide (ITO)/poly(3,4-ethylenedioxythiophene):poly(4-styrenesulphonate) (PEDOT:PSS) and Ca/Al electrodes.

For electric-field- (Figure 8-9) and temperature-dependent (Figure 8-7) characterization, devices were fabricated on precleaned glass substrates coated with a 1600Å-thick layer of ITO and a 300Å-thick layer of PEDOT:PSS. MDMO-PPV, P3HT, and PCBM were dissolved in chlorobenzene and spin coated to a thickness of ~70nm. A LiF/Al contact was deposited by thermal evaporation at high vacuum ($< 3\times10^{-6}$ Torr), and defined by a 1-mm-diameter shadow mask. After contact deposition, P3HT:PCBM devices were annealed for 5 minutes at 100C in a nitrogen environment. For temperature-dependent measurements, devices were kept inside a continuous flow of helium. Diode lasers with photon energies of 3.0 eV and 1.5 eV were used as light sources. The current-voltage characteristics were recorded using a HP4156 semiconductor parameter analyzer.

8.5 Internal Quantum Efficiency of Below-gap and Above-gap CT States

Figure 8-4 shows the external quantum efficiency (EQE) at short-circuit conditions compared with the optical absorption of blends of MDMO-PPV:PCBM (1:4 by weight) and P3HT:PCBM (1:1 by weight). The absorption coefficients of each component in the blends are also shown. The weak absorption under 1.6 eV, observed for mixtures of the

polymer and PCBM, is attributed to CT absorption.[129, 130] The lowest energy part of the absorption spectra, below 1.4 eV and 1.2 eV for MDMO-PPV:PCBM and P3HT:PCBM systems, respectively, can be attributed to light- and aging-induced features and not CT transitions, as the absorption in this region increases upon repeating measurements on the same film; see Figure 8-5.

Figure 8-4 shows the optical absorption of blends of MDMO-PPV:PCBM (1:4 by weight) and P3HT:PCBM (1:1 by weight) compared with the external quantum efficiency (EQE) at short-circuit conditions. The lowest energy part of the absorption spectra, below 1.4 eV and 1.2 eV for MDMO-PPV:PCBM and P3HT:PCBM systems, respectively, can be attributed to light- and aging-induced features and not CT transitions, as the absorption in this region increases upon repeated measurements on the same film.

We fitted the EQE spectrum calculating the absorption of organic layers, *i.e.*, $A = A_0(1-\exp(-2\alpha \cdot d))$, where A_0 accounts for the loss from ITO and PEDOT:PSS layers and is assumed to be 0.85, α is the absorption coefficient measured with PDS, and d is the thickness of the blended films. Consequently, we obtained internal quantum efficiencies (IQE) of (45±10)% and (80±10)% for MDMO-PPV:PCBM and P3HT:PCBM devices, respectively; see Figure 8-6 for the IQE as a function of energy. The fit, constant across full wavelength range from above to below the optical gap, strongly suggests that the energies of excited CT states do not greatly influence CT state dissociation. Every optically-accessible exciton and CT state exhibits a similar probability of charge generation or recombination. Even if our below-gap optical excitation generates hot CT states, we find no change in the efficiency of charge generation despite varying the below gap excitation energy by several tenths of an eV.

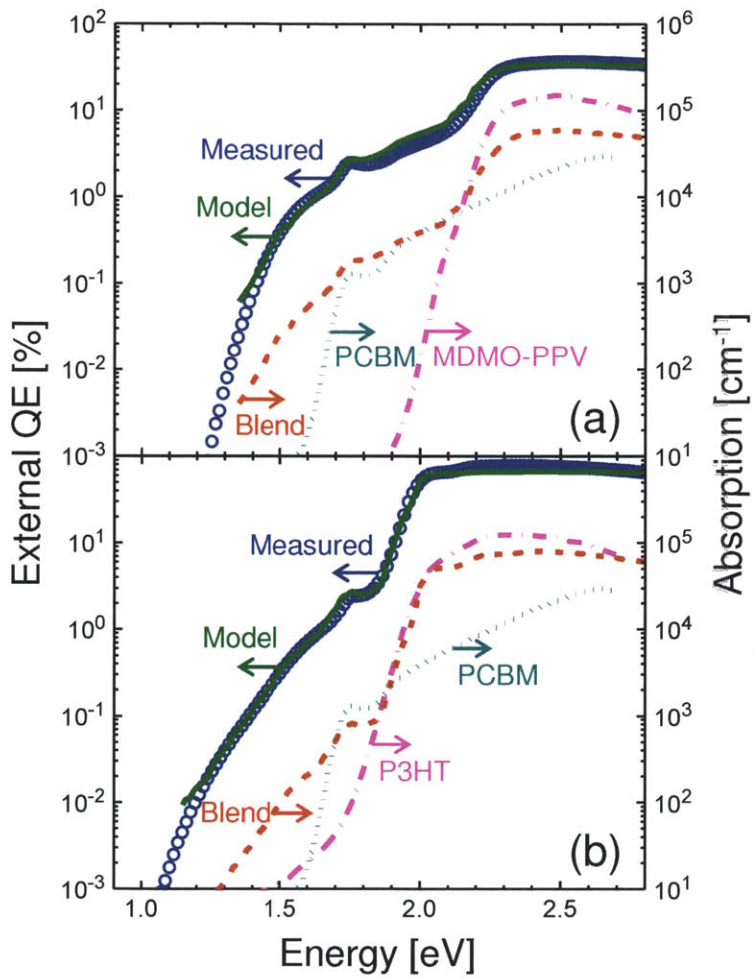

Figure 8-4 **(a)** The external quantum efficiency (EQE) spectrum (circles) under short-circuit conditions compared to the absorption spectrum of an MDMO-PPV:PCBM device. The absorption coefficients of MDMO-PPV (dash-dotted line), PCBM (dotted line), and blends (dashed line) are shown. The EQE was fit using IQEs of (45±10)%. **(b)** The EQE spectrum (circles) and absorption spectrum of a P3HT:PCBM device. An IQE of (80±10)% was obtained. For both heterojunctions, the CT state absorption band exhibits a charge collection efficiency similar to that of the polymer or PCBM.

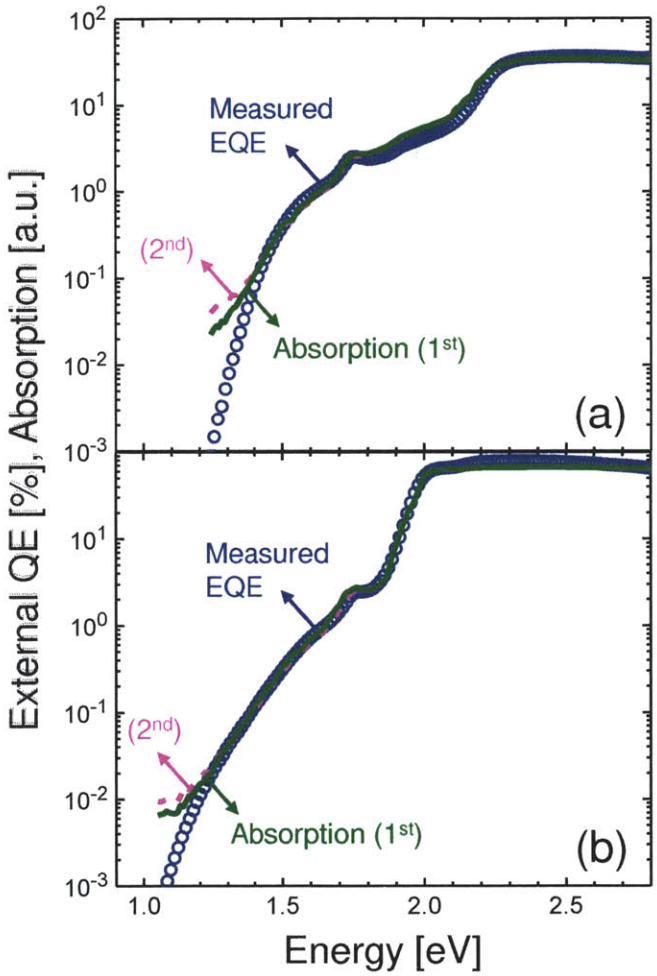

Figure 8-5 **(a)** The absorption spectrum of an MDMO-PPV:PCBM device compared with external quantum efficiency (EQE) spectrum (circles) under short-circuit conditions. The absorption spectra measured on the first (solid) and second (dash) runs are shown. For comparison with the EQE, the absorption spectra were multiplied with the internal quantum efficiency (IQE) of (45±10)%. **(b)** The equivalent of (a) for a P3HT:PCBM device. The IQE is (80±10)%.

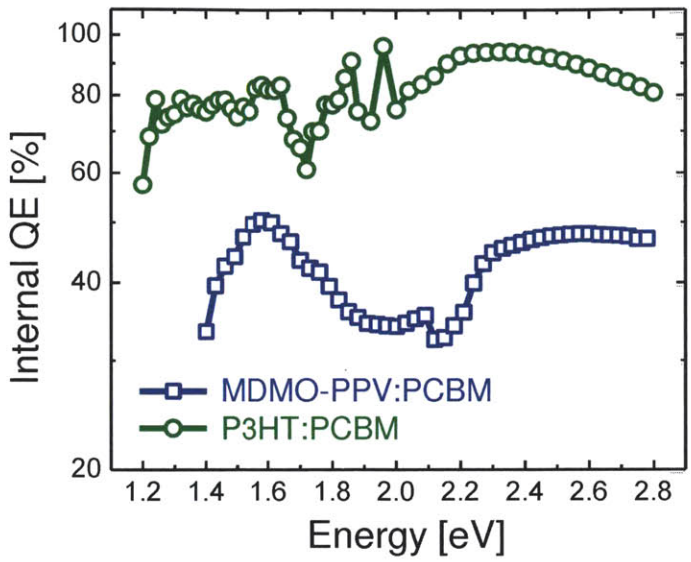

Figure 8-6 The internal quantum efficiency spectra of MDMO-PPV:PCBM (squares) and P3HT:PCBM (circles) devices, respectively. The IQE was obtained by calculating IQE(E) = EQE(E) / A(E), where A is the absorption of organic layers. A is given by $A = A_0 (1-\exp(-2\alpha \cdot d))$, where A_0 accounts for the loss from ITO and PEDOT:PSS layers and is assumed to be 0.85, α is the absorption coefficient measured with PDS, and d is the thickness of the blended films. The average IQE_m, calculated as $\log(IQE_m) = \sum \log(IQE(E)) / n$, are (45±10)% and (80±10)% for MDMO-PPV:PCBM and P3HT:PCBM devices, respectively. The internal quantum efficiencies are energy-independent across full wavelength range from above to below gap.

8.6 Temperature Dependence of Photocurrent under Below-gap and Above-gap Excitations

Figure 8-7 compares V_{OC} and photocurrents under below-gap and above-gap excitations at varying temperatures. Diode lasers with photon energies of 3.0 eV and 1.5 eV were used as light sources. Details of the device structure, fabrication, and characterizations are described in Section 8.4. In order to equalize the initial CT generation rate for both excitations, the incident light intensity was adjusted using optical density filters to obtain a short-circuit current density of $J = 32$ A/cm^2 (for MDMO-PPV:PCBM) or $J = 0.11$ mA/cm^2 (for P3HT:PCBM) at 280K for both laser wavelengths. For both heterojunctions, the photocurrent density decreased by more than an order of magnitude when the temperature was reduced from room temperature to below 50K; see Figure 8-8.

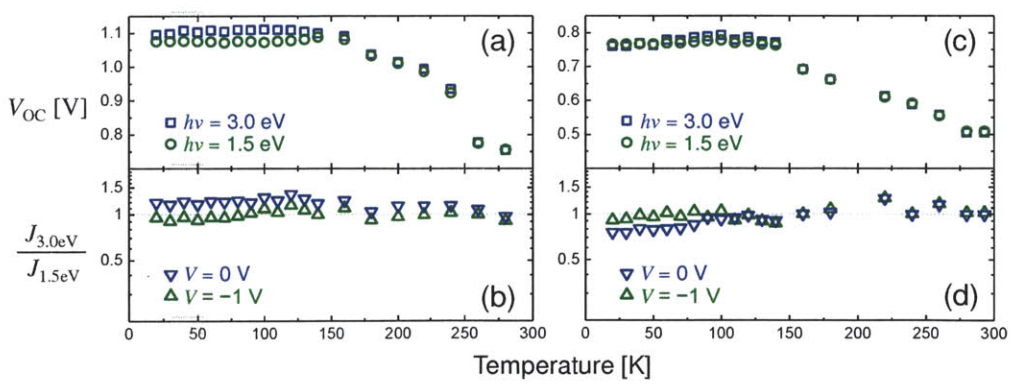

Figure 8-7 (a) The open-circuit voltage of an MDMO-PPV:PCBM device as a function of temperature under above-gap ($h\nu = 3.0$ eV, squares), and below-gap ($h\nu = 1.5$ eV, circles) excitations **(b)** The photocurrent ratio of above-gap and below-gap excitations at a voltage of $V = 0$V (∇) and $V = -1$V (Δ). **(c), (d)** The equivalent of (a) and (b) for a P3HT:PCBM device, respectively.

V_{OC} is a key indicator for charge recombination in organic solar cells, and is logarithmically proportional to the photocurrent under the electric field at an open-circuit condition.[139, 140] In both heterojunctions, we cannot resolve a difference in V_{OC} for temperatures above 130K when CT states are excited rather than donor or acceptor excitons. But V_{OC} is (30±5) mV higher for above-gap excitation in MDMO-PPV:PCBM devices at temperatures below 130K. The initial CT generation rates are not expected to change with temperature since the exciton diffusion yield in bulk heterojunctions is close to unity and hardly dependent on temperature.[141] Indeed, under reverse bias at $V = -1\text{V}$, we observe similar photocurrent densities for above-gap and below-gap excitations; see Figure 8-7b and d. Therefore, the slightly higher V_{OC} for above-gap excitations might mean that a hot CT process reduces the CT recombination loss by dissociating hot CT states into deeper Coulomb potential wells. The effect is weak and only observable at low temperature, perhaps because the relaxation of hot CT states slows down with decreasing phonon densities.

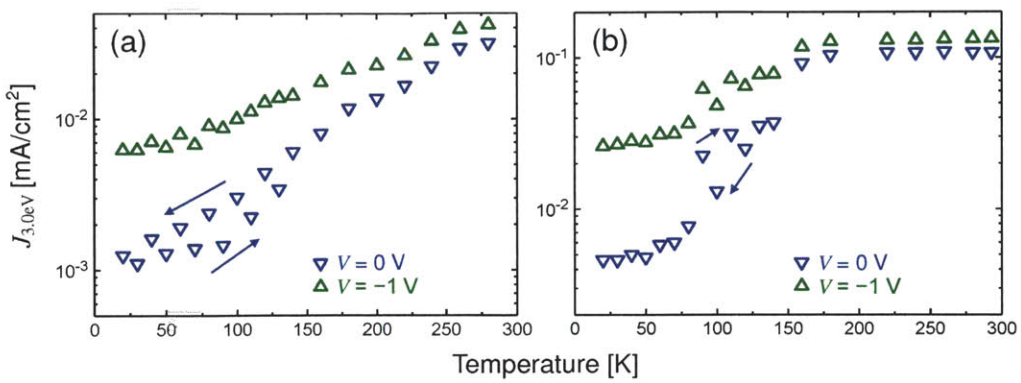

Figure 8-8 **(a)** The photocurrent density of a MDMO-PPV:PCBM device as a function of temperature under the excitation of $h\nu = 3.0$ eV. Voltages of $V = 0$V (▽) and $V = -1$V (△) were applied. The arrow indicates the sequence at which the measurement was taken. The discrepancy of the data measured in upward and downward directions is attributed to the device degradation. **(b)** The equivalent of (a) for a P3HT:PCBM device.

It is also notable in Figure 8-7b and d that the above-gap and below-gap excitations show the same temperature dependence of photocurrent. Under the concept of thermally assisted charge separation ($J \sim \exp(-E_B/kT)$, where E_B is the binding energy),[120] this implies that the binding energy of CT states created from exciton dissociation is equal to that of directly photogenerated bound CT states. We confirm this conclusion again by observing that below-gap and above-gap excitations generate the equivalent photocurrent under varying electric-field; see Figure 8-9.

Figure 8-9 plots the current-voltage (IV) characteristics given above-gap ($h\nu = 3.0$ eV) and below-gap ($h\nu = 1.5$ eV) excitations. The incident light intensity was modulated with optical density filters to match the photocurrent at $V = -2$V and, thus, roughly equalize the initial CT generation rate for both excitations. For the two

heterojunction systems, nearly equal IV curves were produced regardless of whether excitons or CT states are initially excited. The largest difference is observed in the short-circuit current of MDMO-PPV:PCBM devices. But even this accounts for less than 10% of collected charges, implying negligible hot processes. The IV characteristics are the outcome of charge separation under the internal electric field determined by the applied voltage.[120] This result confirms that the CT states created from exciton dissociation have the same electric-field dependence and, presumably, the same binding energy, as the thermally-relaxed CT states generated by sub-gap illumination.

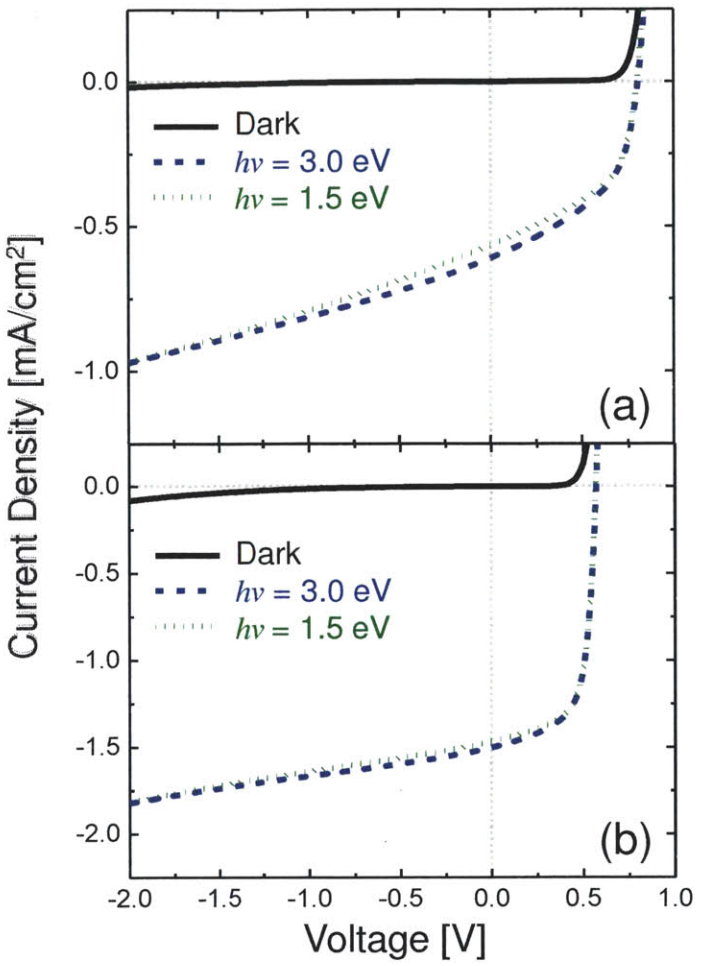

Figure 8-9 **(a)** The dark-current and photocurrent densities of an MDMO-PPV:PCBM photovoltaic cell under above-gap ($h\nu$ = 3.0 eV, dashed line) and below-gap ($h\nu$ = 1.5 eV, dotted line) excitations. The incident light intensity was chosen to equalize the photocurrent densities at $V = -2$ V and was 5.7 mW/cm^2 and 0.65 W/cm^2 for $h\nu$ = 3.0 eV and $h\nu$ = 1.5 eV, respectively. **(b)** The equivalent of (a) for a P3HT:PCBM cell. The incident light intensity was 5.7 mW/cm^2 and 1.7 W/cm^2 for $h\nu$ = 3.0 eV and $h\nu$ = 1.5 eV, respectively.

4.7 Conclusion

To summarize, we observe evidence at low temperatures that may be tentatively attributed to weak hot CT state phenomena. At temperatures close to room temperature, where solar cells usually operate, we find that the CT states formed from exciton splitting are indistinguishable from bound CT states.

Our photocurrent and voltage measurements results provide direct confirmation in solar cells of prior spectroscopic studies on above-gap and below-gap excitations. In optical pump-probe spectroscopy on P3HT or MEH-PPV blended with PCBM, both above-gap and below-gap excitations yielded similar carrier dynamics.[142-144] These studies, however, use below-gap pump wavelengths that excite the high energy part of the CT band. By varying the excitation wavelengths through the CT band we show that it is the thermally-relaxed CT states, not hot CT states, which mediate the conversion between excitons and free charge carriers.

We also extend prior electrical studies on the CT states. Zhou *et al.* reported that a modest quantum yield of photocurrent is produced even when the driving force for exciton dissociation ΔE_{CT} is only ~100 meV.[126] Additionally, it has been shown that the electric-field-induced quenching of CT emission matches the field dependence of photocurrent, meaning that it is the thermally-relaxed, light-emitting CT state that is formed right before charge separation.[121, 126]

Our results imply that excess exciton energies at the donor-acceptor interface are not required for efficient photocurrent generation, at least at room temperature. The absence of hot exciton dissociation processes is expected to be especially significant for

the V_{OC} of low-energy gap organic solar cells because the necessity for a large E_{CT} might otherwise dissipate a substantial fraction of the potential open-circuit voltage.[130, 140]

9. Conclusion and Outlook

Singlet fission photovoltaics are in their infancy. There are still a lot of issues to be solved in both fundamental understanding and device implementation of singlet fission process.

Regarding a theory governing singlet exciton fission, I and my co-workers developed a simple model that can predict the rate of singlet exciton fission through intermolecular coupling. We constructed our model based on data collected from pentacene, an archetype that exhibits exothermic singlet fission. In pentacene, transfer of a singlet to two triplets is almost resonant. Our model can be expanded to test the dynamics of singlet fission in molecules that have a different amount of driving energies—for example, singlet fission in tetracene is slightly endothermic and hexacene may generate two triplets from one singlet in the Marcus inverted regime. A model that can predict the behaviour of singlet fission over molecules with different driving forces would significantly benefit the design of efficient singlet fission molecules and device structures.

Our pentacene multilayer photodetectors, for the first time, demonstrated photocurrent generation from singlet fission. Our photodetector showed the external quantum efficiency approaching 100% under a high reverse bias. Concurrently, the magnetic field effect on photocurrent confirmed the presence of singlet fission in

photocurrent. Moreover, magnetic field probes with varying pentacene thicknesses revealed that one of the major loss mechanisms is direct dissociation of singlet photoexcitations before undergoing singlet fission.

By analysing the loss mechanism of singlet fission devices, we demonstrated pentacene-based photovoltaic cells that generate more than one electron per photon in the visible spectrum. Using an exciton blocking layer and light trapping schemes, our solar cells exhibited a peak external quantum efficiency of 109%. To our knowledge, this is the first time that any solar cell has achieved quantum efficiencies over 100% outside the UV spectrum. The main bottleneck for better efficiencies is short exciton diffusion length of pentacene thin films and its limitation on pentacene absorption. The exciton diffusion toward donor-acceptor junctions can be improved by engineering morphologies of pentacene thin films. Nanophotonic structuring of optical cavities may also improve the absorption from a thin layer of pentacene.

Singlet exciton fission doubles photocurrent, but halves open-circuit voltages. To increase the net efficiency, singlet fission materials need to be combined with long-wavelength absorbing materials that can capture the photons between the singlet and triplet level of the singlet fission molecule. So far this scheme has been implemented in two device architectures: singlet-fission photovoltaic cells with low bandgap donors (e.g. tetracene/CuPC/C_{60}) and infrared absorbing acceptors (e.g. pentacene/semiconductor nanocrystals). At present, the heterojunction of pentacene and lead selenide nanocrystals appears to be the most promising system. But these devices generate the vast majority of their photocurrent from the nanocrystals. Performance from the singlet fission material is relatively weak. This may be due in part to solution processing the nanocrystal film on

top of the pentacene layer. An inverted structure may better preserve the properties of pentacene. New organic/inorganic architectures and devices are one amongst many promising directions for the field.

Finally, splitting one singlet into three triplets could lead to efficient management of ultraviolet photons, although this process has yet to be experimentally observed. Using singlet fission into three triplets, one could imagine building 'ultimate' singlet fission photovoltaic cells that produce three electrons from the ultraviolet, two from the visible, and one in the infrared. As an important step toward this goal, we demonstrated singlet exciton fission in hexacene, the energetics of which may allow for generating three triplets per photon.

References

[1] M. Loster. (2010) Total Primary Energy Supply — From Sunlight.

[2] Smil, p. 12, 2006.

[3] O. Morton, "Solar energy: A new day dawning?: Silicon Valley sunrise," *Nature,* vol. 443, pp. 19, 2006.

[4] (2011) Solar Energy Perspectives: Executive Summary. *International Energy Agency.*

[5] Solarbuzz. (2012) Module Pricing. Available: www.solarbuzz.com

[6] NREL. (2012). *NREL, UCLA Certify World Record for Polymer Solar Cell Efficiency*. Available: http://www.nrel.gov/news/press/2012/1801.html

[7] M. A. Baldo. *MIT 6.729 Molecular Electronics Lecture Note.*

[8] M. Pope and C. E. Swenberg, *Electronic Processes in Organic Crystals* Oxford University, 1982.

[9] P. Peumans, A. Yakimov, and S. R. Forrest, "Small molecular weight organic thin-film photodetectors and solar cells," *Journal of Applied Physics,* vol. 93, pp. 3693, April 1 2003.

[10] G. D. Scholes and G. Rumbles, "Excitons in nanoscale systems," *Nat Mater,* vol. 5, pp. 683, 2006.

[11] D. J. Griffiths, *Introduction to Quantum Mechanics* Prentice Hall, 2004.

[12] M. A. Baldo and S. R. Forrest, "Transient analysis of organic electrophosphorescence: I. Transient analysis of triplet energy transfer," *Physical Review B,* vol. 62, pp. 10958, 2000.

[13] M. B. Smith and J. Michl, "Singlet Fission," *Chemical Reviews,* vol. 110, pp. 6891, 2010/11/10 2010.

[14] W. Shockley and H. J. Queisser, "Detailed Balance Limit of Efficiency of p-n Junction Solar Cells," *Journal of Applied Physics,* vol. 32, pp. 510, 1961.

[15] S. R. Forrest, "The path to ubiquitous and low-cost organic electronic appliances on plastic," *Nature,* vol. 428, pp. 911, 2004.

[16] P. Peumans, V. Bulovic, and S. R. Forrest, "Efficient, high-bandwidth organic multilayer photodetectors," *Applied Physics Letters,* vol. 76, pp. 3855, 2000.

[17] C. Jundt, G. Klein, B. Sipp, J. Lemoigne, M. Joucla, and A. A. Villaeys, "EXCITON DYNAMICS IN PENTACENE THIN-FILMS STUDIED BY PUMP-PROBE SPECTROSCOPY," *Chemical Physics Letters,* vol. 241, pp. 84, Jul 1995.

[18] M. Pope and C. Swenberg, *Electronic Processes in Organic Crystals*, 1st ed. Oxford: Oxford University Press, 1982.

[19] V. K. Thorsmolle, R. D. Averitt, J. Demsar, D. L. Smith, S. Tretiak, R. L. Martin, X. Chi, B. K. Crone, A. P. Ramirez, and A. J. Taylor, "Morphology Effectively Controls Singlet-Triplet Exciton Relaxation and Charge Transport in Organic Semiconductors," *Physical Review Letters,* vol. 102, p. 017401, Jan 2009.

[20] J. G. Xue and S. R. Forrest, "Carrier transport in multilayer organic photodetectors: II. Effects of anode preparation," *Journal of Applied Physics,* vol. 95, pp. 1869, Feb 2004.

[21] S. Yoo, B. Domercq, and B. Kippelen, "Efficient thin-film organic solar cells based on pentacene/C-60 heterojunctions," *Applied Physics Letters,* vol. 85, pp. 5427, Nov 2004.

[22] A. Kahn, N. Koch, and W. Y. Gao, "Electronic structure and electrical properties of interfaces between metals and pi-conjugated molecular films," *Journal of Polymer Science Part B-Polymer Physics,* vol. 41, pp. 2529, Nov 2003.

[23] R. Mitsumoto, T. Araki, E. Ito, Y. Ouchi, K. Seki, K. Kikuchi, Y. Achiba, H. Kurosaki, T. Sonoda, H. Kobayashi, O. V. Boltalina, V. K. Pavlovich, L. N. Sidorov, Y. Hattori, N. Liu, S. Yajima, S. Kawasaki, F. Okino, and H. Touhara, "Electronic Structures and Chemical Bonding of Fluorinated Fullerenes Studied by NEXAFS, UPS, and Vacuum-UV Absorption Spectroscopies," *The Journal of Physical Chemistry A,* vol. 102, pp. 552, 1998.

[24] J. Gao and F. A. Hegmann, "Bulk photoconductive gain in pentacene thin films," *Applied Physics Letters,* vol. 93, p. 223306, 2008.

[25] R. C. Johnson and R. E. Merrifield, "Effects of Magnetic Fields on the Mutual Annihilation of Triplet Excitons in Anthracene Crystals," *Physical Review B,* vol. 1, pp. 896, 1970.

[26] C. E. Swenberg and N. E. Geacintov, "Organic molecular photophysics," in *Organic molecular photophysics*. vol. 10, J. B. Birks, Ed., ed London: J. Wiley, 1975.

[27] Y. Mori, Y. Sakaguchi, and H. Hayashi, "Spin effects on decay dynamics of charge-separated states generated by photoinduced electron transfer in zinc

porphyrin-naphthalenediimide dyads," *Journal of Physical Chemistry A,* vol. 106, pp. 4453, May 2002.

[28] Z. Xu and B. Hu, "Photovoltaic Processes of Singlet and Triplet Excited States in Organic Solar Cells," *Advanced Functional Materials,* vol. 18, pp. 2611, 2008.

[29] C. J. Brabec, G. Zerza, G. Cerullo, S. De Silvestri, S. Luzzati, J. C. Hummelen, and S. Sariciftci, "Tracing photoinduced electron transfer process in conjugated polymer/fullerene bulk heterojunctions in real time," *Chemical Physics Letters,* vol. 340, pp. 232, Jun 2001.

[30] H. Bouchriha, V. Ern, J. L. Fave, C. Guthmann, and M. Schott, "MAGNETIC-FIELD DEPENDENCE OF SINGLET EXCITON FISSION AND FLUORESCENCE IN CRYSTALLINE TETRACENE AT 300-K," *J. Phys. (Paris),* vol. 39, pp. 257, 1978.

[31] A. Rao, M. W. B. Wilson, J. M. Hodgkiss, S. Albert-Seifried, H. Bässler, and R. H. Friend, "Exciton Fission and Charge Generation via Triplet Excitons in Pentacene/C60 Bilayers," *Journal of the American Chemical Society,* vol. 132, pp. 12698, 2010/09/15 2010.

[32] W.-L. Chan, M. Ligges, A. Jailaubekov, L. Kaake, L. Miaja-Avila, and X.-Y. Zhu, "Observing the Multiexciton State in Singlet Fission and Ensuing Ultrafast Multielectron Transfer," *Science,* vol. 334, pp. 1541, December 16, 2011 2011.

[33] P. J. Jadhav, P. R. Brown, N. Thompson, B. Wunsch, A. Mohanty, S. R. Yost, E. Hontz, T. Van Voorhis, M. G. Bawendi, V. Bulović, and M. A. Baldo, "Triplet Exciton Dissociation in Singlet Exciton Fission Photovoltaics," *Advanced Materials,* vol. 24, p. 6169, 2012.

[34] B. Ehrler, B. J. Walker, M. L. Böhm, M. W. B. Wilson, Y. Vaynzof, R. H. Friend, and N. C. Greenham, "In situ measurement of exciton energy in hybrid singlet-fission solar cells," *Nat Commun,* vol. 3, p. 1019, 2012.

[35] Q. Wu, B. Kaduk, and T. V. Voorhis, "Constrained density functional theory based configuration interaction improves the prediction of reaction barrier heights," *The Journal of Chemical Physics,* vol. 130, p. 034109, 2009.

[36] S. Yoo, W. J. Potscavage Jr, B. Domercq, S.-H. Han, T.-D. Li, S. C. Jones, R. Szoszkiewicz, D. Levi, E. Riedo, S. R. Marder, and B. Kippelen, "Analysis of improved photovoltaic properties of pentacene/C60 organic solar cells: Effects of exciton blocking layer thickness and thermal annealing," *Solid-State Electronics,* vol. 51, pp. 1367, 2007.

[37] M. W. B. Wilson, A. Rao, J. Clark, R. S. S. Kumar, D. Brida, G. Cerullo, and R. H. Friend, "Ultrafast Dynamics of Exciton Fission in Polycrystalline Pentacene," *Journal of the American Chemical Society,* vol. 133, pp. 11830, 2011/08/10 2011.

[38] C. Jundt, G. Klein, B. Sipp, J. Le Moigne, M. Joucla, and A. A. Villaeys, "Exciton dynamics in pentacene thin films studied by pump-probe spectroscopy," *Chemical Physics Letters,* vol. 241, pp. 84, 1995.

[39] O. E. Semonin, J. M. Luther, S. Choi, H. Y. Chen, J. Gao, A. J. Nozik, and M. C. Beard, "Peak external photocurrent quantum efficiency exceeding 100% via MEG in a quantum dot solar cell," *Science,* vol. 334, pp. 1530, 2011.

[40] M. B. Smith and J. Michl, "Singlet fission," *Chemical Reviews,* vol. 110, p. 6891, 2010.

[41] J. Lee, P. Jadhav, and M. A. Baldo, "High efficiency organic multilayer photodetectors based on singlet exciton fission," *Applied Physics Letters,* vol. 95, pp. 033301, 2009.

[42] M. W. Wilson, A. Rao, J. Clark, R. S. Kumar, D. Brida, G. Cerullo, and R. H. Friend, "Ultrafast dynamics of exciton fission in polycrystalline pentacene," *J Am Chem Soc,* vol. 133, pp. 11830, 2011.

[43] J. C. Johnson, T. H. Reilly, A. C. Kanarr, and J. van de Lagemaat, "The Ultrafast Photophysics of Pentacene Coupled to Surface Plasmon Active Nanohole Films," *The Journal of Physical Chemistry C,* vol. 113, pp. 6871, 2009.

[44] H. Marciniak, M. Fiebig, M. Huth, S. Schiefer, B. Nickel, F. Selmaier, and S. Lochbrunner, "Ultrafast Exciton Relaxation in Microcrystalline Pentacene Films," *Physical Review Letters,* vol. 99, 2007.

[45] V. Thorsmølle, R. Averitt, J. Demsar, D. Smith, S. Tretiak, R. Martin, X. Chi, B. Crone, A. Ramirez, and A. Taylor, "Morphology Effectively Controls Singlet-Triplet Exciton Relaxation and Charge Transport in Organic Semiconductors," *Physical Review Letters,* vol. 102, 2009.

[46] W. L. Chan, M. Ligges, A. Jailaubekov, L. Kaake, L. Miaja-Avila, and X. Y. Zhu, "Observing the multiexciton state in singlet fission and ensuing ultrafast multielectron transfer," *Science,* vol. 334, pp. 1541, 2011.

[47] P. J. Jadhav, A. Mohanty, J. Sussman, J. Lee, and M. A. Baldo, "Singlet exciton fission in nanostructured organic solar cells," *Nano Lett,* vol. 11, pp. 1495, 2011.

[48] B. Ehrler, B. J. Walker, M. L. Bohm, M. W. Wilson, Y. Vaynzof, R. H. Friend, and N. C. Greenham, "In situ measurement of exciton energy in hybrid singlet-fission solar cells," *Nat Commun,* vol. 3, p. 1019, 2012.

[49] B. Ehrler, M. W. Wilson, A. Rao, R. H. Friend, and N. C. Greenham, "Singlet exciton fission-sensitized infrared quantum dot solar cells," *Nano Lett,* vol. 12, pp. 1053, 2012.

[50] D. L. Dexter, "Two ideas on energy transfer phenomena: Ion-pair effects involving the OH stretching mode, and sensitization of photovoltaic cells," *Journal of Luminescence,* vol. 18–19, Part 2, pp. 779, 1979.

[51] A. Suna, "Kinematics of Exciton-Exciton Annihilation in Molecular Crystals," *Physical Review B,* vol. 1, p. 24, 1969.

[52] V. K. Thorsmølle, R. D. Averitt, J. Demsar, D. L. Smith, S. Tretiak, R. L. Martin, X. Chi, B. K. Crone, A. P. Ramirez, and A. J. Taylor, "Morphology Effectively Controls Singlet-Triplet Exciton Relaxation and Charge Transport in Organic Semiconductors," *Physical Review Letters,* vol. 102, p. 017401, 2009.

[53] J. Burgos, M. Pope, C. E. Swenberg, and R. R. Alfano, "Heterofission in pentacene-doped tetracene single crystals," *physica status solidi (b),* vol. 83, pp. 249, 1977.

[54] S. Yoo, B. Domercq, and B. Kippelen, "Efficient thin-film organic solar cells based on pentacene/C[sub 60] heterojunctions," *Applied Physics Letters,* vol. 85, pp. 5427, 2004.

[55] A. K. Pandey, S. Dabos-Seignon, and J.-M. Nunzi, "Pentacene: PTCDI-C[sub 13]H[sub 27] molecular blends efficiently harvest light for solar cell applications," *Applied Physics Letters,* vol. 89, pp. 113506, 2006.

[56] F. Monestier, A. K. Pandey, J.-J. Simon, P. Torchio, L. Escoubas, and J.-M. Nunzi, "Optical modeling of the ultimate efficiency of pentacene: N, N[sup [prime]]-ditridecylperylene-3, 4, 9, 10-tetracarboxylic diimide--blend solar cells," *Journal of Applied Physics,* vol. 102, pp. 034512, 2007.

[57] T. Kowalczyk, S. R. Yost, and T. Van Voorhis, "Assessment of the Delta SCF density functional theory approach for electronic excitations in organic dyes," *The Journal of Chemical Physics,* vol. 134, pp. 054128, 2011.

[58] Q. Wu, B. Kaduk, and T. Van Voorhis, "Constrained density functional theory based configuration interaction improves the prediction of reaction barrier heights," *The Journal of Chemical Physics,* vol. 130, pp. 034109, 2009.

[59] R. Nitsche and T. Fritz, "Determination of model-free Kramers-Kronig consistent optical constants of thin absorbing films from just one spectral measurement: Application to organic semiconductors," *Physical Review B,* vol. 70, p. 195432, 2004.

[60] R. P. Groff, P. Avakian, and R. E. Merrifield, "Coexistence of Exciton Fission and Fusion in Tetracene Crystals," *Physical Review B,* vol. 1, pp. 815, 1970.

[61] J. Guo, H. Ohkita, H. Benten, and S. Ito, "Near-IR femtosecond transient absorption spectroscopy of ultrafast polaron and triplet exciton formation in polythiophene films with different regioregularities," *J Am Chem Soc,* vol. 131, pp. 16869, 2009.

[62] C. Swenberg and M. Pope, *Electronic Processes in Organic Crystals*. Oxford, NY: Clarendon Press, 1982.

[63] Z.-L. Guan, J. B. Kim, H. Wang, C. Jaye, D. A. Fischer, Y.-L. Loo, and A. Kahn, "Direct determination of the electronic structure of the poly(3-hexylthiophene):phenyl-[6,6]-C61 butyric acid methyl ester blend," *Organic Electronics,* vol. 11, pp. 1779, 2010.

[64] N. S. Sato, Y; Shinohara, H;, "Threshold ionization energy of C60 in the solid state," *Chemical Physics,* vol. 162, p. 6, 1992.

[65] A. Kahn, N. Koch, and W. Gao, "Electronic Structure and Electrical Properties of Interfaces between Metals and pi-Conjugated Molecular Films," *Journal of Polymer Science: Part B,* vol. 41, p. 20, 2003.

[66] J. Hwang, A. Wan, and A. Kahn, "Energetics of metal–organic interfaces: New experiments and assessment of the field," *Materials Science and Engineering: R: Reports,* vol. 64, pp. 1, 2009.

[67] B. Xu and S. Holdcroft, "Triplet emission from π-conjugated polymers," *Advanced Materials,* vol. 6, pp. 325, 1994.

[68] P. D. Reusswig, D. N. Congreve, N. J. Thompson, and M. A. Baldo, "Enhanced external quantum efficiency in an organic photovoltaic cell via singlet fission exciton sensitizer," *Applied Physics Letters,* vol. 101, pp. 113304, 2012.

[69] R. E. Merrifield, P. Avakian, and R. P. Groff, "Fission of singlet excitons into pairs of triplet excitons in tetracene crystals," *Chemical Physics Letters,* vol. 3, pp. 386, 1969.

[70] F. Monestier, A. K. Pandey, J. J. Simon, P. Torchio, L. Escoubas, and J. M. Nunzi, "Optical modeling of the ultimate efficiency of pentacene: N, N'-ditridecylperyiene-3, 4, 9, 10-tetracarboxylic diimide-blend solar cells," *Journal of Applied Physics,* vol. 102, Aug 2007.

[71] P. D. Reusswig, D. N. Congreve, N. J. Thompson, and M. A. Baldo, "Enhanced external quantum efficiency in an organic photovoltaic cell via singlet fission exciton sensitizer," *Applied Physics Letters,* vol. 101, p. 113304, 2012.

[72] S. B. Rim, S. Zhao, S. R. Scully, M. D. McGehee, and P. Peumans, "An effective light trapping configuration for thin-film solar cells," *Applied Physics Letters,* vol. 91, Dec 2007.

[73] K. Tvingstedt, V. Andersson, F. Zhang, and O. Inganäs, "Folded reflective tandem polymer solar cell doubles efficiency," *Applied Physics Letters,* vol. 91, p. 123514, 2007.

[74] H. Bouchriha, V. Ern, J. L. Fave, C. Guthmann, and M. Schott, "Magnetic field dependence of singlet exciton fission and fluorescence in crystalline tetracene at 300 K," *J. Phys. France,* vol. 39, pp. 257, 1978.

[75] M. A. Green, "The path to 25% silicon solar cell efficiency: History of silicon cell evolution," *Progress in Photovoltaics: Research and Applications,* vol. 17, pp. 183, 2009.

[76] J. Lee, M. J. Bruzek, N. J. Thompson, M. Y. Sfeir, J. E. Anthony, and M. A. Baldo, "Singlet Exciton Fission in a Hexacene Derivative," *Advanced Materials,* pp. n/a, 2013.

[77] J. C. Johnson, A. J. Nozik, and J. Michl, "High Triplet Yield from Singlet Fission in a Thin Film of 1,3-Diphenylisobenzofuran," *Journal of the American Chemical Society,* vol. 132, pp. 16302, 2010/11/24 2010.

[78] C. C. Gradinaru, J. Kennis, E. Papagiannakis, I. H. M. van Stokkum, R. J. Cogdell, G. R. Fleming, R. A. Niederman, and R. van Grondelle, "An unusual pathway of excitation energy deactivation in carotenoids: singlet-to-triplet conversion on an ultrafast timescale in a photosynthetic antenna," *Proceedings of the National Academy of Sciences,* vol. 98, pp. 2364, 2001.

[79] E. C. Greyson, J. Vura-Weis, J. Michl, and M. A. Ratner, "Maximizing Singlet Fission in Organic Dimers: Theoretical Investigation of Triplet Yield in the Regime of Localized Excitation and Fast Coherent Electron Transfer†," *The Journal of Physical Chemistry B,* vol. 114, pp. 14168, 2010/11/18 2010.

[80] T. C. Berkelbach, M. S. Hybertsen, and D. R. Reichman, "Microscopic theory of singlet exciton fission. I. General formulation," *arXiv preprint arXiv:1211.6458,* 2012.

[81] T. C. Berkelbach, M. S. Hybertsen, and D. R. Reichman, "Microscopic theory of singlet exciton fission. II. Application to pentacene dimers and the role of superexchange," *arXiv preprint arXiv:1211.6459,* 2012.

[82] J. Jortner and M. Bixon, "Intramolecular vibrational excitations accompanying solvent-controlled electron transfer reactions," *The Journal of Chemical Physics,* vol. 88, pp. 167, 1988.

[83] W.-L. Chan, M. Ligges, and X. Y. Zhu, "The energy barrier in singlet fission can be overcome through coherent coupling and entropic gain," *Nat Chem,* vol. advance online publication, 2012.

[84] Q. Miao, X. Chi, S. Xiao, R. Zeis, M. Lefenfeld, T. Siegrist, M. L. Steigerwald, and C. Nuckolls, "Organization of acenes with a cruciform assembly motif," *Journal of the American Chemical Society,* vol. 128, pp. 1340, 2006.

[85] T. Siegrist, C. Besnard, S. Haas, M. Schiltz, P. Pattison, D. Chernyshov, B. Batlogg, and C. Kloc, "A Polymorph Lost and Found: The High-Temperature Crystal Structure of Pentacene," *Advanced Materials,* vol. 19, pp. 2079, 2007.

[86] J. E. Anthony, J. S. Brooks, D. L. Eaton, and S. R. Parkin, "Functionalized pentacene: Improved electronic properties from control of solid-state order," *Journal of the American Chemical Society,* vol. 123, pp. 9482, 2001.

[87] Q. Wu and T. Van Voorhis, "Direct optimization method to study constrained systems within density-functional theory," *Physical Review A,* vol. 72, p. 024502, 2005.

[88] Q. Wu and T. Van Voorhis, "Direct calculation of electron transfer parameters through constrained density functional theory," *The Journal of Physical Chemistry A,* vol. 110, pp. 9212, 2006.

[89] J. Aaqvist and A. Warshel, "Simulation of enzyme reactions using valence bond force fields and other hybrid quantum/classical approaches," *Chemical Reviews,* vol. 93, pp. 2523, 1993/11/01 1993.

[90] Q. Wu, C. L. Cheng, and T. Van Voorhis, "Configuration interaction based on constrained density functional theory: A multireference method," *The Journal of Chemical Physics,* vol. 127, p. 164119, 2007.

[91] S. R. Yost, E. Hontz, S. Yeganeh, and T. Van Voorhis, "Triplet Versus Singlet Energy Transfer in Organic Semiconductors: The Tortoise and the Hare," *The Journal of Physical Chemistry C,* 2012.

[92] P. M. Zimmerman, F. Bell, D. Casanova, and M. Head-Gordon, "Mechanism for singlet fission in pentacene and tetracene: from single exciton to two triplets," *Journal of the American Chemical Society,* vol. 133, pp. 19944, 2011.

[93] H. Yamagata, J. Norton, E. Hontz, Y. Olivier, D. Beljonne, J. Bredas, R. Silbey, and F. Spano, "The nature of singlet excitons in oligoacene molecular crystals," *The Journal of Chemical Physics,* vol. 134, pp. 204703, 2011.

[94] E. Akesson, G. C. Walker, and P. F. Barbara, "Dynamic solvent effects on electron transfer rates in the inverted regime: Ultrafast studies on the betaines," DTIC Document1991.

[95] M. Sparpaglione and S. Mukamel, "Adiabatic vs. nonadiabatic electron transfer and longitudinal solvent dielectric relaxation: beyond the Debye model," *Journal of Physical Chemistry,* vol. 91, pp. 3938, 1987.

[96] H. Sumi and R. Marcus, "Dynamical effects in electron transfer reactions," *The Journal of Chemical Physics,* vol. 84, p. 4894, 1986.

[97] R. Marcus, "On the Theory of Oxidation-Reduction Reactions Involving Electron Transfer. I," *The Journal of Chemical Physics,* vol. 24, pp. 966, 1956.

[98] C. Ramanan, A. L. Smeigh, J. E. Anthony, T. J. Marks, and M. R. Wasielewski, "Competition between Singlet Fission and Charge Separation in Solution-Processed Blend Films of 6,13-Bis(triisopropylsilylethynyl)pentacene with Sterically-Encumbered Perylene-3,4:9,10-bis(dicarboximide)s," *Journal of the American Chemical Society,* vol. 134, pp. 386, 2012/01/11 2011.

[99] M. Pabst and A. Kohn, "Implementation of transition moments between excited states in the approximate coupled-cluster singles and doubles model," *The Journal of Chemical Physics,* vol. 129, pp. 214101, 2008.

[100] A. Rao, M. W. B. Wilson, S. Albert-Seifried, R. Di Pietro, and R. H. Friend, "Photophysics of pentacene thin films: The role of exciton fission and heating effects," *Physical Review B,* vol. 84, p. 195411, 2011.

[101] C. Hellner, L. Lindqvist, and P. C. Roberge, "Absorption spectrum and decay kinetics of triplet pentacene in solution, studied by flash photolysis," *Journal of the Chemical Society, Faraday Transactions 2: Molecular and Chemical Physics,* vol. 68, pp. 1928, 1972.

[102] P. J. Jadhav, A. Mohanty, J. Sussman, J. Lee, and M. A. Baldo, "Singlet Exciton Fission in Nanostructured Organic Solar Cells," *Nano Letters,* vol. 11, pp. 1495, 2011/04/13 2011.

[103] B. Ehrler, M. W. B. Wilson, A. Rao, R. H. Friend, and N. C. Greenham, "Singlet Exciton Fission-Sensitized Infrared Quantum Dot Solar Cells," *Nano Letters,* vol. 12, pp. 1053, 2012/02/08 2012.

[104] K. N. Houk, P. S. Lee, and M. Nendel, "Polyacene and Cyclacene Geometries and Electronic Structures: Bond Equalization, Vanishing Band Gaps, and Triplet

Ground States Contrast with Polyacetylene," *The Journal of Organic Chemistry,* vol. 66, pp. 5517, 2001/08/01 2001.

[105] H. Angliker, E. Rommel, and J. Wirz, "Electronic spectra of hexacene in solution (ground state. Triplet state. Dication and dianion)," *Chemical Physics Letters,* vol. 87, pp. 208, 1982.

[106] R. Mondal, R. M. Adhikari, B. K. Shah, and D. C. Neckers, "Revisiting the Stability of Hexacenes," *Organic Letters,* vol. 9, pp. 2505, 2007/06/01 2007.

[107] M. M. Payne, S. R. Parkin, and J. E. Anthony, "Functionalized Higher Acenes: Hexacene and Heptacene," *Journal of the American Chemical Society,* vol. 127, pp. 8028, 2005/06/01 2005.

[108] B. Purushothaman, S. R. Parkin, and J. E. Anthony, "Synthesis and Stability of Soluble Hexacenes," *Organic Letters,* vol. 12, pp. 2060, 2010/05/07 2010.

[109] M. Watanabe, Y. J. Chang, S.-W. Liu, T.-H. Chao, K. Goto, M. IslamMd, C.-H. Yuan, Y.-T. Tao, T. Shinmyozu, and T. J. Chow, "The synthesis, crystal structure and charge-transport properties of hexacene," *Nat Chem,* vol. 4, pp. 574, 2012.

[110] B. Purushothaman, S. R. Parkin, M. J. Kendrick, D. David, J. W. Ward, L. Yu, N. Stingelin, O. D. Jurchescu, O. Ostroverkhova, and J. E. Anthony, "Synthesis and charge transport studies of stable, soluble hexacenes," *Chemical Communications,* vol. 48, pp. 8261, 2012.

[111] A. Kahn, N. Koch, and W. Gao, "Electronic structure and electrical properties of interfaces between metals and π-conjugated molecular films," *Journal of Polymer Science Part B: Polymer Physics,* vol. 41, pp. 2529, 2003.

[112] S. A. Kovalenko, A. L. Dobryakov, J. Ruthmann, and N. P. Ernsting, "Femtosecond spectroscopy of condensed phases with chirped supercontinuum probing," *Physical Review A,* vol. 59, pp. 2369, 1999.

[113] E. M. Grumstrup, J. C. Johnson, and N. H. Damrauer, "Enhanced Triplet Formation in Polycrystalline Tetracene Films by Femtosecond Optical-Pulse Shaping," *Physical Review Letters,* vol. 105, p. 257403, 2010.

[114] L. Ma, K. Zhang, C. Kloc, H. Sun, M. E. Michel-Beyerle, and G. G. Gurzadyan, "Singlet fission in rubrene single crystal: direct observation by femtosecond pump-probe spectroscopy," *Physical Chemistry Chemical Physics,* vol. 14, pp. 8307, 2012.

[115] N. Nijegorodov, V. Ramachandran, and D. P. Winkoun, "The dependence of the absorption and fluorescence parameters, the intersystem crossing and internal conversion rate constants on the number of rings in polyacene molecules," *Spectrochimica Acta Part A: Molecular and Biomolecular Spectroscopy,* vol. 53, pp. 1813, 1997.

[116] A. D. Platt, J. Day, S. Subramanian, J. E. Anthony, and O. Ostroverkhova, "Optical, fluorescent, and (photo) conductive properties of high-performance functionalized pentacene and anthradithiophene derivatives," *The journal of physical chemistry. C, Nanomaterials and interfaces,* vol. 113, p. 14006, 2009.

[117] H. Imahori, K. Tamaki, D. M. Guldi, C. Luo, M. Fujitsuka, O. Ito, Y. Sakata, and S. Fukuzumi, "Modulating Charge Separation and Charge Recombination Dynamics in Porphyrin–Fullerene Linked Dyads and Triads: Marcus-Normal

versus Inverted Region," *Journal of the American Chemical Society,* vol. 123, pp. 2607, 2001/03/01 2001.

[118] B. K. Li, H. T. He, W. J. Chen, M. K. Lam, L. X. Zhang, K. W. Cheah, and J. N. Wang, "Magnetic Field Effect on Photocurrent in Single Layer Organic Semiconductor Devices," *AIP Conference Proceedings,* vol. 1399, pp. 881, 2011.

[119] X. Y. Zhu, Q. Yang, and M. Muntwiler, "Charge-Transfer Excitons at Organic Semiconductor Surfaces and Interfaces," *Accounts of Chemical Research,* vol. 42, pp. 1779, 2009.

[120] P. W. M. Blom, V. D. Mihailetchi, L. J. A. Koster, and D. E. Markov, "Device Physics of Polymer:Fullerene Bulk Heterojunction Solar Cells," *Advanced Materials,* vol. 19, pp. 1551, 2007.

[121] D. Veldman, O. z. İpek, S. C. J. Meskers, J. r. Sweelssen, M. M. Koetse, S. C. Veenstra, J. M. Kroon, S. S. v. Bavel, J. Loos, and R. A. J. Janssen, "Compositional and Electric Field Dependence of the Dissociation of Charge Transfer Excitons in Alternating Polyfluorene Copolymer/Fullerene Blends," *Journal of the American Chemical Society,* vol. 130, pp. 7721, 2008.

[122] M. Muntwiler, Q. Yang, W. A. Tisdale, and X. Y. Zhu, "Coulomb Barrier for Charge Separation at an Organic Semiconductor Interface," *Physical Review Letters,* vol. 101, p. 196403, Nov 7 2008.

[123] H. Ohkita, S. Cook, Y. Astuti, W. Duffy, S. Tierney, W. Zhang, M. Heeney, I. McCulloch, J. Nelson, D. D. C. Bradley, and J. R. Durrant, "Charge Carrier Formation in Polythiophene/Fullerene Blend Films Studied by Transient

Absorption Spectroscopy," *Journal of the American Chemical Society,* vol. 130, pp. 3030, 2008.

[124] T. M. Clarke, A. M. Ballantyne, J. Nelson, D. D. C. Bradley, and J. R. Durrant, "Free Energy Control of Charge Photogeneration in Polythiophene/Fullerene Solar Cells: The Influence of Thermal Annealing on P3HT/PCBM Blends," *Advanced Functional Materials,* vol. 18, pp. 4029, 2008.

[125] R. D. Pensack and J. B. Asbury, "Barrierless Free Carrier Formation in an Organic Photovoltaic Material Measured with Ultrafast Vibrational Spectroscopy," *Journal of the American Chemical Society,* vol. 131, pp. 15986, 2009.

[126] Y. Zhou, K. Tvingstedt, F. Zhang, C. Du, W.-X. Ni, M. R. Andersson, and O. Inganäs, "Observation of a Charge Transfer State in Low-Bandgap Polymer/Fullerene Blend Systems by Photoluminescence and Electroluminescence Studies," *Advanced Functional Materials,* vol. 19, pp. 3293, 2009.

[127] S. H. Park, A. Roy, S. Beaupre, S. Cho, N. Coates, J. S. Moon, D. Moses, M. Leclerc, K. Lee, and A. J. Heeger, "Bulk heterojunction solar cells with internal quantum efficiency approaching 100%," *Nature Photonics,* vol. 3, pp. 297, May 2009.

[128] J. J. Benson-Smith, L. Goris, K. Vandewal, K. Haenen, J. V. Manca, D. Vanderzande, D. D. C. Bradley, and J. Nelson, "Formation of a Ground-State Charge-Transfer Complex in Polyfluorene//[6,6]-Phenyl-C61 Butyric Acid Methyl Ester (PCBM) Blend Films and Its Role in the Function of

Polymer/PCBM Solar Cells," *Advanced Functional Materials,* vol. 17, pp. 451, 2007.

[129] K. Vandewal, A. Gadisa, W. D. Oosterbaan, S. Bertho, F. Banishoeib, I. Van Severen, L. Lutsen, T. J. Cleij, D. Vanderzande, and J. V. Manca, "The relation between open-circuit voltage and the onset of photocurrent generation by charge-transfer absorption in polymer: Fullerene bulk heterojunction solar cells," *Advanced Functional Materials,* vol. 18, pp. 2064, Jul 2008.

[130] K. Vandewal, K. Tvingstedt, A. Gadisa, O. Inganas, and J. V. Manca, "On the origin of the open-circuit voltage of polymer-fullerene solar cells," *Nature Materials,* vol. 8, pp. 904, 2009.

[131] K. Tvingstedt, K. Vandewal, A. Gadisa, F. L. Zhang, J. Manca, and O. Inganas, "Electroluminescence from Charge Transfer States in Polymer Solar Cells," *Journal of the American Chemical Society,* vol. 131, pp. 11819, Aug 2009.

[132] L. Goris, K. Haenen, M. Nesladek, P. Wagner, D. Vanderzande, L. De Schepper, J. D'Haen, L. Lutsen, and J. V. Manca, "Absorption phenomena in organic thin films for solar cell applications investigated by photothermal deflection spectroscopy," *Journal of Materials Science,* vol. 40, pp. 1413, Mar 2005.

[133] L. Goris, A. Poruba, L. Hod'akova, M. Vanecek, K. Haenen, M. Nesladek, P. Wagner, D. Vanderzande, L. De Schepper, and J. V. Manca, "Observation of the subgap optical absorption in polymer-fullerene blend solar cells," *Applied Physics Letters,* vol. 88, p. 052113, Jan 2006.

[134] T. Drori, C. X. Sheng, A. Ndobe, S. Singh, J. Holt, and Z. V. Vardeny, "Below-gap excitation of pi-conjugated polymer-fullerene blends: Implications for bulk

organic heterojunction solar cells," *Physical Review Letters,* vol. 101, p. 037401, Jul 2008.

[135] A. J. Cohen, P. Mori-Sanchez, and W. Yang, "Insights into Current Limitations of Density Functional Theory," *Science,* vol. 321, pp. 792, August 8, 2008 2008.

[136] Q. Wu and T. Van Voorhis, "Direct calculation of electron transfer parameters through constrained density functional theory," *Journal of Physical Chemistry A,* vol. 110, pp. 9212, Jul 27 2006.

[137] H. Hoppe, N. S. Sariciftci, and D. Meissner, "Optical constants of conjugated polymer/fullerene based bulk-heterojunction organic solar cells," *Molecular Crystals and Liquid Crystals,* vol. 385, pp. 233, 2002.

[138] A. M. C. Ng, K. Y. Cheung, M. K. Fung, A. B. Djurisic, and W. K. Chan, "Spectroscopic ellipsometry characterization of polymer-fullerene blend films," *Thin Solid Films,* vol. 517, pp. 1047, Dec 1 2008.

[139] K. Vandewal, K. Tvingstedt, A. Gadisa, O. Inganäs, and J. V. Manca, "Relating the open-circuit voltage to interface molecular properties of donor:acceptor bulk heterojunction solar cells," *Physical Review B,* vol. 81, p. 125204, 2010.

[140] B. P. Rand, D. P. Burk, and S. R. Forrest, "Offset energies at organic semiconductor heterojunctions and their influence on the open-circuit voltage of thin-film solar cells," *Physical Review B,* vol. 75, p. 115327, Mar 2007.

[141] O. V. Mikhnenko, F. Cordella, A. B. Sieval, J. C. Hummelen, P. W. M. Blom, and M. A. Loi, "Temperature Dependence of Exciton Diffusion in Conjugated Polymers," *The Journal of Physical Chemistry B,* vol. 112, pp. 11601, 2008.

[142] P. D. Cunningham and L. M. Hayden, "Carrier dynamics resulting from above and below gap excitation of P3HT and P3HT/PCBM investigated by optical-pump terahertz-probe spectroscopy," *Journal of Physical Chemistry C,* vol. 112, pp. 7928, May 29 2008.

[143] P. Parkinson, J. Lloyd-Hughes, M. B. Johnston, and L. M. Herz, "Efficient generation of charges via below-gap photoexcitation of polymer-fullerene blend films investigated by terahertz spectroscopy," *Physical Review B,* vol. 78, p. 115321, Sep 2008.

[144] A. A. Bakulin, D. Martyanov, D. Y. Paraschuk, P. H. M. v. Loosdrecht, and M. S. Pshenichnikov, "Charge-transfer complexes of conjugated polymers as intermediates in charge photogeneration for organic photovoltaics," *Chemical Physics Letters,* vol. 482, pp. 99, 2009.